J. Indian Inst. Sci., Nov.–Dec 1992, 73, 501–578

IISc THESES ABSTRACTS

Thesis Abstract (M.Sc. (Engng))

An implementation of cross architecture procedure call by Laeeq M. Khan.
Research supervisor: Y. N. Srikant.
Department: Computer Science and Automation.

1. Introduction

The biggest motivation for computer networking is resource sharing[1]. It is frequently desirable to pool computers to allow efficient resource sharing (these resources may be real devices such as card readers and printers or they may be virtual devices such as disk files) such that each computer retains autonomy over its environment. Further, a crash in a centralized system entails total nonavailability of computing power whereas if a few computers in a network are unoperational, the rest will continue to work unaffected.

Workstations are ideally suited for computing jobs which require an interactive environment because they are basically single-user machines and hence provide consistent response time. Another factor is the availability of many peripheral devices such as mice and light pens which render workstations more user-friendly for interactive jobs. However, workstations are not suitable for highly compute-intensive jobs as they are basically uniprocessor machines operating at moderate frequencies. For such type of work, large mainframes or supercomputers are more suitable, but interactive use of these machines is not economically feasible. Furthermore, devices like mice, etc., are not usually available for these types of machines.

A typical application program is partly interactive and partly compute-intensive and hence requires the features of both workstations and supercomputers.

A usual method to speed up an application is to ship the entire application to a supercomputer using a network connecting the workstation and the supercomputer. In this method, however, the workstation is used only as a terminal to submit a job to the supercomputer and its interactive features remain unutilized.

Another method is the use of remote procedure call (RPC)[2]. Here some of the procedures of an application are implemented as different processes on a remote machine. One problem with this method is parameter passing. Passing parameters by value is not difficult, but passing them by reference is much harder. This problem basically arises due to the fact that the main program and the remote procedure execute in separate address spaces, and this fact gives rise to further difficulties, namely, nonavailability of global variables to remote procedures and impossibility of using pointer variables to access remote structures, etc.

2. The experiment

To circumvent these difficulties we have implemented a cross architecture procedure call (CAPC) model. The purpose of this architecture is to make supercomputers available to workstation users as compute servers.

In this method, a workstation user marks some of the procedures in his/her application program which he/she wants to execute on a remote mainframe or supercomputer connected to the workstation by a network. These procedures are compiled by a compiler to produce machine code for the computer on which they are supposed to be executed. A special-purpose loader loads these procedures on the

appropriate machines and then these procedures are executed on the remote machines at appropriate times without any further modification in the source code

Usually a user will want to execute compute-intensive procedures on supercomputers and interactive parts on a workstation, thus utilizing both the machines most efficiently. In our method, both local and remote procedures use standard subroutine call instructions unlike RPC. In this architecture, both local and remote subroutines share a common virtual address space (physically distributed over many machines) and thus global and pointer variables can be used and parameters can be passed by reference with complete transparency. Arbitrary nesting of remote and local procedures is also possible.

In our prototype implementation we have used an IBM-PC (8088 processor operating at 4·7 MHz) as a workstation and a MAGNUM-1 (68030 processor operating at 25 MHz) as a compute server. As an IBM-PC does not have any virtual memory hardware (essential for our architecture) we have simulated a virtual memory management system for that machine through software. Our 'network' is an RS 232C connection between the two machines using COPTL (connection-oriented transport provider for local communications) operating at 9600 baud.

To test the system we have also implemented the required compiler for a simple language (a subset of Pascal-PL/0) which produces code for 8088 and 68030 machines, and also a special loader. The system has been completely implemented and tested with several programs. We have also made a thorough performance study of this system. The system is found to accelerate the applications as much as 2·8 times in the best cases.

References

1. TANENBAUM, A. S. *Computer networks*, 1987, Prentice-Hall India

2. LAMPSON, B. W., PAUL, M. AND SIEGERT, H. J. Distributed systems—architecture and implementation, *Lecture Notes in Computer Sciences*, Vol 105, 1981, Springer-Verlag

Thesis Abstract (M.Sc. (Engng))

DPLLs for network synchronization: a new approach by Satish M. Kulkarni.
Research supervisors: B. S. Sonde and M. V. Pitke
Department: Electrical Communication Engineering.

1. Introduction

The advances in digital ICs and LSI/VLSI technologies have spurred the design, development and application of digital techniques in modern telecommunication networks. The advances in digital switching, in conjunction with those in digital transmission, are now leading to the development of all-digital networks that provide for voice, data and other telematic services going eventually to integrated services digital network. Clock synchronization of all the nodes is an important requirement in the implementation of these networks, in order to avoid the loss of data or slips, due to differences in master-clock frequencies at various nodes in the network. The master–slave synchronization approach is the most commonly used one in these networks for synchronizing the various clocks, which is also the basis for the system being adopted in India. In this approach, all the nodes in the network are synchronized by means of timing information extracted from the incoming digital transmission links A PLL of the second-order type is usually required to derive/lock on to the timing information extracted from the incoming data signal. Fast acquisition and the avoidance of cycle slips during acquisition are important requirements of the PLL for use in this application. With the emergence of LSI/VLSI technologies, Digital PLLs (DPLLs) are now available which offer several advantages over analog PLLs (APLLs) including avoidance of the effects of component tolerances, drifts, possibilities of real-time processing of the input signal and ease of fabrication.

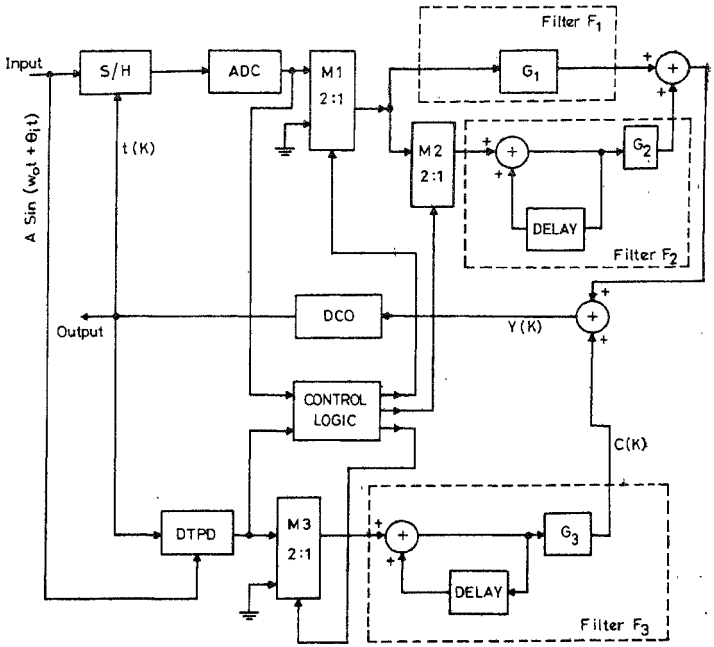

FIG. 1. New DPLL block schematic.

Keeping these advantages in view, it was decided to consider an approach using the DPLL for network synchronization.

2. DPLL implémentation: a new approach

While the use of DPLLs for this application has been reported, techniques for the avoidance of cycle slips during acquisition and consequently of the reduction in the acquisition time do not seem to have received the attention they merit. Considering these factors, a detailed investigation was conducted on DPLLs with particular reference to the avoidance of cycle slips and reduction in the acquisition time. This has resulted in a new DPLL with improved performance characteristics, suitable for application in network synchronization. Figure 1 shows the block diagram of the DPLL, which comprises a digital time period difference detector (DTPD), multiplexers (M_1–M_3), Filter F_3, and a control logic, in addition to the building blocks employed in a conventional second-order DPLL. DTPD aids DPLL in frequency acquisition, by providing a signal proportional to the time period difference between the input signal and the DPLL output. The

Table I
Computer simulation results
(a) : Acquisition time in step number as a function of K_1[1]

K_1'	*Conventional DPLL*	*New DPLL*
1·3	35	4
1·2	4	2
1·1	6	3
1·0	4	3
0·9	5	4
0·8	8	4
0·75	9	5
0·5	16	8

DPLL parameters : $G_3 = 1$, $K_t = 1$; $r = 2$
Initial conditions : 0, 1·0 rad

(b) Cycle slips as a function of initial conditions (@ $K_1' = 1$)

Initial conditions (rad)	*Convergence step number*	
	Conventional DPLL	*New DPLL*
0, 2·59	12 (2)*	5
0, 2·63	(14)**	5
0, 2·65	20 (4)	5

* Figures in brackets indicate no. of cycles slipped.
** No convergence up to 30 steps.

control logic with the aid of M_1–M_3 suitably configures the DPLL for frequency/phase acquisition and tracking modes. The analytical, computer simulation and experimental studies pertaining to this, and the results obtained therefrom are described in this work.

3. Results and conclusions

The performance of both new and conventional DPLLs has been analysed and compared by analytical, computer simulation and experimental methods. These have clearly shown a reduction in the acquisition time and the avoidance of cycle slips during acquisition. An overview of the simulation results for both the new and conventional DPLL, for different input frequencies (K_1') and initial phase errors ($\phi[0]$, $\phi[1]$) is given in Table I. Significant contributions and conclusions as a result of this investigation include:

(a) The derivation of equations for acquisition behaviour and stability conditions using the fixed point and contractive mapping theorems for the new DPLL together with its computer simulation study.

(b) Experimental realization of both the new DPLL and conventional DPLL in the laboratory making use of the state-of-art ICs and a 65C02 μP kit to verify the performance improvement achieved.

(c) The tracking performance of the new DPLL is similar to that of the conventional second-order DPLL, *viz.*, it has a frequency memory which makes it tolerant to signal fadeouts and it possesses narrowband noise rejection and jitter suppression properties.

(d) For the new DPLL there is a reduction in the number of acquisition steps and therefore in the acquisition time.

(e) The new DPLL acquires frequency and phase lock for all the initial phase-error conditions, with the avoidance of cycle slips.

References

1. LINDSEY, W. C., GHAZVINIAN, F., HAGMANN, W C. AND DESSOUKY, K — Network synchronization, *Proc. IEEE*, 1985, **73**, 1445–1467.
2. — *Transmission systems for communication*, Fifth edn, 1982, Bell Telephone Labs
3. LINDSEY, W C. AND CHIE, C. K. — A survey of digital phase locked loops, *Proc IEEE*, 1981, **69**, 410–443
4. OSBORNE, H. C. — Stability analysis of an nth power DPLL–Parts I & II; First-, second- and third-order DPLLs, *IEEE Trans.*, 1980, **28**, 1343–1364.
5. BERNSTEIN, G. M., LIEBERMAN, M. A. AND LICHTENBERG, A J — Nonlinear dynamics of digital phase locked loops, *IEEE Trans*, 1989, **COM-37**, 1062–1070.

Thesis Abstract (M.Sc.(Engng))

A parallelizing compiler for Pascal by Maulik A. Dave.
Research supervisor: Y. N. Srikant.
Department: Computer Science and Automation.

1. Introduction

Compilers which convert sequential programs into parallel programs are known as parallelizing compilers[1]. Parallelizing compilers try to create a parallel program consisting of parallely executable processes out of a sequential program.

1.1. *Why or why not parallelizing compilers?*

The approach of using parallelizing compilers offers the following advantages over the other approach of writing parallel programs.

(1) *Use of existing software packages*

Most of the software in existence is in sequential languages. We believe that rewriting all of them in parallel languages is much more expensive than restructuring them by parallelizing compilers.

(2) *Program portability*

To avoid writing a separate parallel program for each kind of parallel machine, one can write a single sequential program and use a parallelizing compiler to restructure them. This is more advantageous because a major part of a parallelizing compiler is machine-independent (only the code generator is different just like in an ordinary compiler), and hence can be used for various kinds of machines with only a little one-time extra effort. Thus parallelizing compilers improve program portability.

(3) *Training facilities not needed*

It is difficult to train non-computer science programmers in parallel algorithms and languages. Parallelizing compilers avoid all such extra strain on the programming community.

Unfortunately, parallelizing compilers have the following disadvantages also.

(a) To detect fine-grain parallelism in sequential programs, the required amount of compilation time is very large.

(b) Full parallelism is not detected by parallelizing compilers, specially in the presence of arrays.

(c) There are some problems for which efficient parallel algorithms have been found but present-day parallelizing compilers are not able to convert the corresponding sequential programs into efficient parallel ones.

In spite of all these disadvantages, the advantages specially (1) and (3) above seem to be overwhelming the disadvantages and hence a number of parallelizing compilers are being built all over the world.

2. A brief overview of parallelization

The output of a sequential program is the output of the statements executed according to their textural sequencing. However, for a program, the same output can sometimes be achieved by a different ordering of the statements also. The total ordering imposed by a sequential language is more restrictive than is necessary to guarantee a program's output. The required ordering is a partial ordering as opposed to the total ordering of the sequential execution. This phenomenon is exploited during determination of parallelism in sequential programs.

Dependence is a relation among the statements of a program. A statement S2 is dependent on statement S1 if S1 must be executed before S2 in order to preserve the semantics of the original program. Under this definition, dependence represents the essential orderings within a program. Any execution order that preserves a program's dependence also preserves its output.

Now we explain two main types of dependences, *viz.*, data dependence and control dependence. Consider the following two statements, S1 and S2.

S1 : a : = b + c;

S2 : d : = a + c;

Since S2 uses the value of 'a', which is changed by S1, these two cannot be executed in parallel. S2 is dependent on S1 due to data considerations. Now consider the following two statements, S3 and S4·

S3 : if (a <> ϕ) then

S4 : b : c + d;

S3 and S4 cannot be executed in parallel because execution of S3 controls whether S4 has to be executed or not. This is control dependence.

To determine data dependence in the presence of array references and pointers is very difficult and sometimes impossible. For example, consider the following statements, S5 and S6:

S5 : a[i + 1] : = b + c ;

S6 : d : = a[j + 1];

To determine dependence of S5 and S6 completely at compile time is impossible because, in S5, we do not know which element of 'a' is going to be changed and in S6, we do not know which element of 'a' is going to be used. The subscript analysis methods yield information regarding possible dependence only and not complete dependence as in statements S1 and S2 above.

The task of a parallelizing compiler can be divided into two parts: (1) transforming the input program into intermediate representation (with parallelism explicit), and (2) transforming intermediate representation to machine code.

The first part depends on the type of architecture of the machine for which the compiler is going to generate code. However, it does not depend on specific machine characteristics. For example, the first part of a parallelizing compiler will be the same for all kinds of multiprocessors with shared memory, but will differ for multiprocessors and vector processors. The second part will need machine details such as the number of processors, type of processors, services provided by the operating systems, etc. It is because

of this reason that portability of the first part is higher than that of the second part and it can be dealt with separately.

The first part can be further divided into:

(1) Generation of intermediate code with only sequential features. This is the same as in any usual compiler.

(2) Dependence analysis of the above intermediate code using the techniques of dataflow and control flow analysis. The aim of such analysis is to detect parallelism in programs.

(3) Conversion of the intermediate code in (1) above into one having parallel constructs also. Here we use the dependence information computed in (2) above.

3. A parallelizing compiler for Pascal

We have implemented a parallelizing compiler for Pascal which is based on certain new concepts and also some of the older well-proven concepts.

Most of the parallelizing compilers have been written for Fortran. We have chosen Pascal because it has extra features such as recursion, pointers, record structures, nesting of procedures, etc.

The aim of our compiler is to extract as much parallelism as possible in a reasonable amount of time. We observe that shared memory multiprocessors do not have a large number of processors. We have not detected fine-grain parallelism because it is not useful on shared memory mutliprocessors (because of the small number of processors and also the scheduling overheads) and the compilation time may become very large. We have not used symbolic computation either because of the same reason, *viz.*, compilation time becoming very large.

Instead of going in for flowgraphs, we have designed and implemented a new intermediate form called boxgraphs in our compiler. Boxgraphs have the following advantages over flowgraphs:

(i) Boxgraphs do not contain cycles, so the analysis becomes much easier.

(ii) Boxes are sufficiently large, so the scheduling overheads are not considerable.

(iii) Each boxgraph can be analyzed separately. Hence, parallel algorithms can be easily developed for analyzing boxgraphs (future work)

(iv) For block-structured languages boxgraphs can be constructed very easily.

(v) There is a provision to display parallelism explicitly using boxgraphs.

An algorithm has been implemented to carry out simple and interprocedural dataflow analysis and array subscript analysis, and hence to detect parallelism in boxgraphs and to convert them into the boxgraphs depicting parallelism explicitly.

We have implemented our compiler on ORG Supermax machine, a shared memory multiprocessor with two 68020 processors running on UNIX operating system V.3. We have implemented dynamic scheduling of processes and parallelism has been achieved using the features available in operating system UNIX V.3. The implementation, we believe, is a good test bed to try out experiments with parallelizing compilers.

References

1. WOLFE, M. J. *Optimizing supercompilers for supercomputers*, 1989, Pitman.

Thesis Abstract (Ph.D.)

Solids with crystallographically forbidden symmetries–Aperiodic tilings and quasicrystals by S. Baranidharan.
Research supervisors: E. S. Raja Gopal and V. Sasisekharan.
Department: Physics.

1. Introduction

Solid phases exhibiting noncrystallographic symmetries in addition to long-range order are of recent interest. The original discovery by Shechtman *et al*[1] on the existence of an intermetallic alloy which diffracts like an ordinary crystal but has the crystallographically disallowed five-fold symmetry has sparked off a considerable amount of investigations into a wide variety of materials[2]. Various models[3] have been proposed for these phases including aperiodic tilings which fill the space completely. The presence of the forbidden rotational symmetry and hence the aperiodic ordering in the diffraction patterns inhibits the progress towards an experimental structure solution of these phases, otherwise known as quasicrystals.

2. The present work

This work concerns itself with the various aspects of modelling the aperiodic structures in the form of geometric tilings in the two-dimensional plane and also with experimental analyses of a few selected materials exhibiting five-fold symmetry.

The principle of self similarity of geometric building blocks has been used to construct aperiodic tilings with various symmetries. It is shown that aperiodic tilings can be generated with crystallographically allowed (2,3,4,6) and disallowed symmetries using the self-similarity concepts[4]. Thus it is the first report on the possibility of aperiodic tilings with 2,3,4,6-fold symmetries. An analysis into aperiodic tilings with five-fold symmetry shows that one can find approximate large square cells in such tilings. This would be of considerable use in approximating the experimental structure solution of the quasicrystal to a large cubic cell. It is also shown that the method of intersecting decagons can be successfully used to construct defect-free aperiodic tilings with five-fold symmetry[5] without retracing the already generated coordinates.

The diffracting properties of finite-size aperiodic tilings with five-fold symmetry have been studied. These tilings with unit scatterers at the vertices show appreciable variations in the positions and intensities of peaks in their diffraction patterns, when the number of scatterers is below 300. The characteristic diffraction patterns of aperiodic tilings with 2,3,4,5,6,8,10,12-fold symmetries have been displayed. These will be useful for a comparative study of diffraction from quasi- and incommensurate crystals.

The quasicrystalline phase in Al_6CuLi_3 intermetallic alloy has been investigated using electron diffraction, differential scanning calorimetry and x-ray diffraction techniques. The original alloy prepared by directional solidification and slow casting predominantly contained the icosahedral phase. The electron diffraction pictures and the microstructures near the various symmetry axes showed the presence of large-size grains in the matrix. Figure 1 shows the electron diffraction pattern along a five-fold symmetry axis. The differential scanning calorimetry studies showed the existence of a reversible transformation of the icosahedral quasicrystalline phase to a high temperature phase at about 391°C. Further heating of the sample above the transition temperature resulted in a loss of lithium. This phase transition is another new result considering the fact that similar earlier experiments by others did not yield this information. It occurs at a heating rate of 10°/min and gets suppressed at higher heating rates.

Single-grain fragments of quasicrystals from the Al–Cu–Li alloy were subjected to standard single-crystal x-ray diffraction experiments. The Weissenberg, rotation and precession photographs were taken to characterize the grain. The precession photographs established the icosahedral symmetry of the grain. It was also found that the x-ray reflections could be indexed to a large body-centered cubic

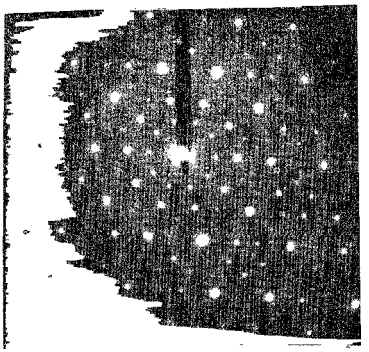

FIG. 1. The selected-area diffraction pattern along a five-fold axis from the Al–Cu–Li quasicrystal.

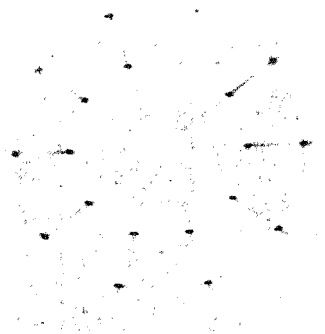

FIG. 2. The zero-level x-ray precession photograph along a five-fold axis from the Al–Cu–Li quasicrystal.

structure of lattice parameter 60 Å. Figure 2 shows the zero-level x-ray precession photograph along a five-fold axis. Various higher-layer precession photographs also have been shown. All the reflections could be either interpreted as arising from a quasicrystal or from a large cubic structure.

The structural aspects and stability of Al–Mn and Al–Fe rapidly solidified alloy ribbons were studied using electron diffractrion, powder x-ray diffraction and resistivity measurements under high pressure. The quasicrystalline phase which is present along with other crystalline phases in these ribbons was found to undergo a first-order-like irreversible phase transition under quasihydrostatic pressures generated in Bridgman anvil high-pressure arrangement. The resistivity behaviour under high pressure is found to be similar to metallic glasses. These results are compared with other results in literature.

References

1. SHECHTMAN, D., BLECH, I., GRATIAS, D. AND CAHN, J. W. — *Phys. Rev. Lett.*, 1984, **53**, 1951–1953
2. GRATIAS, D. AND MICHEL, L. (eds) — International workshop on a periodic crystals. *J. Phys.*, 1986, **47**, C3-1–C3 498
3. STEINHARDT, P. J. AND OSTLUND, S. — *The physics of quasicrystals*. 1987, World Scientific
4. SASISEKHARAN, V. — *Pramana*, 1986, **26**, L283–L293
5. PENROSE, R. — *Bull. Inst. Math. Appl.*, 1974, **10**, 266–271

Thesis Abstract (Ph.D.)

Optical investigations on alkali metal periodates and perchlorates by T. A. Al-Dhahir.
Research supervisor: H.L. Bhat.
Department: Physics.

1. Introduction

Alkali metal periodates and perchlortes belong to the family of compounds represented by the general

FIG. 1 Ferroelastic domains in $CsIO_4$ viewed through polarized light

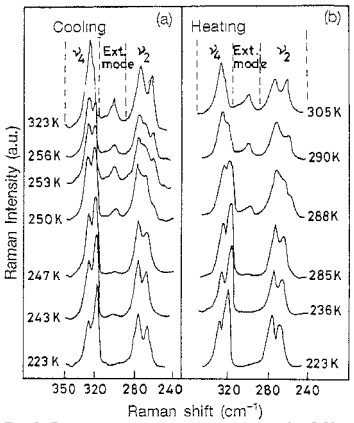

FIG. 2 Raman spectra in various temperatures for $CsIO_4$ in the (a) cooling, and (b) heating run

formula MXO_4 (where M = K, Rb or Cs and X = I or Cl) At room temperature the three perchlorates and cesium periodate crystallize into orthorhombic Pnma structure[1,2], where K and Rb periodates crystallize into scheelite structure with space group $I4_1/a^{2,3}$. It is well established that the perchlorates of K, Rb and Cs exhibit high-temperature phase transition to cubic structure (space group Fm3m) at 579, 544, and 497K, respectively[1]. Physical data on single-crystal periodates are rare. The reported phase transition of $CsIO_4$ at 423K is the only study of its kind available in literature[4] This is probably because of the difficulty in growing them which is due to their very low solubility in water and their decomposition on or before melting. It was therefore considered worthwhile to grow crystals of the above-mentioned materials and then to investigate the structural phase transitions exhibited by them The phase transitions are investigated through static and dynamical optical properties like birefringence, light transmission, optical microscopy and light scattering through Raman spectroscopic studies.

2. Results and discussion

2.1. *Crystal growth*

As the first step in fulfilling the above objective, single crystals of alkali metal periodates and perchlorates were grown by employing the gel technique. While considerable information was available on the growth of alkali metal perchlorates such information was lacking on the growth of alkali metal periodates In particular, the growth of $CsIO_4$ was further complicated on account of its unfavourable habit From this point, growth of $CsIO_4$ crystals of 1 cm lateral dimension and about 3 mm thickness is no small an achievement. By careful experimentation, growth conditions were optimized in the double-diffusion apparatus. The best results were obtained with 0·5 M concentration of cation and anion feed solutions and gel of pH = 4. General characterization carried out on the K, Rb and Cs periodate crystals clearly revealed the similarities and dissimilarities between them.

2.2 *Optical studies on $CsIO_4$*

$CsIO_4$ turned out to be an interesting system. This crystal exhibited phase transitions, both above and

below room temperature. To understand the nature of these phase transitions birefringence, light–transmission optical microscopy and Raman spectroscopy[5-7] were employed. Our experiments clearly established the first-order nature of the high-temperature phase transition exhibited by this crystal. From microscopy observation of domains (Fig. 1) it is established for the first time that the room temperature phase of $CsIO_4$ is ferroelastic[5,6]. From the analysis of ferroelastic domains and their orientation states the point group of high-temperature phase is suggested to be 4/mmm and the transition to be of type 4/mmm Fmmm (p). Further, by working through the pseudo-symmetry relation it is proposed that the high-temperature space group of this crystal could be $I4_1/acd$.

2.3. *Raman spectroscopic studies*

Polarized Raman spectroscopic studies carried out across the high-temperature phase transition in $CsIO_4$ strongly indicated that the transition is of order–disorder type. It is also inferred that the local site symmetry of IO_4 anion both in room temperature and high-temperature phases is C_S and the phase transition is weak first order in nature.

The low-temperature Raman study of this crystal yielded very interesting results. The spectra displayed marked change at 256 and 244K during cooling cycle, then between 287 and 291K during heating cycle (Fig. 2). From the analysis of the spectra it is suggested that transition at 256K is from normal to incommensurate phase which changes to a commensurate structure at 244K. This phase transition is accompanied by thermal hysteresis which is understood to arise due to pinning of discommensuration by impurities[8].

Polarized Raman spectroscopic studies of KIO_4 and $RbIO_4$ conformed to the group theoretical predictions and selection rules fairly well. High-pressure Raman study on KIO_4 showed a pressure-induced phase transition in which normal and high-pressure phases coexist over considerable pressure range (6·5–9·8 GPa).

2.4. *Optical studies on alkali metal perchlorates*

The birefringence, light transmission and microscopy studies on K, Rb and Cs perchlorates clearly suggested that the high-temperature phase transitions occurring in these crystals are ferroelastic–paraelastic of type m3m Fmmm(ss)[9] The number of crystallographically permissible domain walls in such a transition being as high as 21, the observed domain structure should look very complicated and this is what has been actually observed experimentally.

References

1. Rao, C. N. R. and Prakash, B. — *NBS Reference data series 56*, National Bureau of Standards, Washington, DC, 1975, and references therein.
2. Beintema, J. — *Z. Kristallogr.*, 1937, **97**, 300–322.
3. Hyllerass, E. — *Z. Phys.*, 1926, **39**, 308–312.
4. Arend, H., Granicher, H., Helg, G. and Hofmann, R. — *Helv. Phys. Acta*, 1970, **43**, 484–485.
5. Al-Dhahir, T. A., Raghurama, G. and Bhat, H. L. — *Phase Transition*, 1988, **12**, 205–214.
6. Al-Dhahir, T. A., Raghurama, G. and Bhat, H. L. — *Ferroelect. Lett.*, 1988, **8**, 49–53
7. Al-Dhahir, T. A., Chary, B. R., Bhat, H. L., and Narayanan, P. S. — *Indian J. Pure Appl. Phys.*, 1988, **26**, 239–245
8. Al-Dhahir, T. A., Sood, A. K. and Bhat, H. L. — *Solid St. Communs*, 1989, **70**, 863–868.
9. Raghurama, G., Al-Dhahir, T. A., and Bhat, H. L. — *J. Phys. C.*, 1987, **20**, 4505–4511.

Thesis Abstract (Ph.D.)

Electrical and spectroscopic investigations of phase transitions in ferroelastic TAAP and DTAAP by M. N. Shashikala.
Research supervisor: H. L. Bhat.
Department: Physics

1. Introduction

Monoclinic telluric acid ammonium phosphate [$Te(OH)_6$. $2NH_4H_2PO_4$. $(NH_4)_2HPO_4$] referred to as TAAP is a recently discovered ferroelectric with its physical properties comparable to those of tryglycine sulphate[1]. It undergoes a second-order phase transition at 45°C. In fact, when compared to TGS, it exhibits several advantages such as no cleavage plane, neither brittle nor plastic, no mechanical stresses or strains when grown, insensitive to thermal variations, possibility of growing large and macro defect-free crystals[2]. Because of its better mechanical and geometric properties, TAAP is considered a potential replacement for TGS in pyroelectric detection and imaging. However, on account of its being a recently discovered ferroelectric material, all its physical properties have not yet been completely investigated. We have therefore undertaken detailed studies on the ferroelectric properties of this new crystal and its deuterated analogue across the phase transition and the results obtained during these investigations form the main body of this work.

2. Experimental work

Optical-quality single crystals of TAAP were grown at 33°C by slow evaporation from the aqueous solution of telluric acid, ammonium hydrogen phosphate and diammonium hydrogen phosphate mixed in required proportions[3]. The deuterated analogues of the crystals were grown from heavy water with an isotopic purity of 99·4 per cent at 10°C for effective deuteration[4].

The following experiments have been carried out to study the various properties of TAAP and DTAAP.

(1) Dielectric measurements were carried out using Hp 4275 model multifrequency LCR meter. The data were fed to an IBM personal computer to plot the dielectric constant *vs* temperature.

(2) High-pressure experiments have been carried out employing an EN24 steel piston cylinder type of pressure cell with liquid paraffin as pressure-transmitting medium.

(3) Spontaneous polarization was measured with modified Sawyer–Tower circuit at 50Hz. All measurements were carried out on (101) crystal plates with air-drying silver paste as electrodes.

(4) Raman spectra of the crystals were recorded using a Spex double monochromator with a photon-counting system. An argon laser (Spectra–Physics) operating at 4880 Å with a power output of 150 mW was used to excite the Raman spectra.

(5) Infrared spectra were recorded in KBr pellets using a Perkin–Elmer model 580 spectrometer.

(6) Switching studies have been carried out employing Merz technique and applying a train of bipolar square pulses with a frequency of 0·2 Hz.

(7) Domain structure in TAAP has been observed by rubbing the crystal face on a smooth cloth, soaked with a solution containing 93 per cent methanol, 5 per cent water and 2 per cent nitric acid. The etching time ranged from 5 to 20 seconds.

3. Results and discussion

Studies of dielectric measurements on TAAP have shown that the crystal exhibits pronounced anomalies at T_c and the dielectric constant follows Curie–Weiss law in both ferro and paraelectric phases. One of the observations made during the present investigation was the dependence of dielectric constant and

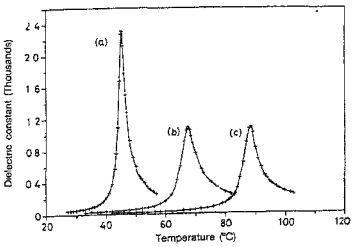

FIG 1. Dielectric constant *vs* temperature for (a) undeuterated, (b) partially deuterated, (c) nearly totally deuterated TAAP.

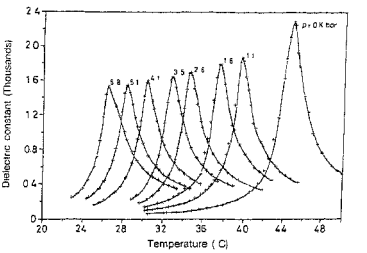

FIG 2 Variation of dielectric constant with temperature of TAAP at different pressures

coercive field on the thickness of the sample. This has been explained on the basis of the presence of surface layers on the crystal. Dielectric relaxation studies of TAAP near Curie temperature have indicated that TAAP undergoes an order–disorder type of phase transition[4]. To examine the role of hydrogen bonds, dielectric measurements on DTAAP were made and it was found that deuteration increases the transition temperature from 45 to 87°C indicating the importance of hydrogen bonds in the ferroelectric behaviour of TAAP[3]. Figure 1 shows the dielectric constant *vs* temperature plots of pure, partially deuterated and nearly fully deuterated TAAP crystals. Pyroelectric measurements on TAAP and DTAAP have shown that DTAAP exhibits a higher pyroelectric coefficient at T_c than TAAP.

The properties of hydrogen-bonded ferroelectrics are generally very sensitive to external pressure. Also, many interesting effects are observed on the application of pressure on ferroelectrics because of the coupling between spontaneous polarization and strain. Accordingly, we have carried out the effect of pressure on ferroelectric properties of TAAP and DTAAP up to 6 Kbars. One of the main effects of pressure was to decrease the transition temperature significantly similar to the behaviour of other well-known hydrogen-bonded ferroelectrics like KDP, LHS, etc. In the case of TAAP, the value of dT_c/dp is −2·6°C/Kbar and for DTAAP the value is −1·65°C/Kbar. Figure 2 shows the variation of dielectric constant with temperature at different pressures for TAAP. The behaviour of dielectric properties with pressure could be explained successfully on the basis of thermodynamic theory[5].

A systematic study of vibrational frequencies and bandwidths across the phase transition is expected to give more information on the nature of the phase transition of the crystal. Raman spectroscopic studies of TAAP and DTAAP carried out across the phase transition clearly suggest an order–disorder model for the phase transition and do not give any evidence for a displacive model. This conclusion was based on the temperature dependence of the phonon frequencies where no soft mode was observed. The width and intensity of the stretching bands of hydrogen bonds are known to be very sensitive to changes that take place across phase transition. The vibrational spectra of the hydrogen bond region of TAAP and DTAAP show considerable broadening across T_c. Also, the vibrational spectra of PO_4 groups which participate in the hydrogen bonding show variations in the shape and width across T_c, indicating that the cooperative phenomena involving PO_4 groups and hydrogen bonds is responsible for the phase transition.

Finally, we present the results of our switching studies and the effect of irradiation on the ferroelectric properties of TAAP and DTAAP. Figure 3 shows the plots of $1/t_m$ *vs* E at various temperatures. These results show that the switching process in this crystal is predominantly governed by a linear forward growth process of the domains. Also, it was found that the switching process in TAAP is slower than in TGS and of DTAAP slower than TAAP. X-ray irradiation brings about noticeable changes in the ferroelectric properties of TAAP. It increases the coercive field there by increasing the threshold field below which the switching could not occur and decreases the dynamic mobility of the domains. Domain-structure studies

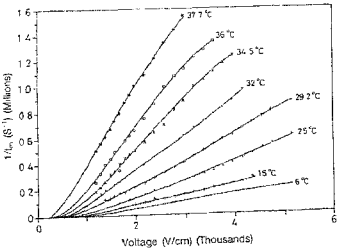

FIG 3. Dependence of reciprocal of switching time $1/t_m$ as a function of external field at different temperatures.

on TAAP revealed that it grows both as predominantly single domain and multidomain crystals depending on which the internal bias increases or remains unaffected upon irradiation. Irradiation also decreases the peak value of dielectric constant and the transition temperature.

References

1. NICOLAU, Y. F. — Single crystal growth of tellûric acid ammonium phosphate (TAAP), *Ferroelectrics*, 1984, **52**, 281–291.
2. GUILLOT GAUTHIER, S., PEUZIN, J. C., OLIVER, M. AND ROLLAND, G. — Monoclinic telluric acid ammonium phosphate, a new ferroelectric compound, dielectric and related properties, *Ferroelectrics*, 1984, **52**, 293–306.
3. SHASHIKALA, M. N., SANGUNNI, K. S. AND BHAT, H. L. — Ferroelectricity in DTAAP, *Ferroelectrics Lett.*, 1988, **9**, 19–25.
4. SHASHIKALA, M. N., SRINIVASAN, M. R. AND BHAT, H. L — Dielectric relaxation in ferroelectric TAAP near the Curie temperature, *J. Phys: Condensed Matter*, 1990, **2**, 4013–4015.
5. SHASHIKALA, M. N., BHAT, H. L. AND NARAYANAN, P. S. — Effect of pressure on the ferroelectric properties of TAAP, *J. Phys. Condensed Matter*, 1990, 2, 5403–5408

Thesis Abstract (Ph.D.)

Design and characterization of bifunctional oxygen electrodes for metal/air batteries by A. M. Kannan.
Research supervisor: A. K. Shukla.
Department: Solid State and Structural Chemistry Unit.

1. Introduction

Metal/air batteries differ from other types of batteries in storing only one of the reactants while using atmospheric oxygen as the cathodic reactant. A major advantage of metal/air batteries over conventional batteries is their potentially high-specific energy density arising due to the low equivalent weight of oxygen as compared to other battery reactants with the exception of hydrogen and lithium. However, the major

limitations of metal/air cells that prevented their widespread application have been their low-specific power density and non-rechargeability. Both the limitations relate to the air electrode.

During recharge of a metal/air battery, oxygen is evolved at the air electrode according to the reaction:

$$4\ OH^- \rightarrow O_2 + 2H_2O + 4e^- \ (E_{rev} = 0{\cdot}3\ V\ vs\ Hg/HgO,\ OH^-).$$

At the high positive potential required for this reaction to proceed at a significant rate, undesirable side effects, *viz.*, corrosion and/or erosion of the electrode support and the electrocatalyst layer, have been observed. For these reasons, designing of a bifunctional air-electrode remains a challenging technical target even today.

2. Present work

In this study, an attempt has been made to develop bifunctional air-electrodes for alkaline metal/air cells in an electrode configuration which circumvents the associated corrosion and erosion problems. As metallic oxides seem to be attractive catalysts for sustaining both oxygen reduction (ORR) and oxygen evolution (OER) reactions, an objective of the present study has been to engineer oxide catalysts capable of sustaining ORR and OER. To this end, various transition-metal oxide catalysts belonging to spinel (AB_2O_4), perovskite (ABO_3) and pyrochlore ($A_2B_2O_6O'_{1-y}$) families have been explored.

After a brief introduction to the electrochemical features of metal/air cells, preparation and characterization of various fluon-bonded bifunctional air-electrodes employing spinel and perovskite oxides are described. The porous structure of the fluon-bonded oxide electrodes has been optimized using a factorial optimization method with respect to binder composition, compaction pressure and compaction time in a specific electrode configuration so as to attain an optimum performance both towards ORR and OER[1]. Galvanostatic polarization and voltammetric studies have been conducted in 6 M KOH to characterize various oxide electrodes. The electrochemical experiments are interfaced to an indigenously developed data-acquisition system driven by a microprocessor[2]. Of the various perovskite oxides investigated, electrodes with $LaNi_{0{\cdot}8}Co_{0{\cdot}2}O_3$ oxide could sustain load currents of 80 mA/cm^2 for oxygen reduction reaction and 180 mA/cm^2 for oxygen evolution reaction with respective polarization values of 0·45 V and 0·35 V from E_{rev}.

Among oxide pyrochlores, $Pb_2Ir_2O_6O'_{1-y}$, $PbBiRu_2O_6O'_{1-y}$ (a solid solution of $Pb_2Ru_2O_6O'_{1-y}$ and $Bi_2Ru_2O_7$) and $Bi_{1{\cdot}5}Tl_{0{\cdot}5}Ru_2O_6O'_{1-y}$ (a solid solution of $Bi_2Ru_2O_7$ and $Tl_2Ru_2O_7$) are identified as efficient bifunctional catalysts for sustaining oxygen reduction and evolution reactions. The electrodes employing $Pb_2Ir_2O_6O'_{1-y}$ could safely sustain a load current density of 100 mA/cm^2 at a polarization of about 200 mV from the rest potential in the cathodic mode and at a polarization of 100 mV in the anodic mode[3]. To characterize these oxide pyrochlores, x-ray photoelectron and x-ray absorption spectroscopic studies have been conducted. It is found that the electro-catalytic activity of these oxides is dictated by the nature of the counter cation present in them which forces the oxygen 2p-band and the B-metal d-band to pull closer facilitating the oxygen lability in the oxide framework. Such a situation supports oxygen evolution reaction occurring through B(IV)–O^- surface species made accessible by B(IV/V) redox couple lying close to the top of the O^{2-} ($2p^6$) valence band. The reduction of oxygen on these oxides occurs through exchange of surface OH^- species with adsorbed O_2^- species present in solution.

To examine the technical viability of these air-electrodes, prototype rechargeable alkaline iron/air cells utilizing pressed-type iron electrodes and bifunctional air-electrodes of $Pb_2Ir_2O_6O'_{1-y}$ as well as $PbBiRu_2O_6O'_{1-y}$ pyrochlore oxides have been fabricated. The cells have been successfully cycled for about 150 charge–discharge cycles without any deterioration.

References

1 KANNAN, A. M., SHUKLA, A. K. AND SATHYANARAYANA, S. — Oxide-based bifunctional oxygen electrode for rechargeable metal/air batteries, *J. Power Sources*, 1989, **25**, 141–150.

2. KANNAN, K. R., KANNAN, A. M. AND SHUKLA, A. K. — A low-cost computer-aided electrochemical system for characterizing battery electrodes, *J. Power Sources*, 1990, **32**, 99–104.

3. KANNAN, A. M., SHUKLA, A. K. AND SATHYANARAYANA, S. — A lead-iridium pyrochlore-based bifunctional oxygen electrode, *J. Electroanal. Chem.*, 1990, **281**, 339–344.

Thesis Abstract (Ph.D.)

Layered transition metal thiophosphates: A study of their properties and intercalation chemistry by P. A. Joy.
Research supervisor: S. Vasudevan.
Department: Inorganic and Physical Chemsitry.

1. Introduction

Metal chalcogenophosphates are a class of layered compounds with the general formula MPX_3 where M is usually a transition metal and X is S or Se[1]. The basic building blocks of the structure are MX_6 and P_2X_6 polyhedra which are edge shared to form sheets. The transition metal chalcogenophosphates happen to be one of the few layered compounds which are magnetic. These materials have been reported to have a rich and original intercalation chemistry[2].

2. Present study

The objective of the present study is to try and understand the nature of intercalation as well as the various changes accompanying intercalation in the transition metal thiophosphates. The study is restricted to the thiophosphates of Mn, Fe and Ni and the intercalating species to pyridine and *n*-alkylamines.

A detailed investigation of the optical, magnetic and vibrational properties of the host crystals of $MnPS_3$, $FePS_3$ and $NiPS_3$ has been carried out to get a coherent picture of the nature of bonding in the thiophosphates.

Optical absorption spectra of single crystals were analyzed and assigned to various transitions within the d electron manifold of the corresponding transition metal ion. The crystal field parameters Dq, B, C and λ were evaluated in the weak field limit of the crystal field theory. The B parameters for these compounds are close to the corresponding free ion values, B_0, implying that the d electrons are localized and fairly ionic.

Anisotropic magnetic susceptibility was measured as a function of temperature. The magnetic behaviour is typical of 2d antiferromagnetic systems with a broad maxima well above the Neel temperature. For all the compounds the transition metals are in the high spin state. The magnetic behaviour of $MnPS_3$, $FePS_3$ and $NiPS_3$ reveals the critical role of the trigonal distortion of the MS_6 octahedra in deciding the nature and symmetry of the magnetic interactions. Although all the three compounds are isostructural, the effects of trigonal distortion are quite different. In $MnPS_3$, where the effect is negligible, it leads to symmetric Heisenberg interactions. In $FePS_3$, the contribution of the trigonal distortion as well as spin-orbit coupling gives rise to highly anisotropic magnetic interactions so that $FePS_3$ is best described by the Ising Hamiltonian. In contrast, the effect of trigonal distortion and spin-orbit coupling in $NiPS_3$ causes the spins to lie in the basal plane and the system is best represented by the anisotropic Heisenberg Hamiltonian.

Infrared spectra of both single crystals and powders of $MnPS_3$, $FePS_3$ and $NiPS_3$ were recorded to obtain the $\vec{E} \parallel \vec{c}$ and $\vec{E} \perp \vec{c}$ active modes of vibrations. The spectra of all the three compounds are identical and show the same temperature and angular dependence. The normal modes could be separated into internal modes of the 'ethane like' P_2S_6 group and external lattice modes. The normal modes of the thiophosphates were obtained by the correlation method[3]. The vibrational spectra could be consistently interpreted in the ionic limit considering that the interactions are between the positively charged M^{2+} ions and the negatively charged $P_2S_6^{4-}$ groups.

Pyridine intercalated $MnPS_3$ powder and single crystals were characterized by XRD and TGA. Two types of intercalated compounds have been identified, one with a lattice expansion of 5·9Å and the other with a lattice expansion of 3·4Å. On the basis of the results obtained from thermal deintercalation mass spectra, EPR, vibrational and Raman spectra and magnetic susceptibility measurements, a mechanism is proposed for the mode of intercalation of pyridine in $MnPS_3$. The intercalated species are found to be

the protonated pyridinium cations solvated by neutral pyridine molecules in the 5·9Å phase and by water molecules in the 3·4Å phase. Charge neutrality is preserved by the removal of Mn^{2+} ions from the lattice-creating defects in the host structure. The mechanism is also to explain all the observed properties including the weak ferromagnetism of the intercalated sample.

The spin dynamics in $MnPS_3$ and pyridine-intercalated $MnPS_3$ single crystals were investigated by EPR spectroscopy. EPR spectra of the crystals were recorded as a function of temperature and orientation of the crystal with respect to the magnetic field. The spectra were examined in the light of the theory of exchange-narrowed EPR spectra in low-dimensional systems[4] by analysing the angular and temperature dependence of linewidths and line shapes. For $MnPS_3$, the results indicate considerable short-range correlations among spins even at temperatures much above the critical temperature. The angular variation of linewidth shows a $1 + \cos^2\theta$ dependence and the line shapes have predominant Gaussian character. The angular variation of line shape and EPR-integrated intensities indicate that spin-spin correlations are much stronger for spins within a layer than those between the layers, confirming the 2d nature of the magnetic interactions in these systems.

In the pyridine-intercalated $MnPS_3$, the dominant component in the angular variation of linewidth is the $(3\cos^2\theta - 1)^2$ term. The line shapes also show predominant Lorentzian character. The results have been interpreted in terms of single-ion anisotropy, arising due to manganese ions near a cation vacancy, created during the intercalation reaction. A mechanism for the observed weak ferromagnetism is suggested in terms of canting of spins, the canting occurring because of different single-ion anisotropies due to local distortions in the intercalated samples.

Intercalation of *n*-alkylamines in $FePS_3$ and $NiPS_3$ showed that the amines are oriented flat with respect to the layers in both the compounds, with a lattice expansion of ~ 3·3Å. The reaction is found to proceed by a mechanism where the Fe^{2+} ions come out of the lattice forms Fe_2O_3 with the water molecules present in the intercalated compound. The presence of fine-particle Fe_2O_3 is confirmed from Mössbauer spectroscopic studies as well as by magnetic measurements. The vacancies created by the removal of some of the Fe^{2++} ions cause a distortion of the FeS_6 polyhedra which is seen as a doublet in the Mössbauer spectra with isomer shift identical to that of pure $FePS_3$ but with a different quadrupole splitting.

The observed magnetic susceptibility of amine-intercalated $FePS_3$ is in qualitative agreement with many of the features expected for a Random Field Ising Model (RFIM)[5,6]. The random effects are due to vacancies of Fe^{2+} ions or due to distorted Fe^{2++} sites near a vacancy. The model proposed is able to justify the presence of superparamagnetic Fe_2O_3 as well as a defect Fe_{1-x} PS_3 lattice. The results are further confirmed by electrical, vibrational and EPR spectra and thermal deintercalation mass spectroscopy, etc.

In the case of amine-intercalated $NiPS_3$, a more complex electrical and magnetic behaviour was observed. But the results are explained in terms of the large crystal field stabilization energy of Ni^{2+} which makes it energetically difficult to remove an Ni^{2+} site from the lattice. So the mechanism proposed involves an initial reduction of part of Ni^{2+} to Ni^{1+} by charge transfer from the amine followed by removal of these reduced sites from the lattice which form a separate NiO-like phase. The EPR results as well as the magnetic susceptibility data are in agreement with such an assumption.

The intercalation reactions of the transition metal thiophosphates have been compared and contrasted with those of the well-studied transition metal dichalcogenides. Whereas in the latter, intercalation is truly topotactic and reversible[7], in the former the reaction is more complex and is best described as a substitution–intercalation reaction. The origin of this difference in reactivity has been attributed to the more ionic nature of the metal–ligand interactions in the thiophosphates as compared to the dichalcogenides.

References

1. JOHNSON, J. W. In *Intercalation chemistry* (M. S. Whittingham and A. J. Jacobson, eds), 1982, pp. 267–283, Academic Press.

2. BREC, R. *Solid St. Ionics*, 1986, **22**, 3–30.

3. WIETING, T. J AND VERBLE, J. L.	In *Electrons and phonons in layered crystal structures*, (F Levy, ed), 1979, p.321, D. Riedel.
4. RICHARDS, P. M.	In *Local properties at phase transitions* (K. A. Muller and A. Rigamonti, eds), 1976, pp. 539–606, Societa Italiana de Fisica, Italy.
5. SHAPIRA, Y., RIDGLEY, D. H., DWIGHT, K., WOLD, A, MARTIN, K. P. AND BROOKS, J. S.	*J. Appl. Phys.*, 1985, 57, 3210–3212.
6. SHAPIRA, Y.	*J Appl. Phys.*, 1985, 57, 1938
7. LEVY, F. (ed.)	*Intercalated layered materials*, 1979, D. Ridel.

Thesis Abstract (Ph.D.)

Transition metal organometallic complexes and related derivatives of bis (diphenyl phosphino) isopropylamine and bicyclic-1,3,2λ^3, 4λ^3-diazadiphosphetidines by T. K. Prakasha.
Research supervisor: S. S. Krishnamurthy.
Department: Inorganic and Physical Chemsitry.

1. Introduction

Diphosphazane ligands offer considerable scope and versatility for designing homo and heterobimetallic complexes and the structural features of the resulting complexes can be altered significantly by altering the substituents on both nitrogen and phosphorus atoms[1-5]. In the present study, the reactions of the diphosphinoamine, $Pr^{i}N(PPh_2)_2$ (dppipa) and the bicyclic diphosphazanes [(PhNP)$_2$(--X(CH$_2$)$_2$Y-)] (X = Y = O; X = O, Y = NMe) with group 6 metal carbonyls, iron pentacarbonyl, a range of metal carbonyl derivatives and palladium and platinum derivatives have been investigated. These studies lead to the isolation of several new transition metal complexes in which the acyclic diphosphazane ligand dppipa exhibits monodentate (η^1-mode), bidentate-chelating (η^2-mode) or bridged-bidentate (μ) modes of coordination. The bicyclic diphosphazanes exhibit monodentate or bridged-bidentate modes of coordination. The structures of the complexes have been elucidated by infrared and nmr (^{1}H, ^{13}C and ^{31}P) spectroscopic studies and confirmed in a few instances by single-crystal x-ray diffraction.

1. Transition metal chemistry of dppipa

Thermal reactions of group 6 metal carbonyls, M(CO)$_6$ (M = Cr, Mo, W) with dppipa in boiling toluene afford the chelates *cis*-[M(CO)$_4$ (dppipa–PP')] (M = Cr, Mo or W) (I) in 65–70% yield. A single-crystal x-ray study of *cis*-[W(CO)$_4$-(dppipa-PP')] confirms its structure and reveals the planarity of WP$_2$N ring[6].

The reaction of Fe(CO)$_5$ with dppipa in the presence of trimethylamine-N-oxide (Me$_3$N(O).2H$_2$O) in 1:1:2 molar ratio in CH$_3$CN at 25°C affords the tricarbonyl chelate, [Fe(CO)$_3$(dppipa–PP')] (II) in 80% yield. All the chelates exhibit a high degree of thermal stability.

Reactions of dppipa with the acetonitrile precursor complexes, *fac*-[M(CO)$_3$(MeCN)$_3$] (M = Mo or W) under a variety of experimental conditions afford a range of novel mononuclear and dinuclear complexes (III–VII, Scheme 1). The dinuclear molybdenum complex, III is isolated in pure state whilst the dinuclear complex, V is obtained as a mixture of III and V. In the process of obtaining single crystals (suitable for x-ray analysis) of the dinuclear molybdenum complex, III from diethylether solution, a heterofunctional chelate (IV) is isolated as the oxidized product. Complex IV has been structurally characterized; the five-membered chelate ring deviates from planarity. Carbonyl-free diphosphazane complexes of molybdenum and tungsten (VII) have been prepared by the thermal reaction of *fac*-[M(CO)$_3$(NCMe)$_3$] (M = Mo or W) with an excess of the diphosphazane ligand (dppipa) in boiling MeCN.

Novel heptacoordinated complexes of molybdenum (II) and tungsten (II) have been prepared by the

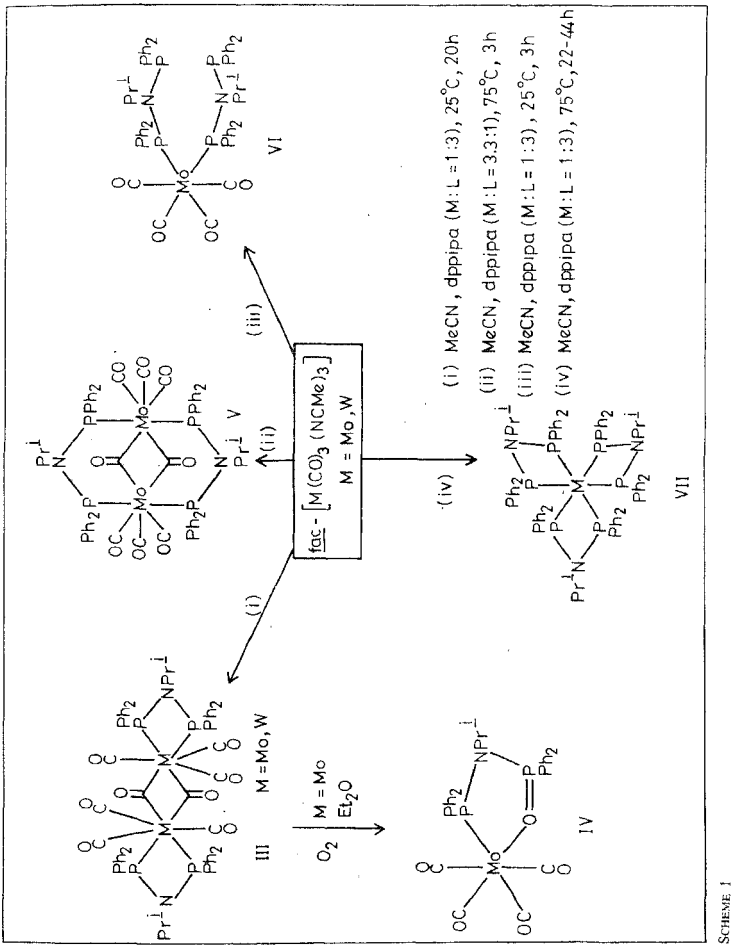
fac - [M(CO)3 (NCMe)3]
M = Mo, W
(i)
(ii)
(iii)
(iv)
(i) MeCN, dppipa (M:L = 1:3), 25°C, 20h
(ii) MeCN, dppipa (M:L = 3:3:1), 75°C, 3h
(iii) MeCN, dppipa (M:L = 1:3), 25°C, 3h
(iv) MeCN, dppipa (M:L = 1:3), 75°C, 22-44h
III M=Mo, W
IV
V
VI
VII
M = Mo
Et2O
O2

SCHEME 1

reaction of dppipa with $[MI_2(CO)_3(NCMe)_2]$ (M = Mo or W) or $[M(Cl)(SnCl_3)(CO)_3(NCMe)_2)]$ (M = Mo or W) generated *in situ*.

Reaction of dppipa with $[C_5H_5Mo(CO)_2]_2$ in boiling benzene yields a complex with a salt-like structure, IX, which transforms into the neutral dinuclear complex, X, when heated under reflux in acetone.

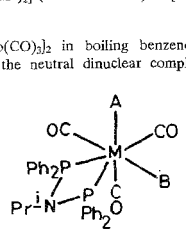

VIII

(M = Mo, W; A = B = I or A = $SnCl_3$, B = Cl)

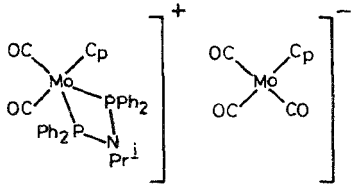

IX ($C_p = \eta^5 - C_5H_5$)

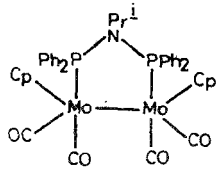

X

Reactions of dppipa with *cis*-$[MCl_2(COD)]$ (M = Pd, Pt; COD = 1,5-cyclooctadiene) yield mononuclear chelates, *cis*-$[MCl_2$ (dppipa-PP')] (XI). The homo- and hetero-dinuclear complexes of Pd(I) and Pt(I), XII have been prepared by the redox condensation reactions of M(II) (M = Pd, Pt) and Pd° complexes.

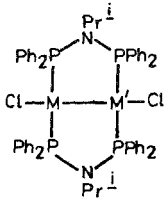

(M = M' = Pd; M = Pd, M' = Pt)

XII

A diphenyl phosphinous acid derivative, XIII is obtained as an hydrolysed product in an attempt to prepare Pt(O) complexes of dppipa. It has not been possible to isolate a Pt(O) complex in contrast to the reaction of $Pt(PPh_3)_4$ with dppm which yields the dinuclear complex, $Pt_2(\mu\text{-dppm})_3$[7].

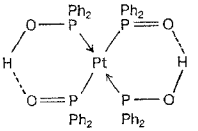

XIII

2. Transition metal chemistry of bicyclic diphosphazanes, [PhNp]$_2$ [−X(CH$_2$)$_2$Y-] (X = Y = 0; X = 0, Y = NMe) (XIV)

Reactions of tetracarbonyl derivatives, *cis*-$[M(CO)_4\text{-}(NHC_5H_{10})_2]$ (M = Mo or W) with the unsymmetrical bicyclic diphosphazane, XIV (X = 0, Y = NMe)[8] yield mononuclear complexes, *cis*-$[M(CO)_4(\eta'\text{-L})_2]$ (XV) (L = XIV) wherein the bicyclic diphosphazane exhibits η'-mode of coordination. From a comparison of the Phosphorus-31 chemical shifts, it is inferred that P–O end of the bicyclic diphosphazane ligand coordinates to metal leaving behind the P–MNe uncoordinated. Treatment of bicyclic diphosphazanes, XIV with *fac*-$[M(CO)_3(NCMe)_3]$ (M = Mo or W) leads to the isolation of the mononuclear complexes, *fac*-$[M(CO)_3(\eta'\text{-L})_3]$ (XIV).

The reaction of XIV (X = Y = 0) with *cis*-$[PdCl_2(COD)]$ yields a complex (XVII) of composition $[Pd(\mu\text{−}L)_2Cl_2]_n$ (L = XIV) (X = Y = 0). In analogy with the results reported by Verkade and co-workers[9], one can tentatively propose a tetranuclear structure for this complex (XVII) as a dinuclear structure with two bridging ligands which will be sterically more unfavourable than a tetranuclear structure.

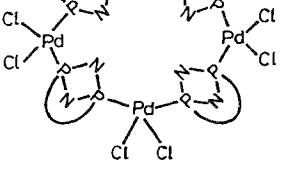

XVII

3. Conclusions

The present investigations on the transition metal chemistry of dppipa and the bicyclic diphosphazanes demonstrate the rich chemistry that can be carried out with these systems. The transition metal chemistry of bicyclic diphosphazanes, although explored only to a limited extent, shows that these ligands can form several interesting complexes exhibitng either η'- or bridged bidentate modes of coordination. The complexes containing pendent diphosphazane ligands can be valuable synthons for the preparation of bimetallic and high-nuclearity clusters.

References

1 KING, R. B — Alkylaminobis (difluorophosphines) Novel bidentate ligands for stabilizing low metal oxidation states and metal–metal bonded systems. *Acc Chem Res*, 1980, **13**, 243–248.

2 DE LEEUW, G., FIELD, J. S AND HAINES, R. J — $[Co_2(CO)_4\{\mu-(CH_2O)_2PN(Et)P(OCH_3)_2\}]$; A molecule with a symmetrical formula but an unsymmetrical structure. *J. Organometal Chem.*, 1989, **359**, 245–254

3 MAGLE, J. T., JOHNSON, M. P AND LLOYD, C. L — Novel trimetallic complexes of rhodium with bis (difluorophosphino) methylamine; The crystal and molecular structure of $[Rh_3(\mu\text{-}Cl)_3(\mu\text{-}H_3CN(PF_2)_2)_3]$, *J Am. Chem. Soc*, 1989, **111**, 5012–5013

4 USON, R., FORNIES, J., NAVARRO, R., TOMAS, M., FORTUNO, C., CEBOLLADA, J. I. AND WELCH, A. J — Synthesis and reactivity of palladium (I) derivatives with bis (diphenylphosphino) amine: X-ray crystal structure of $Pd_2(\mu\text{-dppa})_2Cl_2(CH)_2CO$, *Polyhedron*, 1989, **8**, 1045–1052.

5 KRISHNAMURTHY, S. S. — Organometallic chemistry of diphosphazane ligands, *Proc. Indian Acad Sci. Chem. Sci*, 1990, **102**, 283–290.

6 BALAKRISHNA M. S., PRAKASHA, T. K., KRISHNAMURTHY, S. S SRIWARDANE, U. AND HOSMANE, N. S. — Organometallic derivatives of diphosphinoamines, $X_2PN(R)PX_2$ Reactions with carbonyl derivatives of group 6 metals and iron pentacarbonyl. The crystal structures of $[Mo(CO)_4PhN(P(OPh)_2)]$ and $[W((CO)_2PrN(PPh_2)_2]$, *J Organomet Chem*, 1990, **390**, 203–216.

7 MANOJLOVIĆ-MUIR, L., MUIR, K. W GROSSEL, M. C., BROWN, M. P NELSON, C. D., YAVARI, A., KALLAS, E., MOULDING, R. P. AND SEDDON, K. R — Tris-μ-(bis (diphenylphosphino) methane–diplatinum (O), *J. Chem. Soc. Dalton Trans.*, 1986, 1955–1963.

8 KUMARAVEL, S. S., KRISHNAMURTHY, S. S., CAMERON, T. S. AND LINDEN, A. — Synthesis and structural studies of new bicyclic 1, 3-diphenyl-1,3,2λ^5, 4λ^5-diazadiphosphetidines, *Inorg. Chem*, 1988, **27**, 4546–4550.

9 STRICKLEN, P. M., VOLCHO, E. J. AND VERKADE, J. G. — Novel homo- and heterometallic coordination macrocycles, *J Am Chem Soc*, 1983, **105**, 2494–2495.

Thesis Abstract (Ph.D.)

Electron spectroscopic investigations of nitrogen adsorbed on transition metal surfaces and of oxide superconductors by G. Ranga Rao.
Research supervisor: C. N. R. Rao.
Department: Solid State and Structural Chemistry Unit.

1. Introduction

Adsorption of N_2 on transition metal surfaces has been a subject of interest since many years[1,2]. For the last one decade, surface-sensitive techniques, *viz.*, x-ray photoelectron spectroscopy (XPS), ultraviolet photoelectron spectroscopy (UPS), electron energy-loss spectroscopy (EELS), etc., have been used extensively to identify different states of adsorbed molecules on metal surfaces[3]. Nitrogen is known to chemisorb molecularly as well as dissociatively on many of the transition metal surfaces. Two molecular states of N_2(ad) have been identified at temperatures below 170K using the above techniques. One of them is a weakly chemisorbed species with the molecular axis perpendicular to the metal surface (end-on orientation). Another molecular state is a strongly chemisorbed π-bonded precursor nitrogen with the molecular axis parallel to the surface (side-on orientation). This molecular precursor species dissociates at higher temperatures giving rise to an atomic nitrogen on metal surfaces.

The aim of this work is to investigate the adsorption behavior of N_2 and CO on clean and modified surfaces of transition metals. The chemisorption of N_2 on catalysts of the type Ni/Al_2O_3 and Ni/TiO_2 prepared *in situ* in the electron spectrometer has also been discussed. Transition metal oxides and superconductors have been studied by core-level spectroscopy to understand the nature of metal and oxygen states in these materials.

2. Experimental

The electron spectroscopic experiments were performed with VG ESCA 3 MARK II and VG ESCALAB V spectrometers. The radiations of He II (40·8 eV) for UPS and AlK_α (1486·6 eV) or MgK_α (1253·6 eV) for XPS were used in these studies. The XP and UP spectra were recorded at pass energies of 50 and 20 eV, respectively. EEL spectra were obtained using an electron beam of primary energy 3–5 eV. Substrate surfaces were cleaned by sputtering with argon ion beam followed by annealing. The exposures of pure N_2 gas were measured in Langmuirs (1L = 10^{-6} Torr.s).

3. Results and discussion

Adsorption of N_2 leads to the formation of a weakly chemisorbed molecular state on clean single-crystal Ni(100), (110) and (111) surfaces as well as on polycrystalline Ni and Pd surfaces at 80K. The interaction strength of N_2(ad) with the single-crystal Ni varies in the order of (100) > (110) > (111) faces. On polycrystalline Fe surface, however, a strongly bound molecular precursor coexists with a weakly chemisorbed N_2 at 80K. The weakly chemisorbed N_2 is stable up to 100K and desorbs leaving the molecular precursor above 100K. The weakly chemisorbed and precursor states show the N–N stretch frequencies at 2110 and 1590 cm^{-1}, respectively. The corresponding bond orders are estimated to be around 2·7 and 2, respectively.

Modification of polycrystalline Ni surface by electropositive element such as Ba or Al increases the bonding between metal and N_2(ad) because of the effective donation of metal electrons to the $1\pi_g$ antibonding orbital. This is manifested in the decrease of vibrational frequency from 2225 cm^{-1}, exhibited on clean Ni surface, to 1945 cm^{-1} on Ni surface modified by Al. A molecular precursor species prior to dissociation is formed at 80K on an Ni(110) surface covered with carbidic carbon or atomic nitrogen. At low C concentration, however, direct dissociative chemisorption occurs on Ni(110) surface at 80K, accompanied by weak molecular chemisorption on the open Ni sites.

In contrast to the effect of electropositive elements, chlorine is found to weaken the chemisorption bond between the metal and adsorbed CO or N_2. This leads to the stabilization of molecular species on Cl-precovered metal surfaces. As an example, Fig. 1 shows different adsorbed N_2 species present on clean, Ba- and Cl-modified Fe surfaces at 80K. On clean Fe surface, both end-on and side-on oriented N_2(ad) species are stable (step (i)), while on Ba-covered Fe surface only side-on precursor species is found (step (ii)). This precursor species dissociates into atomic nitrogen at higher temperatures. When Fe surface is covered with chlorine, we see only weakly bound end-on-oriented N_2 molecule without any precursor species (step (iii)). This species desorbs at higher temperatures.

Adsorption of N_2 on Ti and Ti–Ni alloy surfaces is found to be both molecular and dissociative. The molecular species shows only a single N(1s) feature around 405 eV indicating very weak chemisorption. Physisorbed N_2 is observed on TiO_2 surfaces with binding energy around 403·6 eV. Nitrogen adsorbs in the molecular form on Ni/Al, Ni/Al_2O_3 and non-annealed Ni/TiO_2 surfaces at 80K. On annealed Ni/TiO_2 surface, however, we find both dissociative and molecular adsorption at 80K (the latter desorbs at 125K) similar to the Ni–Ti alloy surface. This suggests that the annealed Ni/TiO_2 may represent the SMSI state of the catalyst.

Core-level studies indicate the presence of holes on oxygen (O^{-1} type species) in transition metal oxides. Metal ions such as Cu^{3+} and Ni^{3+} which are formally expected to be in 3+ oxidation state in these oxides appear to exist in the 2+ state because of the charge transfer from the oxide ion. Cu(2p) core-level studies

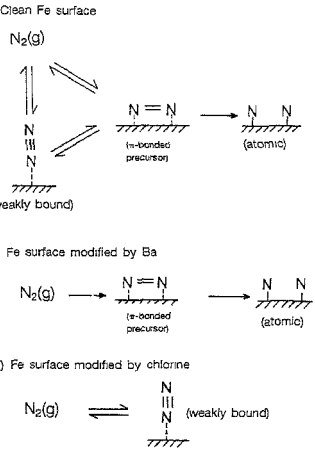

FIG. 1. Adsorbed nitrogen species on clean, Ba- and Cl-modified Fe surfaces at 80K.

demonstrate that Cu is present mainly in the 2+ state in Bi cuprates. The Cu–O charge-transfer-excitation energy which determines the Cu(2p) satellite intensity plays an important role in the superconductivity of cuprates. The relative intensity of the satellite generally decreases with an increase in the T_c or hole concentration in a given series of cuprate superconductors. In the case of $Bi_2Ca_{1-x}Ln_xSr_2Cu_2O_{8+\delta}$ (Ln = rare earth), the satellite intensity goes through a minimum around the same composition where the hole concentration as well as T_c show a maximum. The Bi(4f) spectrum of superconducting $BaBi_{0.25}Pb_{0.75}O_3$ shows a single feature with no evidence for charge separation on Bi ion.

References

1. HARDY, R. W F., BATTOMLEY, F. AND BURNS, R. C — *A treatise on dinitrogen fixation*, 1979, Wiley-Interscience
2. KOCK, A. J. H M. AND GEUS, J. M. — *Prog Surf. Sci.*, 1985, **20**, 165–272
3. ERTL, G AND KÜPPERS, J — *Low energy electrons and surface chemistry*, 1985, VCH

Thesis Abstract (Ph.D.)

Synthesis and reactions of oxygen and nitrogen heterocycles by S. K. Jayaram.
Research supervisor: T. R. Kasturi.
Department: Organic Chemsitry.

1. Introduction

Spirodienones, a class of compounds which occur widely in nature, are important from the point of view

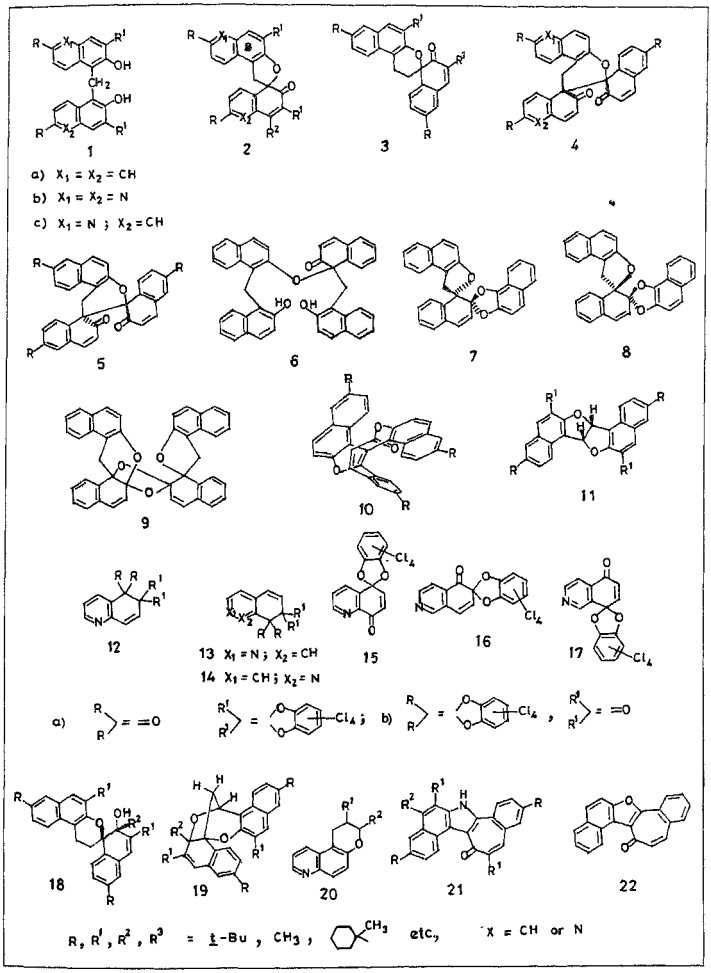
1
2
3
4
a) X1 = X2 = CH
b) X1 = X2 = N
c) X1 = N ; X2 = CH
5
6
7
8
9
10
11
12
13 X1 = N ; X2 = CH
14 X1 = CH ; X2 = N
15
16
17
a)
b)
18
19
20
21
22
R, R1, R2, R3 = t-Bu , CH3 , etc,
X = CH or N

of biosynthesis and have a fascinating chemistry[1]. Oxidative coupling of phenols is a convenient method for the synthesis of spirodienones. Kasturi *et al*[2] have isolated the *cis*- and *trans*-dispironaphthalenones (**4**) and (**5**) along with the Abel's ketone (**2**) and quinonemethide dimer (**3**) in the oxidation of bisnapthol (**1a**) with 2, 3-dichloro-5,6-dicyano-*p*-benzoquinone (DDQ). Spirodienones undergo a wide variety of bond-making and bond-breaking processes with various reagents under different reaction conditions to give novel rearranged, stable products[1-3]. In view of this, we have synthesised several spirocompounds and studied their fascinating chemistry.

2. Results and discussion

With a view to synthesising the nitrogen analogues of the above-mentioned spirodienones, oxidation of the nitrogen analogues of bisnaphthol (1b and 1c) with different oxidising agents like DDQ, KOBr and $K_3Fe(CN)_6$ was studied. This led to the formation of a number of heteroaromatic spirodienones (**2** and **4**). All these compounds were characterised on the basis of spectral properties. Isolation of the dispironaphthalenones in the $K_3Fe(CN_6)$ oxidation led to a reinvestigation of the oxidation of bisnaphthol with different oxidants which threw some light on the mechanism of formation of dispironaphthalenones and a new mechanism involving Barton-type[4,5] intermediate (**6**) has been proposed.

The DDQ oxidation of bis-naphthol gave in addition to the complex compounds mentioned above, a number of less polar compounds. A reinvestigation of this reaction on a fairly large scale was undertaken with a view to characterising these compounds. This led to the isolation of polyaromatic spirocompounds (**7**), (**8**), (**9**) and the macrocyclic lactone (**10**). The structures of these compounds were established by 2D-homo and hetero (^1H-^{13}C) correlation spectroscopy (FUCOUP) and the stereochemistry assigned by NOE studies. Further, it was found that the macrocyclic lactone (**10**) also resulted from the DDQ oxidation of dispironaphthalenones (**4**). Formation of all these compounds could be explained through the Barton-type intermediate (**6**).

Oxidation[6] of the quinonemethide dimers (**3**) with DDQ or *o*-chloranil resulted in the formation of the symmetric furofurans (**11**) the structure of which was confirmed by spectroscopic studies. The stereochemistry at the ring junction was confirmed to be *cis* (J = 8·04 Hz) by a study of the ^{13}C satellite peaks.

To have an insight into the mechanism of transformation of 2-naphthol to a mixture of α- and β-dienones during oxidation with *o*-chloranil[7], a few quinolinols and isoquinolinols were subjected to similar oxidations which resulted in the formation of spirodienones (**12–17**). Photomerisation of these spirodienones, involving β-C-O cleavage was also studied and this threw some light on the electronic factors involved in the novel rearrangement[8]. Grignard reaction of the quinonemethide dimers (**3**) led to spiroalcohols (**18**). The stereochemistry of these alcohols was confirmed to be trans by NOE experiments. Oxidation of these spiroalcohols with DDQ resulted in the novel dioxepin derivatives (**19**) the structure of which was confirmed by 2D-nmr experiments.

Several heteroaromatic chromans (**20**) have been synthesised[9] generating 5,6-quinolindione-5-methide by thermolysis of 5-dimethylaminomethyl-6-quinolinol and trapping it with different dienophiles.

The mechanism proposed by Dean *et al*[10] for the transformation of the spiroketone (**2**) to the indolotropone (**21**) upon treatment with $NH_2OH.HCl$, through the intermediacy of the tropone (**22**), was found to be wrong as the intermediate (**22**) did not give the indolotropone under similar reaction conditions. As a first step in the reinvestigation of the mechanism of this interesting transformation, the structure of the indolotropone was confirmed by x-ray crystal structure analysis. Several 3,3′ and 4′-substituted Abel's ketones were synthesised and subjected to the above transformation. From the results obtained, an alternative mechanism involving the transformation of the aromatic B ring of the spiroketone to the tropone ring has been proposed.

References

1 WARD, R. S. *Chem. Brit.*, 1973, **9**, 444–461.

2	KASTURI, T R., RAJASEKHAR, D., RAJU, G J., MADHUSUDHAN REDDY, G., SIVARAMAKRISHNAN, R., RAMASUBBU, N AND VENKATESAN, K	*J. Chem Soc Perkin Trans. I*, 1984 2375–2382
3	KASTURI, T R.	*Proc Indian Acad. Sci. Chem Sci.*, 1984, **93**, 531–545.
4	BARTON, D H R	*Chem. Brit*, 1967. **3**, 330–336.
5	HEWITT, D G	*J Chem Soc (C)*, 1971, 1750–1754.
6	KASTURI, T R. AND JAYARAM, S K	*Indian J Chem (B)*, 1988, **27**, 714–717
7	KASTURI, T R. ARUNACHALAM, T. AND SUBRAMANYAM, G	*J Chem Soc (C)*, 1970, 1257–1259.
8	KASTURI, T. R. AND JAYARAM, S K	*Indian J Chem (B)*, 1988, **27**, 605–608
9	JAYARAM, S K AND KASTURI, T. R	*Indian J. Chem (B)*, 1990, **29**, 707–710
10	DEAN, F M., LOCKSLEY, H. D. AND FLETCHER, C	*J. Chem Soc*, 1964, 5096–5098

Thesis Abstract (M.Sc. (Engng))

Bioleaching of a lean grade chalcopyrite ore—studies on amenability and mechanisms
by K. Suryanarayana Murthy.
Research supervisor: K. A. Natarajan.
Department: Metallurgy.

1. Introduction

The major problem being faced by today's mining industry is the continuous depletion of high-grade ores and the subsequent need to mine lean-grade ore deposits. Till now, these lean-grade ore deposits have been neglected because conventional pyrometallurgical techniques, which are energy consuming in nature, are not cost effective to process. Bioleaching which requires very little energy has emerged as an alternative methodology to the conventional technique in processing such lean-grade ores. Bioleaching has also additional advantages such as abating air pollution and suitability for the treatment of small tonnages. Microbial participation in the leaching of sulphides has been reported elsewhere[1,2]. Currently, this technique is being widely used in the extraction of copper and uranium on an industrial scale.

Malanjkhand copper project, the second largest ore-producing mine in India, mainly adopts conventional pyrometallurgical technique for metal extraction from high-grade ores in which the copper content is more than 0·5 per cent. It is estimated that in the next 12 years of operation, about 17 million tonnes of lean ore containing about 0·3 per cent of copper will be produced which cannot be processed economically by the above technique.

The current work has been undertaken with the following objectives:

(a) To optimise the various process parameters such as particle size, temperature and the necessity of external addition of $9K^{+}$ nutrients.

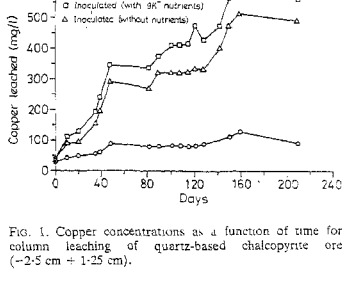

FIG. 1. Copper concentrations as a function of time for column leaching of quartz-based chalcopyrite ore (−2·5 cm + 1·25 cm).

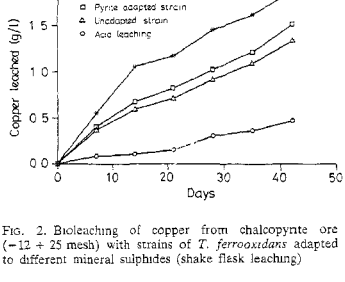

FIG. 2. Bioleaching of copper from chalcopyrite ore (−12 + 25 mesh) with strains of *T. ferrooxidans* adapted to different mineral sulphides (shake flask leaching)

(b) To investigate the significance of adapted strains in bioleaching, and

(c) To ascertain the relative significance of direct and indirect mechanisms occurring in a bioleaching process.

2. Experimental programme

The optimisation of various process parameters was studied with respect to column leaching. The lean-grade chalcopyrite ore sample used in the above experiments was procured from Malanjkhand. The ore as received was initially segregated into quartz- and granite-based samples and used separately in the experiments to find the influence of nature of gangue material on leaching. Mineralogical as well as chemical analysis carried out separately for each sample revealed about 0·4 per cent of copper in quartz-based sample while granite-based sample contained about 0·16 per cent of copper.

Shake flask studies were carried out for the above ore sample to find the significance of adapted strains in bioleaching. Two adapted strains, namely, chalcopyrite and pyrite were developed in the laboratory and their leaching efficiency was studied. Studies on the bacterial attachment to pyrite mineral were carried out to have a comprehensive understanding on the influence of various parameters such as particle size, agitation or static conditions on direct mechanism.

3. Results and conclusions

Copper dissolution from a quartz-based chalcopyrite ore sample as a function of time is depicted in Fig. 1. It could be seen from the figure that the metal dissolution was found to be higher in the presence of bacteria than in their absence. This could be attributed to the direct and indirect attack by bacteria on mineral sulphides. Higher leaching rates in the presence of bacteria were reported earlier[3]. It is also evident from the above figure that the beneficial effect of $9K^{+}$ on bioleaching was not of much significance. Similar results were observed with granite-based sample as well as other size fraction. However, the magnitude and the extent of copper dissolution was found to be dependent on the nature of ore sample and the size fraction. Smaller particles favoured faster and higher metal dissolution.

Figure 2 illustrates the significance of adapted strains in bioleaching. Copper dissolution was found to be higher in the presence of bacterial strain adapted to chalcopyrite mineral followed by that obtained with pyrite-adapted and unadapted strains, respectively. This is presumably due to the fact that the chalcopyrite mineral is expected to attack chalcopyrite mineral more efficiently compared to pyrite or unadapted strains.

The influence of various parameters on bacterial attachment to pyrite mineral under stationary conditions could be seen from Fig. 3. A minimum period of time lag was observed for the onset of significant bacterial attachment. This could be due to two factors: (a) Bacterial adaptation to the mineral sulphide, and (b) bacterial attachment to only a portion and not the entire mineral surface area. Considering the second case, the bacteria should have chemotacticity to locate such favourable sites[4,5]. The lag time was

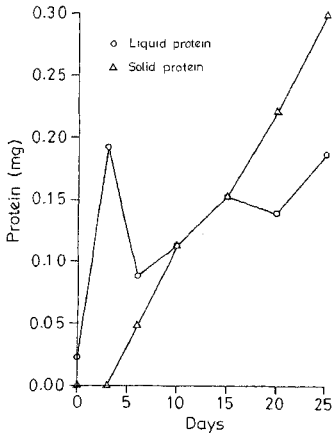

FIG 3. Estimated protein in the liquid and from the solids of pyrite mineral (−200 + 240 mesh) under stationary conditions.

found to increase with increasing particle size. Similar results were obtained with other size fractions also The results obtained under agitation conditions are analogous to those obtained under stationary conditions.

References

1. TORMA, A. E. Microbiological oxidation of synthetic Co, Ni and Zn sulphides by *Thiobacillus ferrooxidans*, *Rev Can Biol.*, 1971, **30**, 209–216
2. BRIERLY, J. A. Thermophilic iron-oxidising bacteria found in copper leaching dumps, *Appl. Environ Microbiol*, 1978, **36**, 523–525.
3. TORMA, A. E Oxidation of gallium sulphides by *Thiobacillus ferrooxidans*, *Can. J. Microbiol*, 1978, **24**, 888–891.
4. ALDER, J. Chemotaxis in bacteria, *A Rev. Biochem*, 1975, **44**, 341–356.
5. BERG, H. C. Chemotaxis in bacteria, *A. Rev. Biophys. Bioengng*, 1975, **4**, 119–136.

Thesis Abstract (Ph.D.)

Fluid rock interactions in the high-grade terrain of South India: A mineralogic and thermodynamic study by S. Varghese.
Research supervisors: G. V. Anantha Iyer, M. Subba Rao and A. G. Menon.
Department: Inorganic and Physical Chemsitry.

1. Introduction

In southern India, a gneiss-granite-greenstone terrain passes into a granulite-gneiss terrain to the south

Table I
Calculated values of $f(H_2O)P$, T and $X(H_2O)$ fl for the metapelitic assemblages of Karnataka and Tamil Nadu

Sl no	Locality	$\sigma\xi^2$	P kbar	$X(H_2O)^{cal}$	$f(H_2O)^{P,T}$ bar	$X(H_2O)^{fl}$
1	Dodderi	6·40	5·0	0·616	2561	0·665
2	Chikkakalavanchi	6·40	5·0	0·683	3438	0·900
3	W of Channanahalli	7·20	5·0	0·532	2619	0·545
4	W of Yelachikoppa	7·20	5·0	0·395	1503	0·275
5.	SW of Yelachikoppa	7·20	5·0	0·345	1211	0·215
6	N of Muddanpalya	7·20	5·0	0·475	2085	0·405
7	Neralamarada Doddi	7·20	5·0	0·335	1158	0·205
8	Jakkasandra	7·20	5·0	0·345	1211	0·215
9	Maralvadi	7·20	5·0	0·294	961	0·167
10.	Maralvadi	7·20	5·0	0·435	1773	0·333
11	Kallankuppa East	7·20	5·0	0·208	603	0·102
12	Kallankuppa East	7·20	5·0	0·221	653	0·111
13	Hallimarad Doddi	7·20	5·0	0·341	1194	0·212
14.	Tippasandra	7·20	5·0	0·502	2321	0·464
15.	Kodamballi	7·50	5·5	0·576	3897	0·728
16.	Duntur	7·50	5·5	0·502	2896	0·478
17	Duntur	7·50	5·5	0·512	3015	0·504
18	Attimur Hill	7·50	6·0	0·167	638	0·075
19	Sattanur Dam	7·50	6·0	0·325	1526	0·189

through a transitional zone spread over southern Karnataka and northern Tamil Nadu. The occurrence of charnockites as patches, blebs and cross-cutting veins showing transgressive contacts with amphibolite facies gneisses is a characteristic feature of the transitional zone and the predominantly high-grade Kerala Khondalite Belt (KKB) of southern most India. The accumulated field, mineralogic and fluid inclusion data indicate that the high-grade metamorphism was fluid-present in these different regions[1].

2. Cordierites as fugacity monitors

The channel volatiles in cordierites of high-grade metapelites from southern and eastern Karnataka, northern Tamil Nadu and southern Kerala were analyzed to characterize the variation in the fluid composition across metamorphic grade. Infrared (IR) powder absorption spectra of the cordierites, used to characterize the channel volatiles, indicate that all the cordierites have CO_2 and H_2O as channel volatiles, suggesting thereby that the metamorphic fluids were essentially of CO_2–H_2O composition. An overall correlation between the variation in the relative proportions of CO_2 and H_2O and the metamorphic grade is apparent from the IR data. The H_2O fraction in the metamorphic fluid, $X(H_2O)^{fl}$, was computed using a thermodynamic method for water barometry[2] in conjunction with gravimetrically determined channel water content and available pressure and temperature data for the pelites. The modified Redlich–Kwong equation of state of Kerrick and Jacobs[3] for H_2O and CO_2 was included in the calculation to take into account non-ideal mixing.

The IR and $X(H_2O)^{fl}$ data (Table II) obtained for the southern Karantaka–northern Tamil Nadu cordierites indicate a gross decrease in the proportion of H_2O in the fluid phase with a concomitant increase in the amount of CO_2 southwards in parallel with the overall increase in the metamorphic grade. It is concluded that charnockites and other granulites of these regions were formed in fluid-present environments and that large amounts of CO_2 in the fluids reduced the activity of water during the metamorphism. Some exceptional $X(H_2O)^{fl}$ values obtained may indicate local variation in the fluid composition or reequilibrium effects.

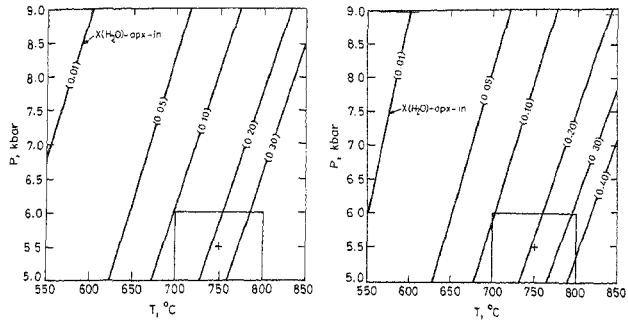

FIG. 1. P–T projections of $X(H_2O)$–orthopyroxene–in contours for (a) Kabbal- and (b) Ponmudi-type assemblages.

3. Fluids and tetrahedral Al, Si order/disorder of K-feldspars

To document mineralogically fluid–rock interactions, structural state of K-rich alkali feldspars in the gneisses, metapelites, charnockites and pegmatites of southern Karnataka–northern Tamil Nadu and the Kerala Khondalite Belt was characterised using petrographic and X-ray powder diffraction methods.

A gross correlation between the distribution of K-feldspar polymorphs and the metamorphic grade is apparent. The amphibolite facies gneisses and metapelites and incipient charnockites of southern Karnataka contain ordered triclinic feldspars with Al occupancy in the T_1O site, t_1O, in the range of 0·949–0·971 (Table II). The charnockites and metapelites of M.M. Hills host variable amounts of disordered K-feldspars, t_1O varying between 0·375 and 0·461. The K-feldspars in the pink granitic pegmatites of Closepet affinity are ordered. A quartz-feldspar pegmatic of probable metamorphic origin at Chillapura, southern Karnataka contains predominantly disordered K-feldspars. In the gneisses and charnockites of KKB the K-feldspars are predominantly disordered with t_1O varying between 0·334 and 0·461. Textural evidence for development of microclines proceeding from grain boundaries and fractures in disordered perthitic and mesoperthitic feldspars is seen in the high-grade rocks of all these terrains. Coarsening of mesoperthitic lamellae along peripheral zones of grains is seen in some KKB samples.

The variation in the structural state has been interpreted to reflect principally the interactions with fluids of varying aqueous contents and locally, deformation effects. In the southern Karnataka–northern Tamil Nadu regions, H_2O-deficient granulite facies metamorphism produced disordered K-feldspars while in the H_2O-dominant amphibolite facies metamorphism the K-feldspars formed were ordered. Similarly, the K-feldspars formed from hydrous melt of Closepet Granite are ordered. Some of the disordered K-feldspars in the granulites and metamorphic pegmatite underwent partial to complete conversion to microcline due either to interactions with the hydrous melt or granitizing fluids of Closepet granite activity, or locally due to deformation. The ordered K-feldspars in the incipient charanockites may reflect replacement of the original plagioclase due to interaction with hydrous metasomatizing fluids. Low H_2O activity during the regional high-grade metamorphism and subsequent gneiss-to-charnockite transformation produced the disordered K-feldspars in the gneisses and charnockites of the KKB. Later interaction with aqueous fluids resulted in the coarsening and ordering of disordered mesoperthitic feldspars.

Table II
Calculated Al-occupancy in the T_1O-site, t_1O, for southern Karnataka and KKB K-feldspars

Sl no	Southern Karnataka		Southern Kerala	
	Sample	t_1O*	Sample	t_1O
1	Kabbal	0·968(40)	Mannanthala	0·380(42)
2	Kabbal	0·971(23)	Panayamuttom	0·398(19)
3.	Ettnagudda	0·949(20)	Vadavathoor1	0·386(18)
4.	Chillapura	0·442(17)	Vadavathoor2	0·381(26)
5.	Chillapura	0·445(08)	Kottaram	0·334(31)
6.	Chillapura	0·437(08)	Aiyroopara	0·438(44)
7.	Halagur	0·436(06)	Kadakaman	0·343(28)
8.	Halagur	0·421(09)	Ponmudi	0·437(21)
9.	Sivasamudram	0·461(29)	Pappanamcode	0·461(25)
10.	Kollegal	0·375(11)		

Southern Karnataka samples. 1–Gneiss; 2,3–charnockite; 4–pegmatite; 5 to 9–charnockites, 10–metapelite. KKB samples: 1 to 4, 6–gneisses; 5, 7 to 9 charnockite.
*By using direct lattice parameters.
Standard deviation in parentheses represents the last two decimals

4. Numerical simulation of gneiss-charnockite transformations

With a view to articulating the role of individual fluid species in the gneiss to charnockite transformation, subsolidus mineral-fluid equilibria of two types of charnockite formation, namely, Kabbal- and Ponmudi-types[1] were computed using a free energy minimization method. The program SOLGASMIX[4] was used to arrive at the P–T–X_{fl} conditions of incipient charnockitization.

A low value of $X(H_2O)$ in the fluid phase is required to stabilize orthopyroxene in the two types of transformations. For the similar P and T of 5·5 kbar and 750°C, the computation indicated a value close to 0·25 for the Kabbal-type assemblage and 0·2 for the Ponmudi-type assemblage as the upper limit of $X(H_2O)$ in the fluid phase (Fig. 1).

Under conditions of incipient charnockitization, CO_2 and H_2O make up the bulk of the fluid phase. The other important fluid species, namely CO, CH_4, H_2 and O_2 are too small. The abundance of CO, CH_4, H_2 and O_2 is orders of magnitude higher in the graphite-bearing Ponmudi system, compared to the Kabbal system, but these four species do not total even to one per cent of the fluid phase.

Computation of phase equilibria in the Ponmudi–C–O–H–N system showed that the major fluid species are CO_2, H_2O and N_2. The abundance of other important species and the $X(H_2O)$ values required for the gneiss-to-charnockite conversion are comparable to those in the nitrogen-free system. The amount of equilibrium NH_3 is very low indicating the stability of N_2 under granulate conditions. Computation with varying amounts of N_2 showed that the $X(H_2O)$ required for incipient charnockitization is almost the same, indicating the very similar role of N_2 and CO_2 as diluents of H_2O.

References

1. Hansen, E. C., Janardhan, A. S., Newton, R. C., Prame, W. K. B. N. and Ravindra Kumar, G. R. — Arrested charnockite formation in southern India and Sri Lanka, *Contr. Mineral. Petrol.*, 1987, **96**, 225–244.

2. Bhattacharya, A. and Sen, S. K. — Energetics of hydration of cordierite and water barometry in cordierite-granulites, *Contr. Mineral. Petrol.*, 1985, **89**, 370–378.

3. Kerrick, D. M. and Jacobs, G. K. — A modified Redlich–Kwong equation for H_2O, CO_2 and H_2O–CO_2 mixtures at elevated pressures and temperatures, *Am. J. Sci.*, 1981, **281**, 735–767.

4. Eriksson, G. — Thermodynamic studies of high-temperature equilibria XII. SOLGASMIX, a computer program for calculation of equilibrium compositions in multiphase systems, *Chem. Scr.*, 1975, **8**, 100–103.

Thesis Abstract (Ph.D.)

Specificity and mechanism of action of RNase T_1—a computer modelling study by P. V. Balaji.
Research supervisor: V. S. R. Rao.
Department: Molecular Biophysics Unit.

1. Introduction

Ribonuclease T_1 (RNase T_1), an extracellular endonuclease secreted by the fungus *Aspergillus oryzae*[1,2], has been selected as the model system for the present work because of both its high specificity and small size (104 amino-acid residues). It specifically recognises the guanine bases in single-stranded ribonucleic acid and catalyses the hydrolysis of the phosphodiester bonds on the 3′-side of this base in a two-step reaction mechanism involving the intermediate formation of guanosine 2′, 3′-cyclic phosphate (G > p). The crystal structure of the enzyme complexed with its specific inhibitor guanosine 2′-mono phosphate (2′-GMP) has been determined at a high resolution of 1·9 Å by two groups of workers independently[3,4]. In addition, high-resolution structures of RNase T_1 complexed with guanyl 2′, 5′-guanosine[5] and guanosine-free RNase T_1 complexed with vanadate[6] are also known. The solution structure of RNase T_1[7] and its complexes with 2′-GMP and guanosine 3′-monophosphate (3′-GMP)[8] have been determined by 2D nmr spectroscopy combined with distance geometry and restrained molecular dynamics calculations. Apart from these studies, ^1H, ^{13}C and ^{15}N-nmr[9–12] and site-directed mutagenesis[13] studies have also been carried out. But these studies do not agree with each other in some of their conclusions like the puckering of the ribose moiety of the inhibitor when bound to RNase T_1 and the hydrogen-bonding scheme for the RNase T_1–2′-GMP complex. Further, these studies did not provide any conclusive evidence for the high specificity of RNase T_1 for guanine. Although His40, Glu58, Arg77 and His92 have been identified to be essential for enzyme activity by chemical modification and other physicochemical studies, no definite role for these amino-acid residues in catalysis has been assigned so far. Based on x-ray crystallographic[14], 2D nmr spectroscopic[8] and site-directed mutagenesis[15,16] studies, three different schemes for the mechanism of action of RNase T_1 have been proposed and they differ significantly in the nature of the amino-acid residues involved in catalysis.

2. Results and discussion

The calculated interaction energies of the three guanosine monophosphates have shown a decrease in the order 2′-GMP > 3′-GMP > 5′-GMP in agreement with experimental studies. The high pK_a value observed for Glu58 in the RNase T_1-2′-GMP complex has been shown to be due to possible hydrogen bond with phosphate group. It has also been shown that ribose moiety can assume either of the two puckered forms C2′-endo and C3′-endo in the complexes of 2′-GMP and 5′-GMP with RNase T_1 whereas in the RNase T_1-3′-GMP complex, it favours C3′-endo form. These results also explain the apparent discrepancies in the conclusions drawn from x-ray diffraction and spectroscopic studies on RNase T_1–2′-GMP complex.

Among the four nucleotides AMP, CMP, GMP and UMP, GMP has the highest and UMP the least interaction with RNase T_1 in agreement with the reported inhibitory power of these nucleotides. The present calculations also suggest that the nucleotides AMP, CMP and UMP can bind to RNase T_1 without any significant conformational changes in either the protein or the nucleotide leading to 'lock-and-key' model of binding. These studies also reveal the possible binding of AMP, CMP and UMP to the enzyme non-specifically in contrast to the binding of 3′-GMP.

The present calculations have also shown that molecules of the type pGp, ApG, CpG, UpG, ApGp, CpGp and UpGp can bind to RNase T_1 in essentially two modes: one energetically favourable mode and the other, a weak binding mode. A stereochemical explanation for the unexpected mode of binding of pGp to RNase T_1 has been given from the present study. The amino-acid residues possibly constituting the 1N and 1p sites were also identified and the hydrophobic and stacking interactions have been shown to play a key role in the binding of RNA to RNase T_1.

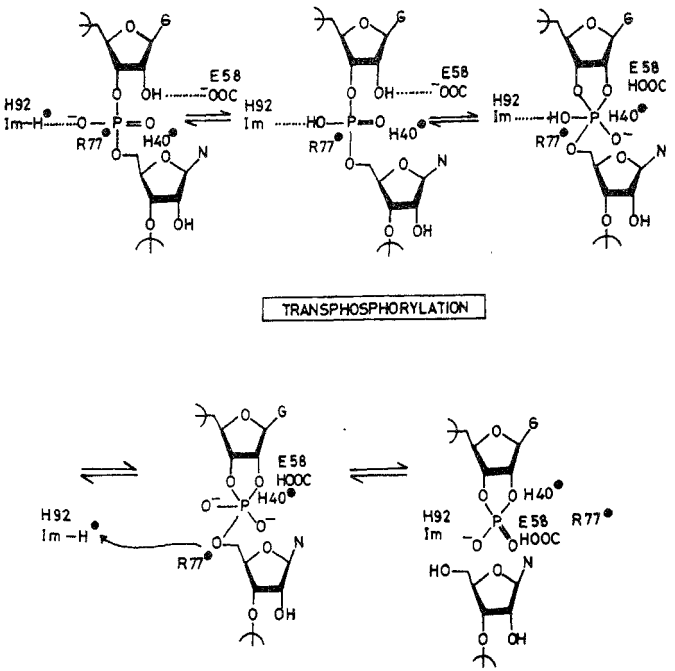

FIG. 1

Computer modelling studies on the binding of GpC and G > p to RNase T_1 have led to a proposal for the mechanism of action of RNase T_1 (Fig 1). In this scheme, the amino-acid residues Glu58 and His92 serve as the general base and acid groups for this enzyme catalysed hydrolysis reaction and His40 stabilises the transition state. After the hydrolysis reaction, the product molecules pGp or NpGp will be in their weak mode of binding which helps their release from the enzyme.

Thus the present computer modelling studies were undertaken to seek a plausible explanation for the specificity and the mechanism of action of RNase T_1. Using semiempirical potential energy functions, the three-dimensional structure of RNase T_1 complexed with various inhibitors (2'-GMP, 3'-GMP, 5'-GMP, AMP, CMP, UMP, ApG, CpG, and UpG), substrates (GpC, ApC and G > p) and products (pGp, ApGp, CpGp and UpGp) have been determined. Modes of binding of inhibitors/substrates to the enzyme, hydrogen bonding and other nonbonded interactions between the enzyme and the bound ligand have been elucidated from these calculations. The results have also been used for successfully explaining the experimental observations. These computer modelling studies have also provided valuable information about the

specificity, subsite interactions and the possible mechanism of action of RNase T_1. The studies on the complexes of RNase T_1 with the products have also led to a possible mechanism of release of the products subsequent to cleavage.

References

1 HEINEMANN, U. AND HAHN, U — In *Protein-nucleic acid interactions* (Saenger, W. and Hahn, U., eds). *Topics in molecular and structural biology*. Vol 10. pp 111–141. 1989, Macmillan

2 PACE, C. N., HEINEMANN, U., HAHN, U. AND SAENGER, W — *Angew. Chemie* (English edn), 1991, **30**, 343–360.

3 ARNI, R., HEINEMANN, U., TOKUOKA, R. AND SAENGER, W — *J. Biol. Chem.*, 1988, **263**, 15358–15368

4. SUGIO, S., AMISAKI, T., OHISHI, H. AND TOMITA, K. — *J. Biochem.* (Tokyo), 1988, **103**, 354–366.

5 KOEPKE, J., MASLOWSKA, M., HEINEMANN, U. AND SAENGER, W — *J. Mol. Biol.*, 1989, **206**, 475–488

6 KOSTREWA, D., CHOE, H.-W., HEINEMANN, U. AND SAENGER, W — *Biochemistry*, 1989, **28**, 7592–7600.

7 HOFFMAN, E. AND RUETERJANS, H. — *Eur. J. Biochem.*, 1988, **177**, 539–560.

8 HOFFMAN, E., SCHMIDT, J., SIMON, J. AND RUETERJANS, H — *Nucleosides Nucleotides*, 1988, **7**, 757–761

9 RUETERJANS, H. AND PONGS, O — *Eur. J. Biochem.*, 1971, **18**, 313–318

10. ARATA, Y., KIMURA, S., MATSUO, H. AND NARITA, K — *Biochemistry*, 1979, **18**, 18–24

11. INAGAKI, F., KAWANO, Y., SHIMADA, I., TAKAHASHI, K. AND MIYAZAWA, T. — *J. Biochem.* (Tokyo), 1981, **89**, 1185–1195.

12 INAGAKI, F., SHIMADA, I., AND MIYAZAWA, T — *Biochemistry*, 1985, **24**, 1013–1020.

13. HAKOSHIMA, T., TODA, S., SUGIO, S., TOMITA, K.-I., NISHIKAWA, S., MORIOKA, H., FUCHIMURA, K., KIMURA, T., UESUGI, S., OHTSUKA, E. AND IKEHARA, M. — *Protein Engng*, 1988, **2**, 55–61.

14. HEINEMANN, U. AND SAENGER, W. — *Pure Appl. Chem.*, 1985, **57**, 417–422.

15. NISHIKAWA, S., MORIOKA, H., KIM, H., FUCHIMURA, K., TANAKA, T., UESUGI, S., HAKOSHIMA, T., TOMITA, K., OHTSUKA, E. AND IKEHARA, M — *Biochemistry*, 1987, **26**, 8620–8624.

16 STEYAERT, J., HALLENGA, K., WYNS, L. AND STANSSENS, P. — *Biochemistry*, 1990, **29**, 9064–9072.

Thesis Abstract (Ph.D.)

Grain boundary layer ceramic capacitors from substituted $BaTiO_3$ processed from hydrothermal powders by R. Vivekanandan.
Research supervisor: T. R. N. Kutty.
Department: Materials Research Centre.

1. Introduction

The current emphasis on the ceramic dielectric materials in the electronic components aims at storing

Table I
Perovskites prepared by hydrothermal method[3-6]

Product	*Reactants*	*Lowest reaction temp °C*	*Structure*	*Cell constants Å*
$BaTiO_3$	$Ba(OH)_2+TiO_2.xH_2O$	85	Cubic	a = 4·064
$SrTiO_3$	$Sr(OH)_2+TiO_2\ xH_2O$	120	Cubic	a = 3·905
$CaTiO_3$	$CaO+TiO_2.xH_2O$	150	Monoclinic	a = c = 7·638 b = 7·637 β = 90·40
$BaZrO_3$	$Ba(OH)_2+ZrO_2\ xH_2O$	130	Cubic	a = 4·196
$BaSnO_3$	$Ba(OH)_2+SnO_2.xH_2O$	260	Cubic	a = 4·116

maximum electrical energy in a minimum volume, minimum temperature coefficient, low loss and widest range of frequency stability. This can be achieved by adopting grain-boundary layer or multilayer ceramic capacitor processing techniques. In multilayer capacitors, the high-permittivity dielectric is processed into thin sheets of 20–50 μm thickness and stacked into thin-plate geometry where each layer is separated by thin-film electrode. In grain-boundary-layer capacitors, the ceramic is processed in such a way as to get conducting grain interiors and insulating grain boundary layers. Effectively the grain boundaries act as microcapacitors interconnected by the conducting grain cores[1]. $BaTiO_3$ and its solid solutions in a number of modified or doped forms are used for these capacitors. To get high ϵ_1, the ceramic should have high sinter density and controlled grain size, which requires starting materials of submicron particle size. In the present case, fine powders are produced from the hydrothermal method. Hydrothermal is a geological term pertaining to the natural processes characterized by the joint action of heat and water under pressure[2].

2. Experimental procedure

Reactive gels of $TiO_2/SnO_2/ZrO_2.xH_2O$ of varying Ti/Sn/Zr ratios are precipitated by the addition of NH_4OH to $TiOCl_2/SnCl_4/ZrOCl_2$ aqueous solutions. The gels are washed free of chloride and NH_4 ions and are mixed with $Ba(OH)_2$ or $Sr(OH)_2$ or CaO. The molar ratios of A/Ti+Zr+Sn (A = Ba, Sr, Ca) is maintained at 0·98–1·05. The slurry is charged into Morey-type autoclave lined with teflon. The relative fill in the autoclave is maintained at 60–80 per cent with distilled water. The autoclave is heated to 120–275° C for 2–6 h. After cooling the pressure vessel, the solid products obtained are filtered. Donor (Nd^{3+} or Sb^{5+}) and acceptor (Mn^{2+}, Cu^{2+}, Zn^{2+}) doping is carried out in the hydrothermal preparation by coprecipitating the corresponding hydroxides with the gel. The powders thus obtained are pressed into pellets and sintered at 1320–1380°C for 2–10h. Ohmic contact is provided for these ceramics by electroless nickel plating. The methods adopted for characterization include XRD, AAS, TGA/DTA, IR, EPR, TEM, SEM capacitance and resistance techniques.

3. Results and discussion

Table I gives the reaction temperature, crystal system and the unit cell constants for the perovskites produced by the hydrothermal method[3-6]. As-prepared $BaTiO_3$ is cubic (metastable) at room temperature, which converts to tetragonal phase after heat treatment above 1200°C[3]. During the synthesis of $BaSnO_3$, an intermediate phase, $BaSn(OH)_6.3H_2O$ is formed under hydrothermal conditions which decomposes in air at 280°C to give $BaSnO_3$[5]. Solid solutions of $Ba(Ti,Zr)O_3$, $Ba(Ti,Sn)O_3$, $(Sr,Ba)TiO_3$ are also prepared by the hydrothermal method. Solid solutions of $Ba(Ti,Sn)O_3$ form up to 35 atom % Sn, under hydrothermal conditions. At higher Sn contents, the product is a mixture of cubic $BaTiO_3$ and $BaSn(OH)_6,3H_2O$. Heat treatment of these mixed phases at 260°C gives separate phases of $BaTiO_3$ and $BaSnO_3$, which on heating to 1000°C, gives rise to monophasic $Ba(Ti,Sn)O_3$[5].

Fine powders of TiO_2 (rutile) are formed from aqueous titanium oxychloride solution under hydrothermal conditions at 160–230°C within 2h. The anatase phase is produced from the same medium when sulfate ion impurity is present, with $[SO_4]/[Cl] > 0{\cdot}03$. Similarly, ultrafine ZrO_2 (monoclinic) is hydrothermally precipitated from aqueous zirconyl oxychloride at 180–230°C within 2h. Tetragonal ZrO_2 is produced from the same medium when sulfate ions are present with $[SO_4]/[Cl] > 0{\cdot}08$. Both TiO_2 and ZrO_2 convert to ABO_3 perovskites when suspended in the corresponding hydroxide solution at 190–480°C under hydrothermal conditions.

A detailed evaluation of size, shape and microstrains of the doped and undoped $BaTiO_3$ crystallites are carried out using X-ray line-broadening[7,8] and TEM studies[9]. It is found that the concentration of $Ba(OH)_2$, and acceptor impurities affect the crystallite shape, whereas the stoichiometry with respect to Ba/Ti, donor as well as acceptor impurities, influence the microstrains. It is shown that the strains in the submicron crystallites are related to the point defects in the lattice. Heat treatment reduces anisotropy and strain in undoped samples, whereas annealing is less effective in doped materials.

Grain-boundary-layer ceramic capacitors are processed from $Ba(Ti_{1-x}Sn_x)O_3$ solid solutions ($0 < x < 0{\cdot}25$), doped simultaneously with donor and acceptor impurities[10]. Dielectric properties of these ceramics are strongly dependent on the concentration of donors as well as acceptor dopants, the ceramic microstructure and the phase contents. It is also found that the $3d^n$ configuration of acceptor impurities also influences the dielectric properties. Energy-dispersive X-ray analysis shows uniform distribution of donor and acceptor impurities along the grain and grain boundaries. Phase content analysis by EPR reveals partial coexistence of ferroelectric orthorhombic and tetragonal phases along with the paraelectric cubic phase which directly converts to the rhombohedral phase at low temperatures. The insulating behavior of the grain boundary layers, as compared to the grain interiors, is explained on the basis of higher concentration of barium vacancies in these layers and the vibronic activation of the acceptor states in various symmetry configurations of a lattice that undergoes diffuse phase transition.

The resistivity anomaly and the charge redistribution around the phase transition temperature at the acceptor states in $BaTiO_3$ is explained on the basis of vibronic interaction mechanisms. The resistance anomaly due to structural phase transition in $BaTiO_3$:0·3Nd+0·02Mn is calculated using the TO soft mode frequency. The calculated resistivity values are modified by considering the contribution from multiphonon interaction processes and from mixed contributions from the lower symmetry phases which transform to cubic phase above T_c. The calculated values are compared with experimental observations. Validity of the present explanation for the resistance anomaly during the phase transition is discussed, in comparison with the existing PTCR models.

References

1. GLAISTER, R. M. — Barrier-layer dielectrics, *Proc. Instn Electl Engr*, 1961, **109** (Suppl. 22), 423-430.
2. FRANCK, E. U. — Supercritical water, *Endeavour*, 1968, **27**, 55-59.
3. VIVEKANANDAN, R , PHILIP, S. AND KUTTY, T. R. N — Hydrothermal preparation of $Ba(Ti,Zo)O_3$ fine powders, *Mater. Res. Bull.*, 1987, **22**, 99-107
4. KUTTY, T. R. N. AND VIVEKANANDAN, R. — Preparation of $CaTiO_3$ fine powders by the hydrothermal method, *Mater. Lett.*, 1987, **5**, 79-83.
5. KUTTY, T R. N. AND VIVEKANANDAN, R. — $BaSnO_3$ fine powders from hydrothermal preparations, *Mater. Res. Bull.*, 1987, **22**, 1457-1465.
6. KUTTY, T. R. N., VIVEKANANDAN, R.AND MURUGARAJ, P. — Precipitation of rutile and anatase (TiO_2) fine powders and their conversion to $MTiO_3$(M = Ba, Sr, Ca) by the hydrothermal method, *Mater. Chem Phys.*, 1988, **19**, 533-545.
7. WILLIAMSON, G. K AND HALL, W. H. — X-ray line broadening from filed Al and W, *Acta Metall.*, 1953, **1**, 22-31.
8. WARREN, B. E. AND AVERBACH, B. L. — The separation of stacking fault broadening in cold-worked metals, *J. Appl Phys.*, 1952, **23**, 1059.
9. VIVEKANANDAN, R. AND KUTTY, T. R. N. — Characterization of barium titanate fine powders formed from hydrothermal crystallization, *Powder Technol* , 1989, **57**, 181-192.
10. VIVEKANANDAN, R. AND KUTTY, T. R. N — Grain boundary layer ceramic capacitors based on donor-doped $Ba(Ti_{1-x}Sn_x)O_3$, *Mater. Sci. Engng*, 1990, **6**, 221-231

Thesis Abstract (Ph.D.)

Impedance of sealed nickel–cadmium cells at low states of charge by M. S. Suresh. Research supervisors: S. Sathyanarayana (IPC), N. Kumar (Physics) and A. Subramanyam (ISAC).
Department: Physics.

1. Introduction

Nickel–cadmium cells are rechargeable power sources having a wide range of applications. Hermetically sealed, sintered plate nickel–cadmium cells have been used in aerospace applications to power satellites as these cells are reliable and have a long life. The cells, however, degrade in performance with use due to physicochemical changes that occur within the cells.

Impedance of electrochemical cells yields information on the physicochemical processes occurring in the cells. When performed over a range of frequencies, measurement of impedance can give information about kinetics of charge transfer, diffusion of active species and double-layer capacitance. Hence, technique of frequency response analysis is, in principle, well suited for understanding degradation processes in sealed nickel–cadmium cells.

Frequency-response analysis has been applied by several workers in an attempt to understand degradation mechanisms in sealed nickel–cadmium cells[1–10]. Most of them have studied impedance of cells at relatively high (>5 per cent) states of charge[1,2,5–10]. A few studies have been made at zero-cell EMF[3,4] which corresponds to zero state of charge. However, systematic study of the processes occurring within the cells has not been made, especially in the range of 0·0–1·2 V cell EMF.

In sealed nickel–cadmium cells, with excess negative electrode capacity, the potential of the nickel oxide electrode varies from about 1·2–0·0V (*vs* $Cd/Cd(OH)_2$) in the 'knee' region for negligible change in its state of charge. Thus, one may expect to find a wealth of information about the physicochemical processes taking place at the nickel oxide electrode in the cell EMF range 0·0–1·2 V. Hence, an investigation of the impedance of sealed nickel–cadmium cells in this EMF region was undertaken.

2. Experimental aspects

The impedance of sealed nickel–cadmium cells was measured by applying a sine wave signal of 1 mV (rms) and measuring the inphase and quadrature components of current. The impedance was calculated from the ratio of the applied voltage to the current response expressed as a series-equivalent circuit (R_S, X_S). Impedance of cells was measured in the frequency range 1–0·01 Hz in the cell EMF interval 0·0–1·3 V in steps of 0·1 V. Impedances were also measured at five temperatures −10, 0, +10, +20 and +30°C covering the normal operating temperature range of nickel–cadmium cells.

To check some of the hypotheses considered to explain the impedance behavior of cells several experiments were performed on cell electrodes such as effect of adsorption of products of hydrolysis of the nylon separator and the effect of carbonates on the impedance of cells.

3. Results and discussion

The results showed that the impedance of nickel–cadmium cells (R_S, X_S) peaks around a cell EMF of 0·3–0·45V. The cell impedances were analysed by plotting them as a function of cell EMF and in the complex plane. Based on the results of experiments on cell electrodes, it was concluded that the peaking of impedance of cells was due to processes occurring at the nickel oxide electrode.

Based on the above results it has been deduced that the impedance of sealed nickel–cadmium cells is governed by three different processes.

1. Ni(II)/Ni(III) electrode reaction, above a cell EMF of about 1·1V.
2. A double-layer charging region between 1·0 and 0·2V of cell EMF
3. A new (hitherto unsuspected) Faradaic process between 0·0 and 0·2 V of cell EMF.

A detailed analysis of the results has led to the identification of the most probable reaction in the cell EMF region 0·0–0·2 V as hydrogen electrode reaction (HER).

Based on the phenomenological theory developed to explain the observed behavior, equivalent circuits were developed that fit the experimental results. The values chosen for the equivalent circuit are in reasonable agreement with the values derived from theoretical considerations.

4. Conclusions

The following general conclusions could be drawn from this work.

1. Three different phenomena at different cell EMF; Ni(II)/Ni(III) reaction, double layer, and HER are responsible for the impedance of sealed nickel–cadmium cells at low states of charge. This explains the occurrence of impedance peaks.

2. Porous nickel oxide electrode can be modelled as a planar electrode at low states of charge after taking into account the increased area due to porosity.

3. The variation of charge transfer resistance with temperature for the reaction occurring at 0·0V cell EMF does not follow a simple Arrhenius relation.

4. The measured variation of the dopuble-layer capacitance of the nickel oxide electrode with cell EMF concurs with such measurements made earlier.

The conclusions drawn from this work may have far-reaching consequences in nondestructive testing of sealed nickel–cadmium cells, since it is now possible to identify clearly the regions of cell EMF which correspond to different (for example, Faradaic or non-Faradaic) phenomenological domains of the nickel oxide electrode.

References

1 Hampson, N. A., Karunathilaka, S. A. G. R. and Leek, R. — *J. Appl Electrochem.*, 1980, **10**, 3–11

2 Sathyanarayana, S., Venugopalan, S. and Gopikanth, M. L. — *J Appl. Electrochem.*, 1979, **9**, 125–139.

3 Sal Di Stefano — *Studies of the life limiting failure mechanisms of sealed nickel–cadmium cells*, Final report JPL-D-991, Jet Propulsion Laboratory, California, USA, 1983.

4 Haak, R., Ogden, C., Tench, D. and Sal Di Stenfano — *J. Power Sources*, 1984, **12**, 289–303.

5. Zimmerman, A. H and Janecki, M. C. — *Impedance and mass transport kinetics of nickel–cadmium cells*, Report No. SD-TR-81-63, Sept. 1981, The Aerospace Corporation, El Segundo, California 9024, USA.

6 Zimmerman, A. H., Martinelli, M. R., Janecki, M. C and Badcock, G C. — *J Electrochem. Soc* , 1982, **129**, 289–293.

7. Zimmerman, A. H. — *Impedance of aerospace Ni–Cd cells under open circuit conditions*, Report No. SD-TR-81-109, Jan 1982, The Aerospace Corporation, El Segundo, Calfornia 9024, USA.

8. Zimmerman, A. H. and Effa, P. K. — *Short circuit formation during Ni–Cd cell reversal*, Report No. SD-TR-82-26, May 1982, The Aerospace Corporation, El Segundo, California 9024, USA.

9. Lenhart, S. J., Macdonald, D D. and Pound, B G. — *Space electrochemical research and technology*, NASA Conf. Pub. 2484, April 14–16, 1987, pp 257–283

10. Jindra, J., Musilova, M., Mrha, J and Novak, P. — *Bull. Electrochem.*, 1988, **4**, 137–140

Thesis Abstract (Ph.D.)

Digital computation of magnitudes and waveshapes of voltages and currents on transmission system components due to lightning strokes by N. K. Kishore.
Research supervisor: G. R. Nagabhushana.
Department: High Voltage Engineering.

1. Introduction

Lightning has proved to be the single largest cause of outages on EHV systems contributing to nearly 50% of them. Thus, there is a great need to assess lightning performance of transmission systems. Such a study requires a knowledge of magnitudes and waveshapes of voltages and currents due to lightning strokes. But there is no reliable analytical method to assess these parameters. This work aims at improving the equivalent circuit representation of the lightning stroke to assess the magnitudes and waveshapes of lightning voltages and currents.

2. Equivalent circuit representation

The thundercloud is represented as a capacitor charged to cloud potential. The lightning stroke channel is represented realistically as a lossy transmission line, for the first time, the lossy nature is considered by lumping R_s as $R_s/4$ at the begining and at the end of the line and $R_s/2$ at the middle. R_s itself is estimated based

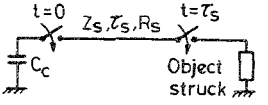

C_c : Cloud capacitance
R_s : Arc resistance.
Z_s : Stroke channel surge impedance
τ_s : Travel time along stroke.

FIG. 1. Equivalent circuit for the lightning stroke

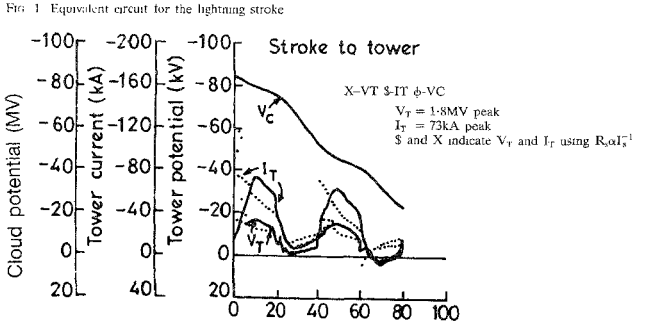

FIG. 2. Results for stroke to tower with OHGW for V_c = 100MV and C_c = 0·2 μF

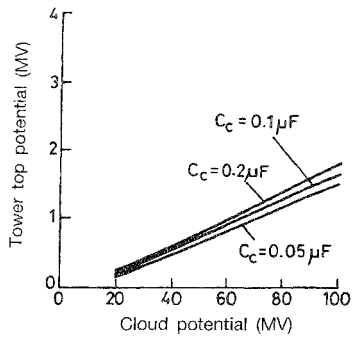

FIG. 3 Variation of tower top potential V_T as a function of cloud potential V_C for strokes to tower with OHGW

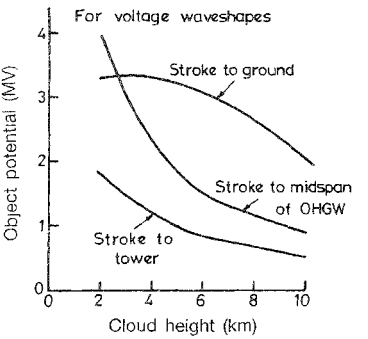

FIG. 4 Variation of tower current I_T as a function of cloud potential V_C for strokes to tower with OHGW

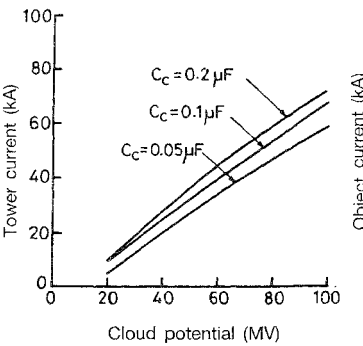

FIG. 5 Variation of voltage as a function of cloud height for V_c = 100 MV and C_c = 0·2μF.

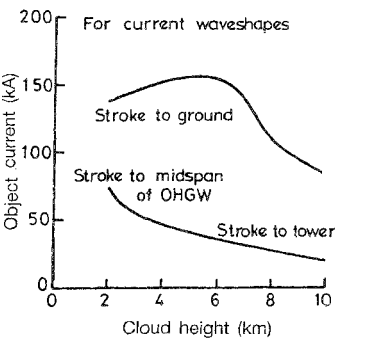

FIG. 6. Variation of current as function of cloud height for V_c = 100 MV and C_c = 0·2μF

on experimental studies on impulse current (8×20μs, 5–20kA) arcs(15 cm long). The results of the experiment could be expressed as:

$$R_r = A+B.Exp(-t/\tau) \quad (1)$$

where R_r is the resistance of the stroke channel at any instant in Ω/m.

$$A = 0{\cdot}3+2{\cdot}84{\cdot}Exp(-Ip/8) \quad (2)$$

$$B = 4{\cdot}0+28{\cdot}0{\cdot}Exp(-Ip/8.2) \quad (3)$$

$$\tau = 3{\cdot}0+6{\cdot}0{\cdot}Exp(-Ip/7{\cdot}5) \quad (4)$$

t = time in μs & Ip = Crest stroke current in kA.

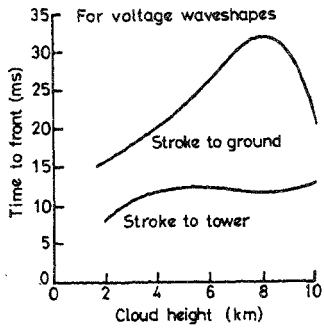

FIG. 7. Variation of times to front for voltage as a function of cloud height for V_c = 100 MV and C_c = 0·2μF.

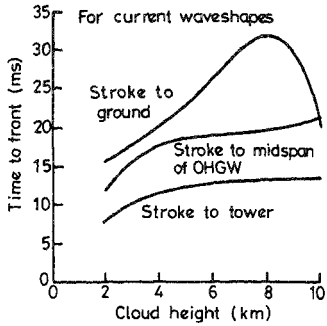

FIG. 8. Variation of times to front for current as a function of cloud height for V_c = 100 MV and C_c = 0·2μF.

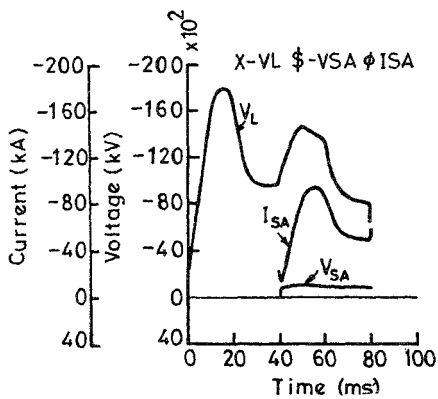

	Peak	18·2MV
V_L	t_f	15μs
	peak	96kA
I_{SA}	t_f	15μs
V_{SA}	peak	1·02MV

FIG. 9. Results for distant stroke to phase conductor terminated in an SA for V_c = 100 MV and C_c = 0·2μF.

The target objects of relevance are: a) towers with/without overhead ground wires(OHGW), b) OHGW, and c) phase conductors terminated with a transformer-surge arrester combination or a surge arrester. The tower is represented by a short transmission line of constant surge impedance terminated in a lumped resistance equal to tower footing resistance (TFR). TFR itself is represented as a time-dependent resistance based on Bewley's curve[1] expressed as:

$$R_f = 116.\ \mathrm{Exp}(-t/1{\cdot}425) + \mathrm{Rl} \qquad (5)$$

where R_f is TFR at any instant t in Ω and t is time in μs.

OHGW and phase conductors are represented by their surge impedance and transmission line behaviour. A gapless ZnO surge arrester (SA) is modelled as a three-slope nonlinear resistor based on v–i characteristics from the manufacturer's data sheets. Each region is represented by $v = ki^{\beta}$. Here, v is the arrester voltage in kV, i the arrester current in A, and k and β are constants derived from manufacturer's data sheets.

A transformer on on-load is represented by its stray capacitance, and when on load, by an inductance equal to the leakage reactance in parallel with stray capacitance.

With the above representations, computations have been made for strokes to a) towers with/without OHGQ, b) midspan of OHGW, c) ground, and d) phase conductors terminated in SA/SA-transformer combination. Dommel's method has been adopted for the computations. Figure 1 shows the equivalent circuit for the lightning stroke.

3. Results and conclusions

Figure 2 shows results for stroke to tower with OHGW for V_c = 100MV and C_c = 0·2μF. Time to front for tower top potential V_T is about 1μs reaching a peak value of 1·8MV, with a second peak of similar magnitude at about 8μs. Time to tail is about 30μs. Tower current reaches a peak value of 72kA in 8μs. Figures 3 and 4 show the dependence of V_T and I_T as a function of cloud potential V_c, with cloud capacitance C_c as a parameter. It can be seen that V_T and I_T are nearly linear with Vc. The values of VT are in the range of 0·15 to 1·8MV and those of I_T are in the range of 6 to 72kA. These magnitudes are in reasonable agreement with the available field data[3,4], lending credibility to the proposed equivalent circuit. Times to front for current are in a close range of 8 to 10 μs whereas earlier works mention front times in the range 2 to 18μs. Figures 5–8 show the dependence of magnitudes of voltages, currents and times to front on cloud height (*i.e.*, stroke channel length) It is seen that magnitudes reduce with increase in cloud height. This is due to higher drop in the increased resistance of the stroke channel due to increase with increase in cloud height except in the case of strokes to ground. This is also attributable to the increased stroke-channel resistance (length).

Figure 9 shows typical results for a stroke-to-phase conductor. Distant strokes-to-phase conductors indicate arrester currents in the range 6 to 96kA with front times in the range of 20 to 11μs. On the other hand, closeby strokes indicate arrester currents in the range 8 to 130kA with front times in the range 20 to 11μs. Thus the computed waveshapes and magnitudes are significantly different from those specified in the standards. There is little field data to compare meaningfully; therefore, it would be interesting to obtain the field data and perhaps a relook at the standards. Arrester potentials are substantially rectangular falling by less than 10 per cent in 50 μs. Therefore, it would be interesting to obtain the field data on the behaviour of transformer insulation to such rectangular pulses rather than the present standard 1·2/50μs.

It is also observed that the magnitudes and waveshapes of voltages and currents are very much dependent on the surge behaviour of the object struck. The transient behaviour of towers, OHGW and phase conductors is well understood. However, transient behaviour of ground is not as well known and needs to be investigated.

In conclusion, this work has been successful in improving the equivalent circuit for the lightning stroke to estimate the magnitudes and waveshapes of voltages and currents due to lightning strokes. Several possible areas of interest for future investigation also have been highlighted.

References

1. BEWLEY, L. V. — Theory and tests of counterpoises, *Electl Engng*, 1934, **53**, 1163–1172.
2. DOMMEL, H. W. — Digital computer solution of electromagnetic transients in single and multiphase networks, *IEEE Trans.*, 1969, **PAS-88**, 388–396.
3. ANDERSON, R. B. — Lightning and thunderstorm parameters, *Proc. IEE Int. Conf. on Lightning and Power Systems*, London, 1984, pp 57–61.
4. GROSS, I. W. AND COX, J. H. — Lightning investigation on the Appalachian Electric Power Company's transmission systems, *Trans. AIEE*, Pt III, 1931, **PAS-50**, 1118–1131.

Thesis Abstract (M.Sc. (Engng))

Transform techniques for optical waveguides by Shiva Kumar.
Research supervisor: A. Selvarajan
Department: Electrical Communication Engineering.

1. Introduction

Practical applications of integrated optics require understanding of light propagation in dielectric waveguides of various geometries and calls for elegant and quick methods of analysis. Beam propagation method (BPM) is one of the methods of analysis[1,2]. It is an accurate method for the medium with small variations in refractive index profile. The method consists of propagating the input beam over a small distance along the propagation direction in a homogeneous medium and then correcting for the refractive index variations seen by this beam during the propagation step. The aim of the work is to analyse a few practical integrated optic structures such as bent waveguide, coupled waveguide and branching waveguide using beam propagation method and a new transform technique.

2. Results and discussion

In BPM, one has to solve scalar Helmholtz equation for homogeneous medium iteratively and apply correction factor. To achieve this, usually FFT algorithms are adopted. But, if we combine Simpson's 1/3 rule with FFT to solve Helmholtz equation for homogeneous medium. The speed of FFT and accuracy of Simpson's 1/3 rule are simultaneously achieved. This algorithm is applied to study practical integrated optic structures such as bent waveguide, branching waveguide, coupled waveguide and X-switch. For bent waveguide, the power output is calculated for different angles of bend. It is found from the study that, beyond the bend angle 10°, almost all the power will be radiated into the substrate

Next the algorithm is applied to branching waveguide with shallow taper. It is found to act like a mode-splitter, *i.e.*, the TEO1 mode launched into the input arm of the waveguide is found to be transferred completely into one of the arms at the output. Next the tappers are made steep by increasing the bent angle to 1/50 radians. Now the waveguide acts like a power splitter. *i.e.*, the power is splitting into both the arms. With the structure considered, the ratio of power in the output arms is found to be 36·64.

Next, the method is applied to directional coupler and planar waveguide array. The results are found to be in good agreement with analytical results. The method is extended to cylindrical coordinates so that two-dimensional Fourier transform can be replaced by one-dimensional Hankel transform for the structures with cylindrical symmetry such as optical fibres.

The conventional beam propagation algorithm is modified using convolution theorem so that only one convolution integral has to be done for every iteration instead of two integrations. In conventional BPM, one has to: (1) take Fourier transform of input beam, (2) propagate it for some distance, (3) take the inverse transform, and (4) multiply by correction factor. The convolution integral suggested does all the above four operations with the help of a single integral and hence will reduce a lot of computational time and errors. In addition, transforming from spatial to spectral domain is done only once at the starting and hence sufficiently more number of samples in spatial domain can be taken to get better accuracy. If the same number of samples are taken in usual BPM, it will take a lot of computational time since transforming and inverting would be done at every iteration. The suggested algorithm is applied to the combination of micro lens and tapper. The results are compared with the conventional BPM.

Finally, a new transform technique for optical waveguides is suggested. The limitations of BPM are that computations can be carried out over limited propagation distance and also variations in the refractive index profile must be small. In the new transform technique proposed, such approximations are not made. The method is based on convolution and Laplace transform techniques. The method converts the partial differential equation into a set of algebraic equations in the transformed domain which can be solved on

the computer by matrix inversion. For a homogeneous medium with index n_s, the field can be expressed as the superposition of plane waves in all directions with the propagation constant, $k_0 n_s$, where k_0 is a free space wave number. Similarly, for an inhomogeneous medium of arbitrary index profile with index varying from n_{min} to n_{max}, the field can be expressed as the superposition of plane waves in all directions with their propagation constants varying from $k_0 n_{min}$ to $k_0 n_{max}$. The method suggested describes a way to find out the weight of each plane wave constituting the field and hence by Fourier inversion, total field can be found out. The method is illustrated by the study of simple integrated optic structures such as bent waveguide with parabolic and exponential index profile. After finding the field, the propagation constants of individual modes are found out using correlation method[3]. The results obtained are in good agreement with analytical results.

References

1 FEIT, M. D AND FLECK, J. A *Appl Opt.*, 1978, **17**, 3990–3998.

2. VAN ROEY, J., VAN DER DONK, J. AND LAGASSE, P E. *J. Opt. Soc. Am*, 1981, **71**, 803–810

3 FEIT, M. D AND FLECK, J A. *Appl Opt*, 1979, **18**, 2843–2855.

Thesis Abstract (M.Sc. (Engng))

Some studies on microprocessor–based ignition timing control system for two-stroke engines by M. N. Kumar.
Research supervisors: M. V. Narasimhan and H. S. Jamadagni.
Department: Mechanical Engineering.

1. Introduction

In the last decade, the growth of two wheeler industry in the country has been phenomenal. Several models of two-stroke, spark-ignition engines with a displacement volume around 150cc in scooters, 80 to 100cc in mobikes and 50 to 60 cc in mopeds have appeared. There have been attempts to develop engines with much lower displacement of 20 to 35cc for mopeds. In particular, the population of the 50cc engines is already very high and there is a clear trend of their numbers increasing further.

Simplicity appears to be the sole virtue of the small-displacement two-stroke spark-ignition engine. The need for improving emission, torque and fuel economy in this class of engines is imperative. In this class of engines, ignition characteristics and timing are not only crucial but also amenable to modification retaining the overall mechanical simplicity.

Optimum ignition timing characteristic is engine-specific and is influenced by many parameters such as speed, load-equivalence ratio, atmospheric humidity, ambient pressure, dilution of fresh charge, fuel composition and knock. But the major parameters which influence the ignition timing characteristics are speed and load. A typical optimised ignition timing characteristic is shown in Fig. 1[1].

Microprocessor-based timing control system only can meet such a complicated ignition timing requirement. Its feasibility has been demonstrated in several experimental systems and in production models of automotive 4-stroke multicylinder engines. The current investigation is aimed at developing a microprocessor-controlled ignition timing control system for two-stroke engines.

Microprocessor control system requires input from sensors. Implementation of cost-effective microprocessor-controlled systems is closely linked with design and development of simple and reliable sensors and electronics. Thus control sensor art plays an important role in the implementation of microprocessor control.

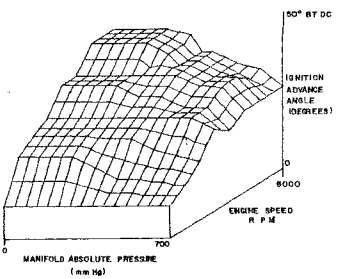

FIG. 1 Ignition requirements of 1-851, 4 CLY carbureted engine optimized for minimum BSFC as function of absolute manifold vacuum and engine speed.

2. Operating condition

The definition of operating condition decides the sensors to be used. The currently available systems use manifold pressure and rpm as the major operating parameters, *i.e.*, speed and load[2,3]. The manifold pressure sensor, however, needs special manufacturing techniques and is therefore generally costly. Further, the manifold pressure is known to fluctuate even under steady-state conditions. To find mean value further processing of the output signal is required. Thus, it was felt that the operating condition should be redefined.

Manifold pressure is a function of speed and throttle. Thus, operating condition can also be defined in terms of rpm and throttle position. The throttle position can be measured easily using a potentiometer. Further, the throttle does not vary under steady-state operating condition thereby avoiding postprocessing.

Throttle plate is generally a cylinder or a plate. The per cent throttle area change, with respect to per cent throttle opening, is maximum at 50 per cent throttle opening. In digital systems, signals are measured as a fraction of a certain reference signal and expressed as an n bit number. Considering a resolution of 1 per cent throttle area opening as adequate, it is concluded that a 7-bit resolution of throttle position is adequate for control purposes. Thus, load sensing by measuring the throttle valve offers advantage of cost saving and simplicity.

3. Crank-angle sensor

Although operating condition is defined by speed and throttle, the control system needs one more vital input, the crank angle, for execution of the spark.

In earlier systems, the crank-angle information is obtained essentially from flywheel gear teeth. As the flywheel has 70 to 120 teeth, to get required crank-angle resolution of less than a degree, some special techniques were used[2,3]. To sense the gear teeth, magnetic reluctance, electromagnetic and Hall effect–type sensors have been used[4]. When this method is used, a separate sensor is needed to get the reference signal.

If all positions of the crank shaft are to be recognised, the signal from the sensor should be analog. If the analog signal generator is used for sensing the crank shaft position, the positional accuracy depends only on the hardware. A single analog sensor would be adequate to find the absolute position of the crankshaft as against reference position and angular position sensors. Further interface electronics is considerably simplified.

Different concepts for continuous signal crank-angle sensors based on variable inductance, Hall effect,

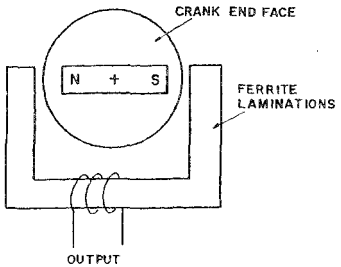

FIG. 2 Magnetic type crank angle sensor.

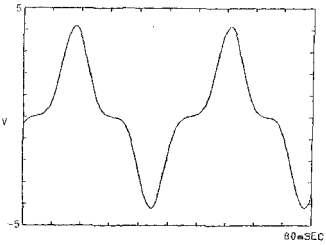

FIG. 3. Output of magnetic sensor

photoelectric effect and magnetic type were examined. The-magnetic type sensor was investigated further as it is simple and easy to fabricate. One more advantage is that this sensor gives rpm information also. The proposed sensor is shown in Fig. 2.

The output of such a sensor is given by

$$V = K\ W\ \phi_m \cos\ \theta$$

where K is constant, W, angular velocity, ϕ, flux and θ, crank angle.

It can be seen from the above relation that the output of the sensor is a function of the angular velocity, *i.e.*, rpm. Thus, at any given crank angle the sensor output voltage increases with speed. To recognize the required crank angle using this sensor, ratiometric and absolute voltage methods have been examined.

3.1. *Ratiometeric method*

In this method, the ratio of the output to the peak value is used to recognise the crank angle.

$$V/(K\ W\ \phi_m) = \cos\ \theta.$$

As this ratio is independent of speed, the crank angle can be easily recognised. This method can be translated into hardware easily by making the reference voltage of the analog-to-digital converter equal to the peak value.

A magnetic-type sensor was fabricated and tested. The output obtained from the sensor is shown in Fig. 3. The distortion at zero crossing is consequent to the finite area of the magnetic pole and core. To reduce distortion an offset was created between axes of the magnet and core. The waveform shape improved as the offset was increased along with a drop in the amplitude. The crank-angle resolution obtained with an offset of 16 mm was 0·6 degrees.

3.2. *Absolute voltage method*

In the memory of the control system, the spark timing, *i.e.*, some crank angle, is stored against the speed and throttle. Since speed is known, spark timing can also be stored as the output voltage of the crank-angle sensor. This method is named as absolute voltage method. In this method also the peak value is measured to find the speed. The resolution obtained in this method depends on the speed. The actual resolution obtained is 1·57° at 600 rpm and 1·6° at 6000 rpm.

4. Hardware and software

Different possible combinations of speed and crank-angle sensing methods were evaluated. The absolute

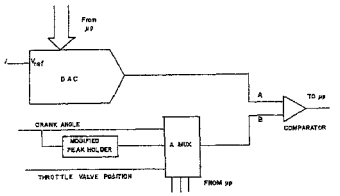

FIG. 4 Block diagram of hardware

voltage method of crank-angle recognition and magnetic sensor output peak for speed measurement was proposed to be implemented on hardware. The minimal hardware required was found by analysis. The block diagram of the hardware is shown in Fig. 4. The hardware was assembled and tested.

Different tasks to be executed by the microprocessor were formulated in chronological order Then the software modules were written and tested separately.

5. Results

When the system was tested, the following results were obtained.

1. The speed is recognised to a resolution of 44 rpm.
2. The throttle area is recognised to a resolution of 1 per cent of the throt area of the carburetor.
3. The microprocessor control system utilises only 25 per cent of the total time available at 6000 rpm and 2·5 per cent at 600 rpm.
4. The spark timing accuracy is 1·71° at 600 rpm and 1·6° at 6000 rpm.
5. The system's performance under transient operating conditions is satisfactory.

6. Conclusions

The hardware configuration of the proposed microprocessor-controlled ignition timing control system for two-stroke engine can be obtained as a single chip to achieve compactness, simplicity and low cost. The system time is under utilised and is capable of managing additional parameters. The proposed ignition timing control system has the potential for implementation on two-stroke engines.

References

1. JOHNSON. R. W., NEUMAN, J. G AND AGARWAL, P. D. — Programmable energy ignition system for engine optimisation, *SAE Trans.*, 750348.
2. SIMANTIS, D. J. — MISAR· An electronic advance, *Automot. Engng*, 1977, **85**, 24–29
3. IKEURA, K., HOSAK, A. AND YANO, T — Microprocessor control brings about better fuel economy with good drivability, *SAE Trans.*, 800056
4. WOLBER, W. G. — Automotive engine control sensors 80, *SAE Trans.*, 800121

Thesis Abstract (M.Sc. (Engng))

Hydraulic transients in pumping systems with air chamber by Lakshmi Naga Padma Kandula.
Research supervisor: K. Sridharan.
Department: Civil Engineering.

1. Introduction

This work presents the results of an extensive computational study of the transients in pumping mains

following power failure and single-pump tripping. The studies are of practical relevance to pumping mains of water supply systems, provided with an air chamber for surge protection. The influence of various parameters on the transients following power failure in system provided with air chamber has been studied by earlier investigators[1]. However, there is some disagreement regarding the effects of the loss parameter for flow out of the air chamber, DHOR1, on the downsurge following power failure. Some investigators[1] assert the existence of an optimum value of DHOR1 that will minimise the downsurge while others[2] advocate providing DHOR1 = 0·0. The traditional design procedure[3] for air chamber ignores pump motor inertia effects and assumes instantaneous closure of the nonreturn valve, provided upstream of the air chamber, following power failure. There is an increasing awareness of the deleterious effects of nonreturn valve malfunction in pumping systems, but these are usually ignored in air chamber design. It is generally assumed that power failure results in the most critical transient condition, but some accidents indicate that failure of one pump out of several pumps operating in parallel could also result in severe transient pressure.

With this background in view, the present study was undertaken with the following scope

1 The influence of loss parameter for flow out of the air chamber, DHOR1, on the downsurge following power failure

2. The effects of (a) delayed closure of pump and/or air chamber nonreturn valves, (b) pump motor inertia and (c) air chamber location, on the transients following power failure, in the transmission main and in the short reach between the pump and air chamber.

3. The effects of (a) delay in nonreturn valve closure, (b) pump motor inertia, (c) number of pumps, (d) pipe size and length, and (e) valve closure pattern on the transients following single pump tripping.

2. Methodology

The method of characteristics employing finite difference scheme is used to solve the hyperbolic partial differential equations, representing the equations of motion and continuity, governing the unsteady flow. The dependent variables, head and velocity at different locations in the pipe, at different times, are calculated. The boundary conditions at the pump end, reservoir end and various internal boundaries such as the junction, air chamber, one-way surge tank, etc., relevant to the systems studied, are used. The steady-state conditions of head and velocity existing before power failure or single pump tripping are used as the initial conditions. Wherever nonlinear equations are to be solved, Newton–Raphson method is used.

3. Effect of outflow loss parameter

A parametric study is carried out to estimate the effect of the loss parameter for flow out of the air chamber, DHOR1, on the downsurge following power failure. The effects of the variation in DHOR1 values over the range of 0·0 to 0·3 on the minimum pressures are presented in a series of diagrams, for various combinations of the other parameters, *viz.*, pipeline, air chamber capacity and line friction parameters. A total of over 400 computational cases are studied. It is found that the optimum value of DHOR1 which minimises downsurge is different for different locations along the alignment, with its value decreasing with increase in relative distance from the air chamber. Near the reservoir end, the optimum value of DHOR1 is 0·0 for all parameter combinations likely to occur in water supply systems. The rate of deterioration in downsurge as DHOR1 increases beyond the optimum value where it exists is more than the improvement in downsurge as DHOR1 increases from 0·0 up to the optimum value. This trend is particularly pronounced for small air chamber capacities and for locations near the reservoir end.

4. Pump–Nonreturn valve–Air chamber system

The effects of delay in nonreturn valve closure, pump motor inertia and air chamber position on the transients following power failure are evaluated by a series of case studies done for three systems. System I is of large size in which a discharge of 3·15 m^3/s is pumped through a 19·6-km long, 1750-mm pipe

under a head of 170 m System II is of moderate size with a discharge of 1·87 m^3/s in a 3·2-km long 1450-mm pipe under a head of 88 m. System III is a small one in which a discharge of 0·40 m^3/s is pumped through a 600-mm pipe over a distance of 660 m under a head of 112 m. The parameters varied are delay in the closure of the air chamber and pump nonreturn valves following flow reversal, WR^2 of the pump motor and air chamber position. Computations are made for over 50 cases. It is found that ideal closure of either one of the nonreturn valves is sufficient to prevent deterioration of pressures in the transmission main. When there is delay in the closure of both the valves, there may be significant deterioration of pressures except for long length systems. The pressures in the short reach between the pump and air chamber are considerably higher than the pressures downstream of the air chamber, for delayed closure of the nonreturn valves. There is a critical delay, d_c, in the closure of the valves which results in the greatest head rise. At this critical delay, the maximum head at the pump nonreturn valve is found to be 1·5, 1·5 and 1·8 times the working head in Systems I, II and III, respectively. The maximum expanded air volume which is used to decide the size of the air chamber is significantly larger for delayed closure of the valves than the value obtained by analysis based on instantaneous valve closure for small length systems. The decay of the high pressures occurring between the nonreturn valve and air chamber occurs only very close to the air chamber. Hence, when the air chamber has to be provided at some distance away from the pump house, it is advisable to provide the nonreturn valve close to the air chamber to localise the high pressures.

5. Single pump tripping

The transients following single pump tripping are studied for a large system in which the system details are similar to those for System I referred earlier. The parameters varied are delay in pump nonreturn valve closure, pump motor inertia, number of pumps, delivery pipe size, delivery pipe length and valve closure pattern. Four types of valve closures are considered, an instantaneous closure of a single door valve, three-step closure of a multidoor valve, a uniform gradual closure and a two-speed closure. Computations are made for over 100 cases. It is found that severe transients following single pump tripping are localised to the short reach upstream of the delivery manifold junction and downstream of the nonreturn valve on the delivery pipe of the failed pump. The transients are even more severe than those resulting from power failure. Even a small delay of 0·5 s in the nonreturn valve closure results in a maximum head 1·9 times the working head for the system studied. The transients worsen with increase in delay up to the critical delay, d_c, with the maximum head being 2·6 times the working head for $d_c = 2·9$ s. Pump motor inertia effects have considerable influence on the transients following single pump tripping as compared to power failure. The maximum pressure due to single pump tripping reduces significantly as the number of pumps is reduced for a system without an air chamber, while this reduction is only marginal for a system with an air chamber. The decay of the high pressures occurring at the nonreturn valve following single pump tripping takes place only very close to the delivery manifold.

The maximum pressure resulting from the closure of a multidoor valve is dependent essentially upon the time of closure of the last door. The beneficial effects of uniform gradual closure are only felt beyond a certain duration of closure. But for such durations, there is a risk of occurrence of large reverse rotation speeds of pump. An effective method of controlling the pressure rise without allowing reverse rotation, following single pump tripping, is to use a two-speed closure with a rapid initial closure followed by a slow closure for the last 10 per cent opening. Increasing the delivery pipe diameter also helps to reduce the severity of transients following single pump tripping.

References

1. FOK, A. T K. Design charts for air chambers on pump lines, *J. Hydraulics Div.*, ASCE, 1978, **104** (HY9), 1289–1303.

2. RUUS, E. Charts for waterhammer in pipe lines with air chambers, *Can. J. Civ. Engng*, 1977, **4**, 40–46.

3. PARMARIAN, J *Waterhammer analysis*, 1983, Dover.

Thesis Abstract (Ph.D.)

Similar solutions and general correlating parameters in non-equilibrium gas-particle nozzle flows by R. K. Thulasiram.
Research supervisor: N. M. Reddy.
Department: Aerospace Engineering.

1. Introduction

For the past several years, high-energy propellants are in much use for the attainment of large amount of thrust to lift heavy vehicles for launching satellites and other space stations. These propellants use metal powder for the stability of combustion which are burnt in the combustion chamber, get oxidised and come out as metal-oxide particles[1]. Hence, the entry into rocket nozzle will not be of pure hot gas but a mixture of gas and metal-oxide particles. As these particles do not do any work, they lag in responding to the nozzle expansion process[2]. Moreover, the particles are dragged out of the nozzle by the forces exerted by gas and hence gas will lose a part of its energy. This way the effective thrust may be reduced. Therefore, for any accurate analysis, the nozzle flow problem has to be treated as a two-phase flow consisting of gas and particles with separate velocities and temperatures[3]. This is a typical example of two-phase nozzle flows. In the present work, a similar solution approach has been introduced for the analysis of non-equilibrium gas-particle nozzle flows and general correlating parameters for the two-phase flow have been obtained.

2. Concept of virtual area and virtual speed of sound

The existing theoretical analyses of gas–particle nozzle flows use the speed of sound pertaining either to equilibrium or frozen limits between the two phases[4]. Since the nozzle flow has to be treated as a two-phase flow expansion process as mentioned earlier, the corresponding mixture thermodynamic properties have to be used for any analysis. Therefore, the use of the existing definition for speed of sound of gas–particle mixture to the current problem of non-equilibrium two-phase flow is not appropriate. In the present work, new definitions for effective Mach number which are called as 'virtual area ratio', 'virtual speed of sound' and 'virtual Mach number' are proposed for non-equilibrium gas–particle nozzle flows. Using these definitions simple area ratio–Mach number relations which are very similar to those of pure gas case have been deduced[5] from continuity and momentum equations. It is also shown from a typical nozzle-flow computation that the virtual Mach number attains a value of unity at the minimum value of virtual area ratio.

3. Similar solutions

For the current investigation, by introducing new independent variables, certain transformations of the equations governing the non-equilibrium gas-particle nozzle flow have been worked out using the new definitions and new expressions derived earlier, which reduce them into a universal form and a general correlating parameter has also been obtained by grouping the terms resulting out of these transformations[6]. The general correlating parameter includes all the parameters specifying the gas and particle characteristics as well as the nozzle shape. Therefore, the results obtained for a single value of this general correlating parameter will be valid for several combinations of the gas and particle characteristics. The cumbersome job of repeating the solution procedure for every initial condition can thus be obviated and hence the computer time required could be reduced significantly. Various physical phenomena occurring in the nozzle when the particles occupy negligible and finite volume in the mixture have been discussed[7]. The potentiality of the similar solution method in studying these physical phenomena without many simplifying assumptions has also been highlighted.

4. Effect of particles on gasdynamic laser performance

Same kind of two-phase flow problem occurs in a very recently evolved field called gasdynamic lasers

(GDL). In this system, a hot mixture of CO_2, N_2 and He gases is expanded through a supersonic nozzle and due to sudden cooling, population inversion occurs among the different energy levels of CO_2 and this leads to the fascinating idea of gasdynamic laser. Highly excited N_2 can be obtained by burning metal powder in air which is then mixed with cold CO_2 and He mixture and then expanded through the nozzle for the laser action. Burning metal powder in air will have products of highly excited N_2 and metal oxide particles and hence the nozzle flow will consist of both solid and gas phases Here, the presence of the particles may affect the lasing performance of a gasdynamic laser.

For a mixture of CO_2–N_2–He gases, apart from gasdynamic conservation equations of the two phases, one has to include two vibrational relaxation rate equations for the two vibrational modes of higher and lower energy levels of CO_2. The coupled gasdynamic and vibrational rate equations have been transformed into a similar form and then solved. From the results obtained[9,10], the effect of the particles could be observed to be too adverse when the size becomes smaller. Also when the loading ratio is increased, significant effect of particles on the lasing efficiency is observed.

5. Conclusions

The major conclusions are: Hitherto non-available simple Mach number–area ratio relations and similar solutions have been obtained for the non-equilibrium gas–particle nozzle flows and the cumbersome job of repeating the solution procedure for every given initial and different parametric conditions could thus be obviated. The size of the particles plays an important role in the nozzle expansion process. The flow reaches an isothermal condition at high particle-loading ratios. The particles affect the vibrational relaxation phenomena adversely. The optimum lasing performance of the CO_2–N_2–He gasdynamic laser is affected significantly when particle size is reduced or when the loading ratio is increased. The correlating parameter obtained from the present study contains all the parameters of the problem and it is shown that different values for this parameter represent the complete spectrum of non-equilibrium flow from near-equilibrium flow to near-frozen flow regimes.

References

1. WESLEY, R. C. III, GARLAND, L. G. AND WIGHTMAN, J. P. — Analysis of mid-tropospheric space shuttle exhausted Al_2O_3 particles, *Atmos. Environ.*, 1987, **21**, 1187–1196.
2. GILBERT, M., DAVIS, L. AND ALTMAN, D. — Velocity lag of particles in linearly accelerated combustion gases, *Jet Propulsion*, 1955, **25**, 25–30.
3. MARBLE, F. E. — Dynamics of a gas containing small solid particles, *Fifth AGARD Combustion and Propulsion Colloquia*, 1963, pp 175–214, Pergamon.
4. RUDINGER, G. — Fundamentals of gas-particle flows, Vol 2, in *Handbook of powder technology*, (Williams, J. C. and Allen, T., eds), 1980, Elsevier
5. REDDY, N. M AND THULASIRAM, R. K. — Transformations of two-phase nozzle flow equations into pure gas type by introducing virtual area and virtual Mach number, *Proc. 17 Int. Symp on Shock Tubes and Waves*, Bethlehem, USA, July 1989, American Institute of Physics, AIP Conf. Proc. No. 208, pp. 732–737.
6. REDDY, N. M AND THULASIRAM, R. K. — Similar solutions in non-equilibrium nozzle flows of gas–particle mixtures, *Proc. 16 Int. Symp. on Shock Tubes and Waves*, July 1987, pp 227–233
7. THULASIRAM, R. K. AND REDDY, N. M. — Similar solutions in non-equilibrium nozzle flows of gas–particle mixture including finite volume effects, *J. Aeronaut Soc India*, 1989, **41**, 419–425.
8. THULASIRAM, R. K. AND REDDY, N. M. — Simultaneous particles and vibrational mode relaxation in gas–particle nozzle flows—similar solutions, *Sixth Natn. Conv. Aerospace Engineers on Aerothermodynamics of Internal Flows*, IIT, Bombay, India, Jan. 24–25, 1991, pp 114–131
9. THULASIRAM, R K., REDDY, K. P. J. AND REDDY, N. M — Theoretical study of optimum performance of two-phase flow CO_2 gasdynamic laser, *Appl Phys. Lett.*, 1987, **50**, 789–791.
10. THULASIRAM, R. K., REDDY, N. M. AND REDDY, K. P. J. — Gain characteristics of two-phase flow 10.6μm CO_2 gasdynamic laser, *J. Aeronaut. Soc. India*, 1990, **42**, 13–18.

Thesis Abstract (Ph.D.)

Kinetic upwind method for inviscid compressible flows by J. C. Mandal.
Research supervisor: S. M. Deshpande.
Department: Aerospace Engineering.

1. Introduction

The present work is mainly concerned with the development of a class of new upwind methods, called kinetic flux vector splitting (KFVS), for numerical solution of inviscid gasdynamics The need for the development of a new method arises from the fact that today's algorithms, though more accurate and robust as compared to those in the earlier days, are still unsatisfactory in many respects. Even though the causes of deficiencies of the method are quite clear and the desirable properties of an 'ideal' method are well understood there is very little idea about how to specify these properties without a contradiction.' The present research started with the aim of approaching the problem from a completely new angle so as to possibly avoid conventional pitfalls. This exercise has finally turned out to be very interesting and fruitful[1].

The KFVS methods are based on the fact that the Euler equations are the moments of the Boltzmann equations whenever the velocity distribution function is a Maxwellian[2-5]. The present work aims at fully exploiting the richness of this connection between the Boltzmann equation and the Euler equations. The important consequences of this exercise are the following:

The development of a class of new schemes which are robust and conservative, satisfy upwind property and entropy condition, and are capable of yielding accurate wiggle-free solutions to a wide variety of problems covering subsonic to hypersonic flow regimes

The most significant outcome of the above approach is the development of a new treatment of flow-tangency boundary condition, called kinetic characteristic boundary condition (KCBC). This boundary treatment is based on the specular reflection model of the kinetic theory of gases. The application of this boundary treatment does not necessitate any change in the basic formulation as a result of which all the important properties of the KFVS method remain valid even at the boundary. Furthermore, this boundary treatment is found to be very robust as it is consistent with the theory of characteristics and there is no requirement of additional assumption or use of fictitious grid points for its implementation.

2. Basic concept

The collisionless Boltzmann equation (BE), given by

$$\partial f/\partial t + \vec{v} \cdot \partial f/\partial \vec{x} = 0, \tag{1}$$

where $\vec{v}$ is the molecular velocity vector and $\vec{x}$ the position vector, is a linear and hyperbolic equation for a single scalar f (namely, the velocity distribution function). The collision term is not considered in our analysis because it vanishes in the Euler limit. The collisionless BE is thus one of the most simple forms of partial differential equations whose exact solution can be readily written as

$$f(t + \Delta t, \vec{x}) = f(t, \vec{x} - \vec{v}\Delta t). \tag{2}$$

Now an upwind method for (1) can be obtained starting with the solution (2). It is therefore natural to think of an upwind method for the Euler equations than can be obtained by taking the moments of the upwind method of the BE. This procedure, referred to as 'moment method strategy' is the basis of the present method. In principle, this procedure is very simple as it avoids dealing directly with the coupled nonlinear conservation laws. Due to the relative ease in dealing with (1), we try to establish various properties and conditions, etc., at the Boltzmann level and finally obtain these conditions at the Euler level using moments. It is later on confirmed by eigenvalue analysis that the implementation of the upwind logic at the Boltzmann level leads to an upwind method for the Euler equations.

It should be noted that the scheme for the Boltzmann equation is only at the conceptual level in KFVS. While solving the Euler equations by KFVS schemes the numerical solution of the Boltzmann equation is never required.

3. Results and discussion

The present method and associated algorithms have been validated through numerous case studies. They are: 1D shock tube problem, 2D shock reflection problem involving supersonic and hypersonic Mach numbers, and transonic and supersonic flows over circular arc bump in a channel. The 2D shock reflection problem has also been solved by employing MacCormack space marching scheme in order to demonstrate that the KCBC can be used in conjunction with other finite difference schemes. Based on these studies it is concluded that the connection between the Euler equations and the Boltzmann equation is rich enough to permit construction of new kinetic numerical method which is robust and conservative, satisfies upwind property and entropy condition, and is capable of yielding accurate wiggle-free solutions to a wide variety of problems. Further, it is shown that the present formulation lends itself easily to the construction of a new treatment of flow-tangency boundary condition in conformity with the theory of characteristics and without involving any extra 'boundary procedure'.

References

1. DESHPANDE, S. M. AND MANDAL, J. C — Kinetic theory based upwind method for inviscid compressible flows, *Theor. Appl. Mech.*, (Bulgarian Academy of Sciences, Sofia), 1988, **3**, 32–38

2. MANDAL, J. C AND DESHPANDE, S. M — Higher order accurate kinetic flux vector splitting method for Euler equations, *Notes Numerical Fluid Mech.*, (Viewweg), 1989, **24**, 384–392

3. MANDAL, J. C AND DESHPANDE, S. M. — An upwind Euler space marching using kinetic flux vector splitting with a new treatment of boundary condition, *Proc. Fourth Asian Congress of Fluid Mechanics*, University of Hong Kong, Hong Kong, August 21–25, 1989, Vol I, p. F-49

4. DESHPANDE, S. M., MANDAL, J. C. AND GHOSH, A. K — A class of Boltzmann schemes for inviscid compressible flows, Paper presented at the *Workshop on Boltzmann Schemes*, Kaiserslautern, FRG, January 11–13, 1990.

5. DESHPANDE, S. M., MANDAL, J. C AND GHOSH, A. K. — Maxwellian distribution based Boltzmann schemes for the Euler equations, *Proc Seventeenth Inter. Symp. on Rarefied Gas Dynamics*, Rheinisch Westfaelische Technische Hochschule, Aachen, FRG, July 8–14, 1990.

Thesis Abstract (Ph.D.)

Development of a three-degree of freedom elastically forced oscillation rig for the measurement of direct and coupling dynamic stability derivatives of aircraft and missile models by B. R. Srinivasa Rao.
Research supervisor: G. N. V. Rao.
Department: Aerospace Engineering.

1. Introduction

Modern flight vehicles are required to execute maneuvres in extreme flight conditions where complicated flow phenomenon are induced due to flow separation, interference, vortex shedding, etc. These phenomenon are highly motion sensitive and configuration dependent. Also, the unsteady and nonlinear forces may lead to strong coupling effects between longitudinal and lateral modes of motion. All these effects cannot be accounted for satisfactorily by theoretical methods alone. Where theoretical solutions are possible,

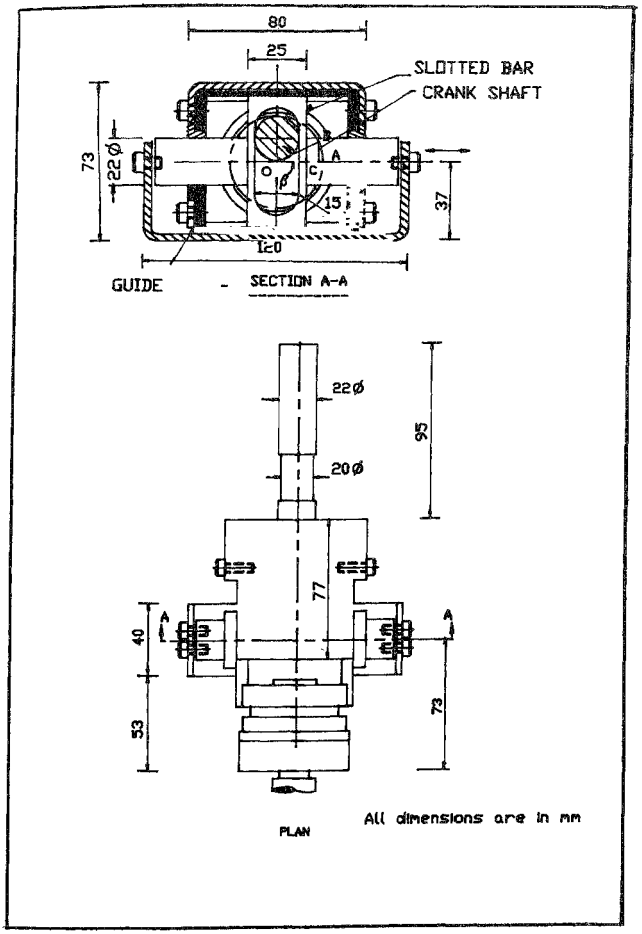

FIG. 1. Scotch-yoke mechanism

experimental confirmation is most desirable. Thus, experimental determination of aerodynamic stability derivatives has become important in the investigation of handling characteristics of high-performance flight vehicles.

Measurement of aerodynamic stability derivatives requires some kind of oscillatory mechanism to oscillate a model in various degrees of freedom and extraction of damping, stiffness and other derivatives corresponding to mode of oscillation excited. Literature survey has shown that although several techniques for experimental determination of derivatives are available[1], they are mostly suited to the extraction of a limited number of important derivatives. This is generally due to the limitations of the capability of the stability-derivative rig. In many cases, the rig is capable of oscillating the model in just one degree-of-freedom oscillations only, yielding damping and stiffness derivatives in that mode. If several derivatives are required to be measured, the rig must be capable of oscillating the model in multiple degrees-of-freedom[2]. The design of such a rig is obviously more elaborate.

In this work, development of a forced oscillation rig to measure direct and coupling dynamic stability derivatives of aircraft and missile models in a wind tunnel, including Magnus derivatives, is described and followed by the presentation of experimental results for a finned body of revolution. This new three degrees-of-freedom oscillatory rig was used to measure 18 dynamic stability and Magnus derivatives. The design of the rig, its fabrication, testing, method of extraction of the derivatives, etc., comprise the main contribution of this work. It was also desired to avoid the use of electro-magnetic devices generating linear motion directly by a much smaller scotch-yoke, driven by a small electric motor. Hence, it was decided to develop the design based around a scotch-yoke.

2. Development of the rig

The dynamic stability rig as conceived, designed and fabricated consists of two mechanisms, one to convert the rotary motion of a dc motor into translatory oscillatory motion and the other to convert the translatory oscillatory motion into three-degrees-of-freedom oscillations. The model mounted on the mechanism executes three-degrees-of-freedom oscillations in rolling, yawing and swerving. As stated earlier, linear motion was generated through a scotch-yoke mechanism mounted at the end of a long shaft driven by a dc motor. The mechanism is supported in a housing which itself is supported on a stationary tube through which the drive shaft passes (Fig. 1). The stationary tube is supported at an intermediate position such that its upstream influence on the model will be negligible and the natural frequency of the overhanging portion (tube, driveshaft, scotch-yoke and model) will be much higher than the driving frequency.

The scotch-yoke mechanism consists of a slotted bar and eccentric shaft assembly and converts the rotational motion by coupling the driving motor to an eccentric shaft rolling inside the slotted bar, giving the bar a sinusoidal translatory motion. The frequency of translational oscillations can be adjusted by controlling the dc motor speed and the amplitude kept constant. The model driving mechanism consists of two flexures one of which connects the model and oscillating bar of the scotch-yoke and the other flexure connects the stationary housing of the scotch-yoke to the model. The flexures are designed to enable driving the model into resonance in rolling, yawing and swerving modes by the translatory sinusoidal oscillations of the scotch-yoke mechanism. The natural frequencies for each of the modes of oscillations were different, being typically 3, 5 and 6 Hertz, respectively. A particular mode of oscillation is excited by adjusting the motor speed to the appropriate frequency. When the required mode of oscillation is excited, the mode excited will be of large amplitude but by designing the frequencies of the modes to be close, the model is forced to execute coupled motion. This is because the tail ends of the response in the other modes overlap with that of dominant mode. The derivatives are obtained by solving the three-degree-of-freedom coupled equations. The equations contain a total number of 18 unknown derivatives. Eighteen equations are obtained from the three modal equations by splitting them into real and imaginary parts and inserting data measured in three different modes of oscillation at three known inertias of the model obtained by adding extra masses. Inertias were determined by Bifilar-suspension technique of measurement. The model displacements were measured by taking the outputs of six accelerometers mounted at two stations on the model. Excitation was measured by six strain-gauge bridges cemented on the forward

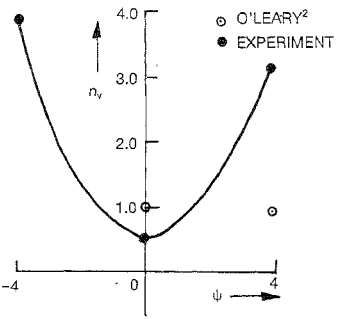

FIG 2 Derivative nv obtained from side slipping motion.

and rear flexures. The strain-gauge bridge outputs were calibrated. The entire data were recorded on analog magnetic tape and later quantified. The solution of equations yielded 18 derivatives.

The test procedure is to oscillate the model at or near the natural frequency of each mode in turn and record the displacement, applied excitation and frequency parameters on analog tape. Tests were repeated after changing the mass of the model in order to obtain measurements at three known masses. Recordings were made with wind-off and wind-on. The aerodynamic derivatives were computed as the difference between the wind-off and wind-on values. Figure 2 shows a typical comparison of the present results with the data reported by a more complicated rig[2].

3. Conclusion

It is concluded that the principle conceived and developed for the new rig can be used for experimental measurement of aerodynamic stability derivatives conveniently and is versatile. It is believed that the present rig is a great deal simpler than many of the existing rigs for such measurements besides possessing the advantage of being able to measure Magnus derivatives also.

References

1 ORLIK-RUCKEMANN, K J. *Review of techniques for determination of dynamic stability parameters in wind tunnels,* AGARD LS-114 1981, Paper H3.

2. O'LEARY, C. O *Wind tunnel measurement of lateral aerodynamic derivatives using a new oscillatory rig with results and comparisons for the Gnat aircraft,* RAE Technical Report 77159, 1977

Thesis Abstract (M.Sc. (Engng))

An explicit optimal guidance for a lanunch vehicle by R. Vijaya Vittal.
Research supervisor: M. Seetharama Bhat.
Department: Aerospace Engineering.

1. Introduction

An accurate guidance scheme capable of steering a launch vehicle along a truly three-dimensional launch

trajectory is required due to limitations in the launch facilities, the associated land mass constraints and the requirement of fuel optimality, especially for PSLV (Polar Satellite Launch Vehicle) class of vehicles[1]. Accurate injection of payload by the launch vehicle reduces the onboard fuel expenditure necessary for correcting any injection errors, thereby enhancing the satellite life time. A highly accurate, optimal three-dimensional guidance logic is developed in this work along with a preliminary study of the onboard implementation requirements. The general explicit guidance schemes exhibit numerical instability closer to injection point. This difficulty is attributed to the demand for exact injection which in turn calls for finite corrections to be enforced in a relatively short time. A separate terminal guidance based on minimization of quadratic penalty on terminal injection errors rather than demanding an exact injection is also proposed. A simple strategy to dynamically determine the appropriate transition to the terminal guidance is also developed.

2. The guidance logic

The explicit guidance schemes determine the required thrust orientation and duration of thrusting based on present and target states alone. The guidance computations are performed at regular intervals throughout the guided phase to ensure the attainment of the terminal conditions against reasonably large disturbances. Such real-time computations are facilitated by the equivalent uniform gravity acceleration assumption[2,3]. Accuracy or optimality of the steering logic is not sacrificed by the above equivalent constant gravity representation when correct average estimates for the gravitational acceleration can be determined. In the present guidance scheme, the actual velocity and position vector contributions of spherical earth gravitational field over the future trajectory are accurately estimated by Enke's[4] method and averaged over flight duration[1,5] as $\mathbf{g}_v$, $\mathbf{g}_p$, respectively.

Fuel minimization is the primary objective for the guidance scheme apart from the requirement of accurate injection[2]. For the non-throttleable rocket engines, this is equivalent to minimum time of burn. Employing minimization of thrusting time as the performance criterion, it can be shown that the optimal thrust orientation must coincide with the costate vector $\mathbf{p}_v(t)$, associated with the velocity vector[1-3] (t is the time variable). It may be recalled that the increments to the current state in terms of position and velocity vectors are provided by proper thrust steering programs to attain the target state in minimum time. Such increments in the position and velocity vectors due to thrust alone define a plane which may be called as a correction plane. The optimal unit thrust vector is confined to this correction plane throughout the remaining part of the powered stages of the multistage vehicle, even though the actual position vector traverses along a three-dimensional path[1,3,5]. Hence, the optimal unit thrust vector $\hat{u}(t)$ that is coincident with the costate vector $p_v(t)$, can be expressed as,

$$\hat{u}(t) = [\hat{I}_{xc} + \hat{I}_{yc}\, P(t-T_c)]/[1+P^2(t-T_c)^2]^{1/2} \qquad (1)$$

where, $\hat{I}_{xc}$, $\hat{I}_{yc}$ are the unit perpendicular vectors in the correction plane, P a parameter associated with the rate of turn of the thrust vector, and T_c the thrust vector time constant. The optimal unit thrust vector $u(t)$ (eqn 1) indicates that the steering angle measured from $\hat{I}_{xc}$ follows a linear tangent law. This steering angle defined in the correction plane can then be received into the pitch and yaw angles in any inertial coordinate frame.

Generally, the point of injection on the desired orbit is unspecified, amongst the six orbital parameters which define the target state. An estimate or range angle θ_T, however, fixes the target state. The freedom in target state also leads to the reference unit vector $\hat{x}_{xc}$ to be defined along the direction of total velocity vector increment required of the vehicle thrust[5]. Finally, six terminal conditions are to be satisfied by a proper choice of the guidance parameters, *viz.*, P, T_c, θ_T, *Tgo* (time to thrust-cutoff) and two degrees of freedom in mutually perpendicular unit vectors $\hat{I}_{xc}$, $\hat{I}_{yc}$ confined to the correction plane.

3. Guidance computations

The required increments in position and velocity vectors to be gained through thrusting to attain the desired orbit can be estimated as:

$$\mathbf{V}_{thR} = \mathbf{V}_T(\theta_T) - \mathbf{V}_0 - \mathbf{V}_g(g_v, Tgo);\ \mathbf{R}_{thR} = R_T(\theta_T) - \mathbf{R}_0 - \mathbf{R}_g(g_p, Tgo) - Tgo\mathbf{V}_0 \quad (2)$$

where $\mathbf{V}_0$ and $\mathbf{R}_0$ are the navigational data on the present state of the vehicle, and *Tgo* is the estimate of total remaining time before final injection. The target state is represented by the vector $\mathbf{V}_T$, $\mathbf{R}_T$. The required increments in the velocity and position vectors (eqn 2) are to be matched with those obtained by properly orienting the thrust vector indicated by a correct choice of the optimal guidance parameters. The available increments in velocity ($\mathbf{V}_{thA}(Tgo)$) and position ($\mathbf{R}_{thA}(Tgo)$) vectors due to thrust can be estimated by integrating the vehicle thrust vector over the remaining burn time successively. A simple series approximation to the unit thrust vector (eqn 1) is used in one method of evaluating time integral of thrust vector. An exact method of integrating the steering thrust profile is also developed for the first time[5].

A differential corrector approach is adopted for finding the guidance parameters that decide the unit thrust vector and the suitable injection point on the desired orbit simultaneously, while treating the average gravity vector as constants. A scheme to find an approximate set of starting values of the guidance parameters which are essential for the fast convergence of the differential corrector is also presented[1,5].

The instability at the terminal phase is avoided by using a quadratic penalty on the terminal injection errors, instead of demanding exact injection[6]. The performance index for the terminal guidance is given by,

$$J_t = 1/2\ [\ [\mathbf{V}_{thR} - \mathbf{V}_{thA}(Tgo)]^T\ Q_v[\mathbf{V}_{thR} - \mathbf{V}_{thA}(Tgo)]$$

$$+\ [\mathbf{R}_{thR} - \mathbf{R}_{thA}(Tgo)]^T\mathbf{Q}_r\ [\mathbf{R}_{thR} - \mathbf{R}_{thA}(Tgo)]\ ] + \int_0^{Tgo} dt, \quad (3)$$

where $\mathbf{Q}_v$, $\mathbf{Q}_r$ are weighing matrices associated with velocity and position vector errors. The transversality conditions can be used to express the costate vector associated with the velocity in terms of injection errors as,

$$\mathbf{P}_v(t) = \hat{\imath}_{xc}\ [-Q_{vx}\ [V_{thRx} - V_{thAx}\ (Tgo)]] + \hat{\imath}_{yc}[-Q_r(t - Tgo)[R_{thRy} - R_{thAy}(Tgo)]$$

$$- Q_{vy}\ [V_{thRy} - V_{thAy}(Tgo)]]. \quad (4)$$

Here, subscripts *x*, *y* indicate the $\hat{\imath}_{xc}$, $\hat{\imath}_{yc}$ components, respectively. Since, the optimal unit thrust vector $\hat{u}(t)$ is collinear with $\mathbf{P}_v(t)$, it can be concluded from eqn 4 that as the target is approached the influence on the thrust direction due to errors in meeting the position constraint decreases as the factor $(t\text{-}Tgo)$ monotonically reduces. A robust terminal guidance scheme using the above conclusion and physically realistic simplifying assumptions is developed[7]. A simple dynamic strategy is proposed based on observing changes in guidance parameter *P* associated with thrust vector turn rate, for invoking the terminal guidance, the present terminal guidance scheme involves very simple computations that facilitate faster guidance updates necessary for an accurate thrust cutoff.

4. Simulation study and conclusions

Extensive simulation of the guidance scheme has been carried out using the data corresponding to a typical PSLV class of launch vehicle for injecting a payload into a 900-km Sun-synchronous circular orbit. The major off-nominal conditions considered in the simulation are: fixed errors or random variations in the thrust magnitude, initial state with offsets, and the effects of computational delay The merits of alternative methods for obtaining thrust profile integrals are studied. The high accuracy of final injection (Table I) and the smooth thrust steering angle profiles obtained in simulation study indicate the efficacy of the present guidance scheme. The specified error tolerances for the PSLV mission are (approximate 3 sigma values) ±15 km in altitude, ± 10m/s in velocity, ±0·1 degree in inclination and 0·01 in eccentricity. The errors resulting from simulations of off-nominal conditions indicated in Table I are much smaller than the specified error tolerances. The onboard computational loads are estimated by measuring the execution

Table I
Terminal errors and time of burn in off-nominal simulations

Simulation case	*Errors in*					*Final stage burn time (s)*	*Terminal guidance duration (s)*
	Alt (m)	*Vel (m/s)*	*$R_T - a$ (m)*	*e*	*Orbit normal (deg)*		
	$X10^3$	*X1*	*X1*	*$X10^{-4}$*	*$X10^{-3}$*		
Ideal condition	$3{\cdot}8e^{-4}$	$1{\cdot}6e^{-4}$	−2 652	$1{\cdot}8e^{-4}$	$1{\cdot}9e^{-3}$	383·78	26·5
1% High thrust	2·0849	0·1554	−245·9	2·8846	0·3924	374·65	30·65
1% Low thrust	2·0922	0·1750	317·5	2·8874	0·2871	393·81	29 81
Sensor bias in each component of position (50m) and velocity (5m/s) employed							
+ve bias	0 5517	8·660	−8363·2	12·596	50·33	384·92	52 91
−ve bias	0 6676	8·659	8291 3	12·515	50·45	383·53	67 53
1 s delay for earlier phase and 20 ms delay for terminal phase							
Computational delay	0 0002	0·00012	−3·305	·00228	·00121	383·60	19·60

time, code and data memory requirements on IBM-compatible PC-ATs[5]. The results indicate the feasibility of the present guidance scheme for onboard implementation.

References

1. SINHA, S K., SRIVASTAVA, S. K., BHAT, M. S. AND PRABHU, K. S — Optimal explicit guidance for three-dimensional launch trajectory, *Acta Astronaut.*, 1989, **19**, 115–123
2. LAWDEN, D F — *Optimal trajectories for space navigation*, 1963, Butterworths.
3. PERKINS, F M. — Explicit tangent-steering guidance for multistage boosters, *Astronaut Acta*, 1966, **12**, 212–223.
4. BATE, R. R., MULLER, D. D. AND WHITE, J E. — *Fundamentals of astrodynamics*, 1971, pp 360–396, Dover.
5. VIJAYA VITTAL, R. AND SEETHARAMA BHAT, M. — An explicit closed loop guidance for a launch vehicle, *Acta Astronaut*, 1991, **25**, 119–129.
6. BITTNER, H — Flat-earth guidance law using in-flight vehicle parameter identification, *Automatica*, 1976, **12**, 427–443.
7. VIJAYA VITTAL, R. AND SEETHARAMA BHAT, M. — Terminal guidance for a launch vehicle, *Int. Conf. Math. Theory of Control*, Dec. 1990, Indian Institute of Technology, Bombay.

Thesis Abstract (Ph.D.)

Some studies on laser-induced deposition and laser annealing of semiconductors by C. M. Harish.
Research supervisors: Vikram Kumar and A. Prabhakar (Organization).
Department: Physics.

1. Introduction

Laser-induced processes are becoming increasingly popular in microelectronic circuit fabrication. Economic

viability, process flexibility and the ability to initiate localised reactions are some of the factors that make these processes attractive. The present work is a study of two such particular applications of laser in microelectronic circuit manufacture: (i) Nd:YAG laser-induced deposition of copper films leading to demonstration of a direct-write process for fabricating microwave integrated circuits (MICs), and (ii) laser annealing of damages caused by ion implantation process in silicon. Evaluation of the temperature rise induced by laser during the above two processes is also included.

2. Laser-induced copper deposition

A technique for deposition of copper films on alumina through Nd: YAG laser-induced decomposition of copper acetate has been developed[1]. The decomposition of copper acetate, an organo-metallic compound, has been studied by Maslowska and Baranowska[2] in which copper is the only solid byproduct.

A 94–96 per cent pure alumina was used as substrate material. The substrates were cleaned using trichloroethylene in an ultrasonic bath to remove greasy material. Thereafter, a saturated solution of copper acetate in deionised (DI) water was sprayed on the substrate which was maintained at 90–95°C for 15 minutes. The solution dehydrated leaving behind a thin (approximately one micron) uniform coating of copper acetate on the substrate. It was thereafter exposed to a Q-switched Nd:YAG laser beam. Decomposition of copper acetate was found to commence when the incident average laser power was over 2 Watts, which corresponds to a laser power density of 25·46 kW/cm^2 for the experimental set up used in this study. The volatile byproducts of the reaction escaped leaving behind pure copper on the substrate. This has been confirmed through ESCA analysis of the deposited film. A computer-controlled galvomirror system was employed to generate the required pattern of the deposit film.

3. Laser direct write thin-film MIC fabrication

Using the above copper deposition technique, thin-film MICs have been fabricated. A graphical layout of the required circuit is prepared to scale. From the graphical layout of the circuit are extracted data pertaining to laser beam scan: laser beam position, number of scans and length of each scan. A computer program is then written, using this data, to control the laser beam positioner. A thin layer of copper acetate is coated on the substrate. Decomposition of copper acetate occurs when Nd:YAG laser beam of sufficient power is incident on the substrate Program for, say, the circuit pattern is run first. Next, the reverse side of the substrate is coated with copper acetate and the program for ground plane is executed. Thus direct write of both circuit side and ground plane on the substrate is achieved. The patterns are gold plated to obtain the required film thickness. A −3db, hybrid coupler is fabricated using this technique giving satisfactory performance.

4. Laser annealing of semiconductors

CW laser annealing of ion implantation damage has been widely reported[3,4]. Most of the work has used lasers operating in the visible region, as this radiation is readily absorbed in silicon. This along with very short dwell times used has sometimes failed to anneal out completely the implantation damage, especially in the interface region between the implanted layer and the bulk[5]. In this study, Nd·YAG laser is used at 1·065μ wavelength. This radiation is not well absorbed in silicon at room temperature. To increase the absorption and also to reduce the thermal stresses, the wafer temperature is maintained at 300°C.

Three commonly used dopant species namely, B_{11}, BF_2 and P_{31} are chosen for this study. CW Nd:YAG laser anneal of B_{11} and BF_2-implanted silicon yields samples with sheet resistance values matching those of the thermally annealed ones. The laser anneal power window is observed to be 14–17 Watts for the B_{11}-implanted samples and from 13–17 Watts for the BF_2-implanted samples. These power windows have been further confirmed by the I–V studies of the diodes formed by laser anneal. P_{31}-implanted samples could not be successfully annealed in this study.

Secondary ion mass spectroscopy (SIMS) analysis of the samples confirms that the dopant redistributions due to laser anneal are very meagre and ranges typically from 20 to 60 Å. Further, narrowing of the

implant profile accompanied by a shift in the profile peak towards the wafer surface is observed at lower anneal powers. Such anomalous behaviour does not appear to have been reported hitherto in literature. This anomalous redistribution has been explained on the basis of damage distribution in the host crystal due to ion implantation.

DLTS studies indicate that the defect state density in the samples goes through a minimum when annealed at laser powers of 15·5–16 Watts. An additional laser-induced defect state has been observed at 0°C in the case of BF_2-implanted samples.

5. Laser heating of materials

Finding the temperature in the case of laser heating requires solution of the heat diffusion equation for temperature with the appropriate heat production term added to account for energy deposition by laser beam.

The general heat diffusion equation can be written as[7]

$$\frac{K(T)}{D(T)}\frac{\partial T}{\partial t} - \nabla \cdot [K(T) \cdot \nabla T] = Q(x,y,z,t). \tag{1}$$

Here, T, the temperature (°K), is a function of position (x,y,z) and time t, $K(T)$, the temperature-dependent thermal conductivity, in W/cm °K, $D(T) = K(T)/\rho C$, the temperature-dependent thermal diffusivity, in cm^2/s (where ρ is the material density in g/cm^2 and C the heat capacity in J/g °K), $Q(x,y,z,t)$, the heat production in the solid per unit time per unit volume due to laser beam, in W/cm^3.

6. Laser heating of silicon

Assumptions made: (i) $K(T)$ and $D(T)$ are dependent on temperature but independent of position, (ii) $f(z)$ is a δ function and (iii) there is no flux density across the surface at $z = 0$, *i.e.*, there is no re-radiation of energy.

Kirchoffs transform[8] and Greens function[9] techniques are utilised to solve eqn (1). Linearised temperature θ is given by:

$$\theta(x,y,z) = \frac{P[1 - R(T)]}{\pi^{3/2}K(T_0)} \int_0^\infty f(u)du \tag{2}$$

where,

$$f(u) = \frac{\exp - \left[\dfrac{(X + V\sigma(T)u^2)^2}{u^2 + \dfrac{1}{\beta}} + \dfrac{y^2}{u^2 + \beta} + \dfrac{Z^2}{u^2} \right]}{\left[\left(u^2 + \dfrac{1}{\beta} \right) (u^2 + \beta) \right]^{1/2}}. \tag{3}$$

In relation (3),

$$X = \frac{x}{r},\ Y = \frac{y}{r},\ Z = \frac{z}{r},\ V = \frac{v}{r},$$

$$\sigma(T) = \frac{r^2}{4D(T)},\ \beta = \frac{r_y}{r_x},\ P_{ab} = \frac{P}{r}$$

$$P = \frac{P_i}{r},\ u = \left(\frac{2Dt'}{r_x} \right)^2 \text{ and } t' = -t'.$$

Evaluation of the integral [eqn (2)] has been carried out using Mathcad™ software package from Mathsoft Corporation, USA. The model successfully supports experimental observations made during laser annealing.

7. Pulsed laser heating of alumina

Assumptions made: (i) Thermal properties of the material to be constant, (ii) Energy lost from surface radiation is negligible, and (iii) Nd:YAG laser radiation is readily absorbed by alumina.

Following the technique presented by Ready[10], the solution for eqn (1) is written as:

$$\theta(\xi, \zeta, \tau) = \int_0^{\tau} \frac{P(\tau - \tau') \cdot \exp - \left[\frac{\xi^2}{\tau' + 1}\right] \cdot \exp - \left[\frac{\zeta^2}{\tau'}\right]}{\tau'^{1/2}\,(\tau' + 1)} \cdot d\tau' \qquad (4)$$

where,

$$\tau = \frac{4Dt}{r^2};\ \zeta = \frac{z}{r};\ \xi = \frac{s}{r} \text{ and } \theta = \frac{2K\sqrt{\pi T}}{rF_{max}}$$

$\theta(\zeta, \xi, \tau)$, the dimensionless temperature, is evaluated for any given pulse shape, *i.e.*, for a given $p(\tau - \tau')$.

Temperature evaluation for the particular case of Nd:YAG laser (1·065μ) heating of alumina (Al_2O_3) has been carried out using the above analysis. Integral at eqn (4) has been calculated using Mathcad™ software package. Estimated temperature rise using this model is in conformity with experimental observations.

References

1 HARISH, C. M., KUMAR, V. AND PRABHAKAR, A. — *J. Electrochem. Soc.*, 1988, **135**, 2903–2904.

2 MASLOWSKA, J. AND BARANOWSKA, A. — *J. Therm. Anal*, 1984, **29**, 309–315.

3 GAT, A AND GIBBONS, J. F. — *Appl. Phys. Lett*, 1978, **32**, 142–144.

4. KACHURIN, G. A., NIDAEV, E. V., KHODYACHIKH, A. V. AND KOVALEVA, L. A. — *Sov Phys. Semicond.*, 1976, **10**, 1128–1130.

5. NARAYAN, J. AND HOLLAND, O. W. — *J. Appl. Phys.*, 1984, **56**, 2913–2921.

6. BEADLE, W. E., TSAI, J. C. C. PLUMER, R. D. (eds) — *Quick reference manual for silicon integrated circuit technology*, 1985, Ch. 7, Wiley.

7. CARSLAW, H. S. AND JAEGER, T C. — *Conduction of heat in solids*, 1959, p. 10, eqn (8), Ch. 1 and 2, Oxford Uni. Press.

8. OZISIK, M. N — *Boundary value problems of heat conduction*, 1968, International Textbook Co.

9. NISSIM, Y. I., LIETOILA, A. GOLD, R. B. AND GIBBONS, J. F. — *J. Appl. Phys.*, 1980, **51**, 274–279.

10. READY, J. F. — *Effects of high power laser radiation*, 1971, Academic Press.

Thesis Abstract (Ph.D.)

Structure and properties of austempered ductile iron as affected by alloying, section size and heat treatment by D. Krishnaraj.
Research supervisor: S. Seshan.
Department: Mechanical Engineering.

1. Introduction

Cast irons are essentially alloys of iron, carbon, silicon, manganese, phosphorus and sulphur. Grey cast iron has free graphite in the form of interconnected flakes which account for its low tensile properties and poor toughness. Attempts to enhance the strength and toughness of grey cast iron led to the development of malleable iron. Subsequent efforts to produce high-strength cast irons having adequate ductility in the as-cast condition resulted in spheroidal graphite cast iron (also referred to as ductile iron or nodular iron or simply as S.G. iron). Since then the use of ductile iron has grown very rapidly to meet the increasing demands of the machine tool industry, automobiles and various other engineering sectors.

In grey iron, the properties are primarily controlled by the size, shape and distribution of graphite, rather than by the matrix. On the other hand, in ductile irons, matrix variations have profound effect on mechanical properties. Of the different high-strength matrices, bainitic matrix is the one to attract attention in recent times. The production and use of as-cast bainitic ductile iron has been known for few years. However, as-cast bainitic ductile irons cannot reach the high toughness values demanded in several applications. On the other hand, austempered ductile iron (ADI) has been reported to possess much higher toughness and strength values than the as-cast bainitic ductile iron. The properties of ADI are known to be dependent on base chemistry, parameters of heat treatment, presence of alloying elements and section size of the casting. It is seen from the review of available literature that the present knowledge on the combined effect of the above variables on the kinetics of bainitic transformation and on the mechanical properties of ADI is rather limited.

In other words, even though the potential of ADI is well established, the material continues to perplex the researchers and foundrymen. In order to obtain data on the effect of the above referred variables on the structure and properties of ADI and to establish reliable combination of parameters, a systematic investigation was taken up. The salient findings of the above investigation are reported here.

2. Experimental details

Unalloyed and alloyed ductile iron test castings (keel blocks representing thin and thick sections, respectively) were made adopting the standardized procedure of melting, spheroidising treatment, inoculation and casting. In all, 20 different combinations of alloy additions (Ni, Mo and Cu in different amounts) were tried. Test blanks cut from these castings were subjected to austempering treatment under various combinations of austempering temperature and austempering time. Test samples were machined from these heat-treated blanks in order to analyse the influence of alloying, section size and heat-treatment on the following:

a. Microstructure and morphology of bainite (using optical microscope)
b. Tensile properties (using Hounsfield tensometer)
c. Impact strength (using instrumented impact testing facility)
d. Hardness (using Brinell hardness testing machine)
e. Retained austenite (using image analyser and scanning electron microscope)
f. Wear resistance (using instrumented wear testing set-up).

3. Conclusions

The findings of the investigation were systematically analysed to study the influence of process variables,

viz., (a) austempering temperature and time, (b) alloy content, and (c) section thickness on the structure and properties.

a. Microstructure

Austempering temperature has considerable influence on the microstructure. Corresponding to low temperatures of austempering, lower bainitic structure results: with increased temperature, the structure changes to a mixture of lower bainite and upper bainite. At still higher temperatures of austempering, fully upper bainitic structures are obtained. On the other hand, austempering times have only a marginal effect on structure, that too only at higher austempring temperatures. Addition of alloying elements results in morphological changes in the bainitic matrix. This effect is felt more at higher austempering temperatures The duration of austempering needed to realise fully bainitic structure increases with increasing alloy contents. In general, alloying elements promote structural heterogeneity in terms of fairly large quantities of martensite for short austempering times and untransformed austenite/martensite for longer austempering durations. In thick sections, alloying additions do help in improving the hardenability (however, thin sections do not mandate any improvement in hardenability).

b. Mechanical properties

Consistently high UTS values were possible in all the trials. UTS increases with austempering time, reaches a maximum (corresponding to the completion of bainitic transformation) and subsequently decreases. Whereas, with increasing austempering temperatures UTS decreases. Thick sections of unalloyed ADI have lower UTS compared to thin sections. Alloying additions, in general, bring about a reduction in tensile strength in thin sections. This is attributed to their effect in slowing down the reaction and introducing heterogeneity in the microstructures. The UTS of thick sections increases with alloying additions to reach a peak and decreases thereafter. Therefore, appropriate selection of alloy contents is to be done based on the section thickness of the castings. Molybdenum additions have the effect of countering the adverse effect of nickel on UTS. Elongation increases with austempering temperature initially and decreases thereafter. Elongation increases initially with alloy contents but decreases beyond a certain level indicating the harmful effect of over alloying.

Variation of impact strength is similar to that of elongation. Impact properties show an initial increase with alloying, followed by a subsequent drop. In this context, the control of molybdenum at the appropriate level checks the reduction due to over alloying with nickel. High hardness values are obtained corresponding to short austempering durations but hardness decreases with increase in austempering time. The hardness, in general, increases with increasing alloy contents, and this increase is more pronounced for short austempering times where the chances of incomplete transformation are more.

c. Austenite volume

The volume of retained austenite in bainitic phase (assessed using the image analyser) increases with increasing austempering temperature. The variation in austenite volume with austempering temperature at the intermediate range of temperatures is not considerable, but at higher austempering temperatures (the upper limit of bainitic transformation temperatures) the austenite volume gets reduced.

Alloying additions increase the austenite volume of upper bainite but a reduction is observed at high levels of alloying due to incomplete reaction. On the other hand, the austenite volume of lower bainite shows very little variation with alloying

d. Wear resistance

Wear resistance of ADI test castings corresponding to short durations of austempering has been found to be somewhat poor, but the wear resistance improved appreciably on increasing the duration of austempering. The presence of alloying elements does not have any marked influence in improving the wear resistance of ADI.

It has been concluded that an appropriate combination of austempering variables and alloy contents is essential (with the consideration to the section size of the casting) in order to realise the desired structure and properties in ADI castings Over alloying and the use of very high temperatures and durations of heat treatment have proved harmful.

References

1. MOORE, D. J , *et al*	On the structure and mechanical properties of austempered ductile iron, *Trans Am Foundrym. Soc* , 1985, **93**, 705–719
2. COX, G. J.	The effect of austempering time on the properties of high strength S G irons, *Br. Foundrym.*, 1986, **79**, 215–220.
3 HEHEMANN, R. F., *et al*	A debate on the bainitic reaction, *Metall Trans.*, 1972, **3**, 1077–1085.
4. GAGNE, M. AND FALLON, P. A	Microstructural characteristics of bainitic ductile iron, *Can. Metall Q.*, 1986, **25**, 79–90.
5. RUNDMAN, K. B. AND KLUNG, R. C	An x-ray and metallographic study of austempered ductile cast iron, *Trans Am. Foundrym. Soc* , 1982, **90**, 499–505
6. LEI, T. S. *et al*	Rolling sliding contact fatigue of austempered ductile iron with and without Ni-Mo, *Trans Inter. Conf on ADI*, 1984, pp. 45–51.

Thesis Abstract (Ph.D.)

Non-equilibrium solidification of pure metals (Al, Cu, Ni), bismuth, eutectic Al–Ge and Al–Cu and peritectic Al–Cr alloys by V. Thiruvenkataswamy.
Research supervisors: S. Ranganathan and K. Chattopadhyay.
Department: Metallurgy.

1. Introduction

Since the seminal discovery of the production of metastable microstructures *via* rapid solidification by Duwez *et al*[1], there has been extraordinary interest in understanding, predicting and controlling these microstructures. Metastability can be of three kinds; compositional, structural and morphological. While a broad knowledge of the thermodynamic and kinetic factors that control the evolution of microstructure during non-equilibrium solidification exists, a full understanding is still far away. The present study explores the non-equilibrium solidification behaviour of metals and alloys with particular emphasis on the micro-second-pulsed laser processing.

2. Experimental techniques

The starting materials used were of 4N purity. A number of selected Al–base (Al–Cu, Al–Ge and Al–Cr) alloys were prepared under controlled atmosphere. An Nd–glass–pulsed laser was used in conjunction with other non-equilibrium processing techniques such as twin-roller quenching for achieving rapid solidification and entrained droplet for achieving undercooling. Material characterisation was done by using optical, SEM and TEM microscopy, XRD and differential scanning calorimetry.

3. Interaction of laser with Al, Cu, Ni and Bi

The characteristics of laser interaction with different pure metals, namely, aluminium, copper, nickel and a semimetal bismuth were studied in detail. The plots of radius of the laser-affected regions above the melting threshold as a function of total energy show three distinct stages. The first stage which appears at lower energy level is nonlinear in nature. This is followed by a linear region. At still higher energy, a

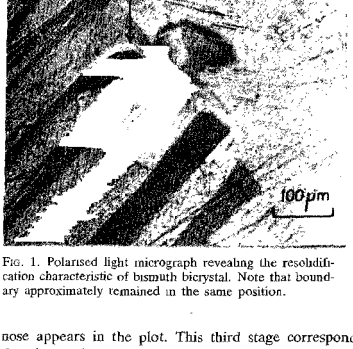

FIG. 1. Polarised light micrograph revealing the resolidification characteristic of bismuth bicrystal. Note that boundary approximately remained in the same position.

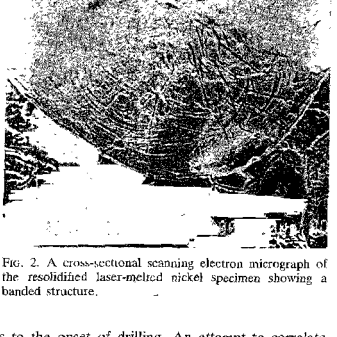

FIG. 2. A cross-sectional scanning electron micrograph of the resolidified laser-melted nickel specimen showing a banded structure.

nose appears in the plot. This third stage corresponds to the onset of drilling. An attempt to correlate the observation with a measure of beam diameter obtained by measuring the radius of the carbon hole succeeded only in the case of second stage where the melted region scales with the beam diameter.

The first stage is prominent only in high-conductivity metals like aluminium and copper, while the second stage is dominant for nickel and bismuth. These are analysed in terms of thermal diffusion distances.

4. Evolution of microstructure in laser-melted pool of Bi and Ni

Following the establishment of easy-glazing regions in bismuth and nickel, we have carried out a detailed study to understand the microstructural evolution during resolidification of the laser-melted pool. The regrowth characteristics[2] of the laser-melted pool along a grain boundary for a bismuth bicrystal are such that boundary does not displace significantly (Fig. 1). For polycrystalline bismuth with a mixed grain size, the epitaxial regrowth is dominated by larger grains. The solidified structure tends to be coarse. A combination of fine-grain size and lower energy pulse inhibits epitaxial regrowth and promotes fresh nucleation. Thus, a large fraction of random grain boundaries inhibits epitaxial growth. For coarse-grained structure, epitaxial regrowth leads to the elimination of fine twins. On the other hand, the presence of smaller grains leads to fine twins in the epitaxially regrown grains

Polycrystalline nickel grows epitaxially into the melt during resolidification of the laser-melted pool. Impurities reveal a cellular growth interface. A characteristic semicircular banded feature with random band spacing aligned perpendicular to the growth direction during the resolidification of high-energy laser pulse-melted nickel pool can be observed (Fig. 2). The origin of such bands is probably related to the stress-assisted impurity precipitation. For lower energy pulse-melted pool, grain refinement takes place indicating the nucleation of fresh nickel grains. This effect is similar to that for bismuth but less dramatic in nature.

5. Microstructural evolution and phase selection during resolidification of laser-melted eutectic alloys

Following the study of pure elements, we have concentrated our attention on binary eutectic alloys. The microstructural evolution and phase selection during the resolidification of laser-melted pool was characterised and compared with the results of other non-equilibrium processing to bring out the similarities and differences of laser processing. Two eutectic systems, namely, Al–Cu and Al–Ge were chosen. While metastable phases form under non-equilibrium conditions in the latter, only microstructural modifications are known to occur in the former.

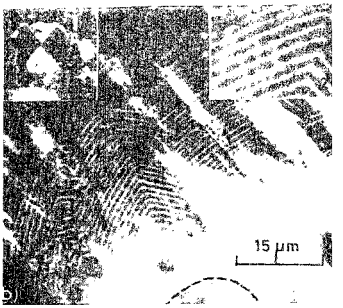

FIG. 3. The solidification microstructure of laser-melted pool of Al–Cu eutectic alloy. Higher magnification micrograph of the centre revealing a banded growth morphology radially away from a nucleating particle (shown by dotted line). Inset 1 shows polarised light micrograph of the particle confirming the phase to be Al_2Cu. Inset 2 shows enlargement of the portion of the band revealing discrete particles.

FIG. 4. The solidification microstructure of laser-melted pool of Al–Ge eutectic alloy. The polarised light micrograph of the columnar grain (see inset) microstructure in the successive melt puddles.

In the case of Al–Cu near-eutectic alloy we have first studied[3] the evolution of microstructure of undercooled alloys by entrained droplet techniques. The different microstructures thus obtained could be rationalised in terms of the extrapolated metastable phase diagrams. The knowledge gained is then extended to analyse the resolidification characteristics of the laser-melted pool. A significant result of the laser processing is the observation of a banded eutectic structure. The occurrence of such bands could be explained by a simple model[4] involving nucleation of Al_2Cu in the solute-rich boundary layer ahead of the moving front due to the establishment of local equilibrium at the interface at the growth temperature.

The results[5] of Al–Ge eutectic alloy indicate the nucleation and columnar growth of a metastable monoclinic phase[6] from the melt/substrate interface at high-power density situation. The requirement of composition partition acts as a barrier for eutectic regrowth during the solidification of the laser-melted pool. The growth advantage of the monoclinic phase stems from the fact that very little solute partitioning is needed for its growth in the near-eutectic melt. Evidences point to a possible competition of monoclinic phase with germanium and possibly α-Al at very low-energy pulsing situation. This situation yields a fine-grained microstructure.

6. Evolution of microstructure and phases in Al–Cr system during non-equilibrium solidification

Following the eutectic systems, we concentrate our attention on Al–Cr alloys (up to 20 at % Cr) which contain a cascade of peritectic reactions. Both laser processing and twin-roller technique of rapid solidification were used to achieve non-equilibrium solidification. However, for ease of microscopy, materials obtained by the latter technique were used more extensively.

Icosahedral quasicrystalline phases[7] having non-crystallographic symmetry are observed from 7 to 15 at% Cr alloys, while equilibrium crystalline "–$Al_{11}Cr_2$ phase is completely absent. Both rapid solidification and subsequent thermal decomposition studies indicate that the main competing phase is θ–Al_7Cr up to 15 at% Cr. Beyond this composition, ϵ–Al_4Cr is the dominant phase together with a small amount of Γ_4–Al_7Cr_3. We have shown[8] that the electron-diffraction patterns of Al–Cr quasicrystals are often associated with a diffuse intensity[9] distribution indicative of short-range order. The change in quasilattice constant with composition suggests the existence of structural vacancies. Further, a sudden change from coarse to

ultrafine quasicrystalline grain structure in Al–7 at% Cr alloy points to a change in nucleation mechanism from heterogeneous to homogeneous mode during the rapid solidification

References

1 DUWEZ, P., WILLIAMS, R. H. AND KLEMENT, W. — *J Appl. Phys*, 1960, **31**, 1136–1137

2 SWAMY, V. T., RANGANATHAN, S. AND CHATTOPADHYAY, K. — *J Cryst Growth*, 1989, **96**, 628–636

3 CHATTOPADHYAY, K., SWAMY, V. T. AND AGARWALA, S. L. — *Acta Metall Mater*, 1990, **38**, 521–531

4 CHATTOPADHYAY, K. AND MUKHOPADHYAY, N. K. — *J Cryst Growth*, 1990, **106**, 387–392.

5 SWAMY, V. T., CHATTOPADHYAY, K. AND RANGANATHAN, S. — *Mater Sci Engng A*, 1990, **123**, 247–254.

6 KOSTER, U. — *Acta Metall*, 1972, **20**, 1361–1370

7 SHECHTMAN, D., BLECH, I., GRATIAS, D. AND CAHN, J. W. — *Phys Rev Lett*, 1984, **53**, 1951–1953

8 SWAMY, V. T., RANGANATHAN, S. AND CHATTOPADHYAY, K. — *J. Mater Res.*, 1989, **4**, 539–551

9 MUKHOPADHYAY, N. K., RANGANATHAN, S. AND CHATTOPADHYAY, K. — *Phil Mag Lett*, 1987, **56**, 121–127

Thesis Abstract (Ph.D.)

Effect of zirconium and titanium additions on the decomposition behaviour of Al–1% Si alloy by George Helmy Deaf.
Research supervisors: E. S. Dwarakadasa and E. S. Rajagopal.
Department: Physics.

1. Introduction

Metal aluminium finds a number of applications in alloyed form because of its low melting point, low density, high specific heat and high specific strength. The fact that it is resistant to corrosion, due to the impervious oxide layer that forms on the surface, and can be greatly strengthened by precipitation hardening has made it a very important engineering material. Addition of metals like Si, Li, or Mg either singly or together decreases the melting point further and improves the foundry characteristics. To improve strength in these alloys normally a small addition of Zr or Ti is made, which refines the grain size by inhibiting recovery and recrystallization rate through the formation of very fine intermetallic particles that pin the grain boundaries. Although the level of additions made is only sufficient to refer to them as trace additions, transition elements exert strong influence on the development of the final microstructure in these alloys. Addition of Zr has only recently been developed while Ti additions have been well studied. Fe, present as an inevitable impurity in Al, also exerts some influence. These additions are becoming important. The exact influence of these elements, Fe, Zr and Ti, when present together is not well studied. In view of the commercial importance of this, especially in Al–Si alloys, the present project was undertaken to investigate the influence of small additions of Zr and Ti in the presence of Fe as an impurity in Al–1% Si alloys. The aim of the study was to evaluate the influence of these additions on the decomposition behaviour of the Al–Si alloy in the evolution of the final microstructure. Alloys could be solutionised at high temperature and quenched to generate a supersaturated state which on annealing would lead to an interaction between point defects present in the material that will eventually give rise to the observed microstructure.

Table I
Chemical composition of the experimental alloys

Material	*Si*	*Fe*	*Ti*	*Zr*	*Mg*	*Al*
Alloy-A	1·10	0·06	0·01	–	0·11	Balance
Alloy-B	1·19	0·20	0·01	–	0·11	Balance
Alloy-C	0·98	0·06	0·01	0·04	0·11	Balance
Alloy-D	1·09	0·20	0·01	0·05	0·11	Balance
Alloy-E	0·93	0·06	0·11	0·05	0·11	Balance

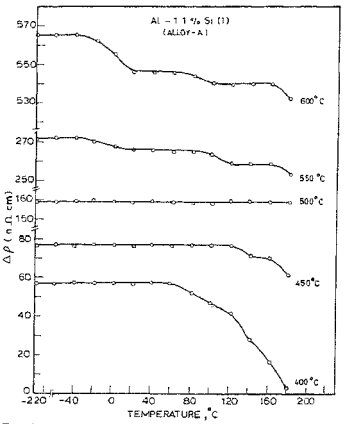

FIG 1(a)

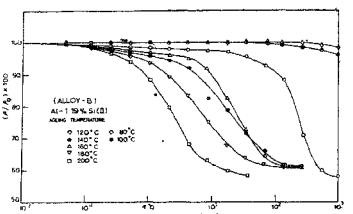

FIG. 1(b).

FIG. 1 Ageing resistivity data for (a) Isochronal, Al–1·1% Si, and (b) Isothermal, Al–1·19% Si.

FIG. 2(a)

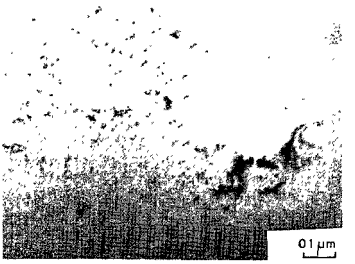

FIG. 2(b)

FIG. 2. Transmission electron micrograph of (a) precipitated Si on dislocations, and (b) refined Si precipitate.

2. Experimental procedure

The alloys used in this investigation were prepared by melting either high purity or commercial-purity Al (containing 0·06% Fe) and adding desired quantities of the alloying elements Si, Zr and Ti through certified master alloys. The composition of the experimental alloys is given in Table I.

The homogenized alloy melt was chill cast into 15 mm rods, homogenized for 48h at 500°C rolled in several stages to 3 mm dia wire rods and finally drawn in diamond dies to 0·7 mm wires or rolled into foils of 0·1 mm thickness.

Wire specimens of length 1m wound non-inductively into a helical coil were solutionized at various temperatures, rapidly quenched and then annealed isochronally or isothermally, while following the decomposition process by resistivity measurements (made at liquid nitrogen temperature) or x-ray diffraction or by thin-foil transmission electron microscopy.

3. Results and discussion

Figure 1 shows a typical set of isochronal and isothermal annealing data which brings about clearly a vacancy mechanism of Si precipitation. The isothermal resistivity data fit into a conventional sigmoidal growth curve, enabling determination of activation energy for vacancy formation, vacancy migration and Si precipitation. The decomposition process itself seems to be divided into a slow first stage of vacancy annihilation, a rapid second stage involving clustering and precipitation of Si and a third slow stage of growth of these precipitates. Although all the curves reach a stable plateau indicating that all of the alloys reach a stable state, the effect of the presence of Fe, Ti and Zr is to retard the kinetics of precipitation by sequestering the vacancies, because of their larger binding energy. In terms of relative effect, Zr exerts the most marked influence. Measurement of residual resistivity after quenching from higher temperatures indicates increasing amounts of Ti, Zr and Fe retained in solid solution and hence capable of larger influences.

Transmission electron microscopic observations clearly indicate the presence of a bimodal distribution of Si, the origin of which is: separation of large Si particles during solidification and precipitation during later decomposition. The latter seem to form on dislocations, shown typically in Fig. 2(a). A small number of dislocation loops were observed in all the alloys. The size of the precipitated Si gets refined in the presence of the alloy additions (Fig. 2(b)), while there is no influence on the larger sized particles. X-ray diffraction studies confirm the effects of the formation of different types of intermetallics in the alloy.

4. Conclusions

The addition of Zr, Ti and Fe retards the decomposition of the Al–Si alloy and increases stability. Of the three alloying elements the effect of Zr is most marked, suggesting that the use of Zr as a grain-refining element is preferable to using other transition elements.

References

1. JONES, H. — *Rapid solidification process* (R Mehrabian, B H. Kear and M. Cohn, eds), 1980, p. 306, Claitors, Baton Rouge, USA.
2. RYUM, N. — *Acta Metall.*, 1969, **17**, 269–278; 821–830
3. WESTERLUND, R W. — *Metall. Trans.*, 1974, **5**, 667–672.
4. MORRIS, J. G. AND BENNETT, J. E. — *Scr. Metall.*, 1969, **3**, 15–21.
5. OZAWA, E. AND KIMURA, H. — *Mater. Sci Engng*, 1971, **8**, 327–335.

Thesis Abstract (Ph.D.)

Microstructural studies of some rapidly solidified titanium eutectoid alloys by T. A. Baskaran.
Research supervisors: S. Ranganathan and R. V. Krishnan.
Department: Metallurgy.

1. Introduction

In the scenario of development of high-temperature titanium alloys, rapid solidification has assumed great significance due to various attributes associated with this process. Of the various classes of rapidly solidified titanium alloys, titanium aluminides, titanium alloys containing rare-earth and metalloid dispersions and titanium-eutectoid alloys hold promise for such high-strength applications[1,2]. In the present study, an attempt has been made to study the microstructural evolution in rapidly solidified titanium eutectoid alloys.

2. Material preparation and experimental procedures

Rapid solidification of a number of titanium-eutectoid alloys has been carried out by electron beam melting and splat quenching. The alloys studied included the binary alloys of Ti–28% Mn, Ti–2·8% Co, Ti–5·4% Ni, Ti–30·4% Ni, Ti–4·5% Cu and Ti–5·5% Cu. Melt-spun ribbons of Ti–37% Mn and Ti–24% Mn–13% Fe were provided by Prof. K. F. Kelton. Ternary additions of silicon were made to Ti–28·6% Ni alloy to study the glass-forming ability.

The rapidly solidified ribbons were characterised by optical microscopy, scanning electron microscopy, transmission electron microscopy, x-ray diffractometry and EDX analysis.

3. Results and discussion

A wide spectrum of microstructures has been obtained which includes quasicrystalline, crystalline and amorphous phases. The high cooling rates have led to a refinement of the microstructures and helped to overcome grain boundary segregation of solutes encountered during ingot processing of these alloys.

3.1. *Quasicrystals and other metastable phases in titanium–manganese alloys*

Figure 1(a) shows the bright field transmission electron micrograph of the icosahedral quasicrystals in melt-spun Ti–37% Mn alloy. The quasicrystals exhibit a speckle contrast and are divided into a number of segments. The 5-3-2-fold selected area diffraction patterns obtained from this phase are shown in Fig. 1(b)–(d) confirming the $m\bar{3}\bar{5}$ symmetry. In addition to the sharp diffraction spots, the presence of diffuse intensity is observed in the 2-fold pattern.

It is noticed that the formation of the quasicrystalline phase in these alloys does not follow any of the known criteria for the I-phase formation, *viz.*, the phase diagram criterion observed in Al–Mn quasicrystal[3] or the crystal structure criterion in the Mg-base quasicrystals[4]. The diffuse intensity observed in the present study is similar to that reported by Gibbons *et al*[5] in Ti–Mn quasicrystals and those observed on annealing the Al–Mn quasicrystals[6]. The presence of diffuse intensity and arcs of diffuse intensities are interesting, since it is expected to give vital information regarding the atomic decoration underlying the quasicrystalline lattice. The arcs of diffuse intensity are found to lie on the odd parity directions and follow a τ inflation rather than τ^3 inflation as reported for the Al–Mn quasicrystals[6]. It is found that the higher order arcs deviate from this rule. The diffuse intensities are explained on the basis of superlattice ordering[6]. It is observed that peak distortion of the inner spots occurs in the 5-fold electron diffraction pattern. It could be due to the presence of phason distortion[7] in the quenched state of the quasicrystals.

The formation of quasicrystals in this alloy is shown to be related to the b.c.c phase with a = 21·7 Å which can be a 2/1 rational approximant structure.

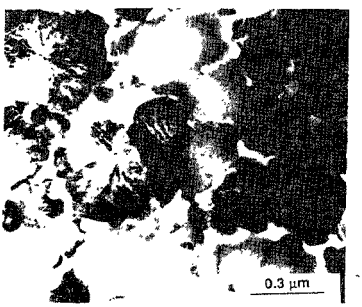

(a)

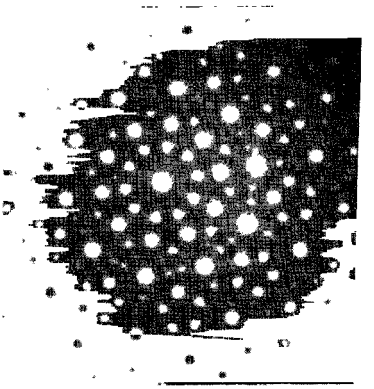

(b)

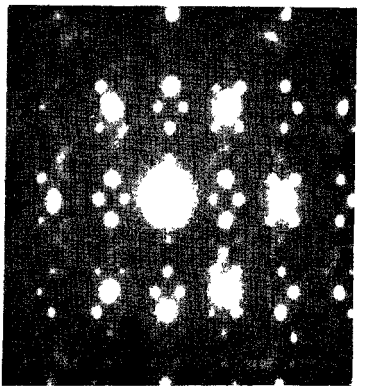

(c) (d)

FIG. 1. (a) Transmission electron micrograph showing the icosahedral quasicrystals in rapidly solidified Ti–37% Mn alloy; (b)–(d) 5–3–2-fold selected area diffraction patterns from the I-Phase in Ti–37% Mn alloy.

An icosahedral quasicrystal has been observed in Ti–24% Mn–13 Fe alloy in the rapidly quenched condition. In the rapidly quenched Ti–28 at % Mn alloy an interesting occurrence of short-range order is noticed (Fig. 2) The short-range order is similar to the SRO in Ni_4Mo. The position of the diffuse

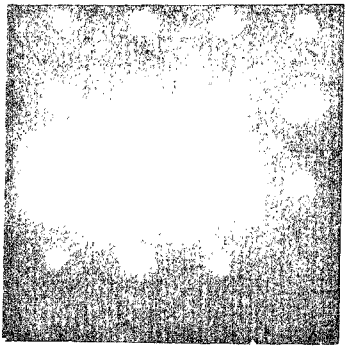

FIG. 2 Selected area diffraction pattern showing the presence of SRO in rapidly solidified Ti–28% Mn alloy

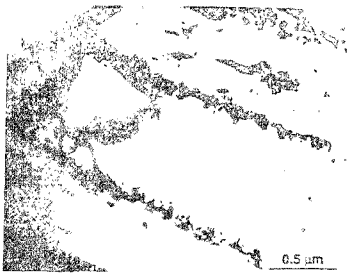

FIG. 3(a) Transmission electron micrograph showing non-lamellar eutectoid product in Ti–2·8% Co alloy in the as quenched condition

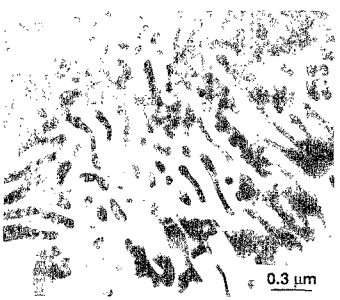

FIG. 3(b)

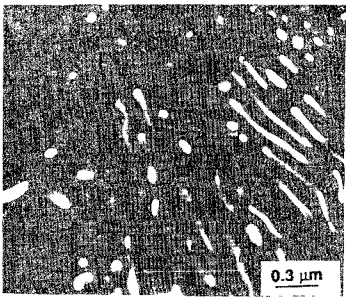

FIG. 3(c).

FIG. 3 (b)–(c) Bright field and dark field transmission electron micrographs showing the lamellar (pearlite) eutectoid decomposition product in Ti–5·4% Ni.

intensity is found to lie at the (1, 1/2, 0) positions However, the matrix in the present case is a b.c.t. phase. This seems to be the first observation of this kind.

3.2. *Eutectoid decomposition*

Eutectoid decomposition in the rapidly solidified titanium eutectoid alloys (Ti–2·8% Co, Ti–5·4% Ni, Ti–4·5% Cu and 5·5% Cu) has been followed. The alloys studied included hypoeutectoid and near-eutectoid compositions. While the alloys of hypoeutectoid composition, *viz.*, Ti–2·8% Co and Ti–4·5% Cu alloys showed a bainitic mode, the near-eutectoid alloys showed pearlitic mode predominantly. Figure 3(a)

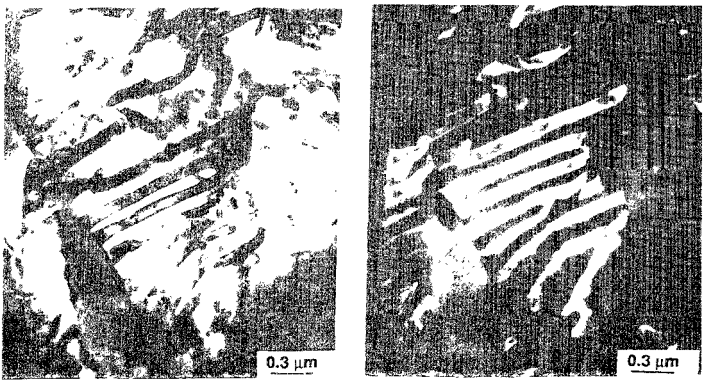

(a) (b)

FIG 4 Transmission electron micrograph showing the nucleation of pearlite colony at proeutectoid alpha interface

shows the nonlamellar mode of eutectoid decomposition in rapidly solidified Ti–2·8% Co while Figs 3(b) and (c) are the bright field and dark field images of the lamellar mode (pearlite) of decomposition occurring in the rapidly solidified Ti–5·4% Ni

Two competing transformations are occurring during rapid quenching of the titanium eutectoid alloys, namely, martensite and eutectoid decomposition of the β phase. On considerations of nonequilibrium conditions, it is proposed that rapid quenching shifts the eutectoid temperature and expands the composition range over which it can occur. Further, increased surface area due to the refinement of the grain size facilitates eutectoid decomposition Similarly, the M_s temperature is also seen to be influenced by the cooling rates

The hypoeutectoid alloys seem to decompose by a nonlamellar mode. The results are discussed taking into account the significant role of interfacial structures. The proeutectoid α nucleation seems to occur by a sympathetic nucleation. The analysis of the interfacial structures by electron microscopy revealed that the proeutectoid α interfaces are partially coherent.

The outcome of the present investigation in Ti–5·4% Ni and Ti–5·5% Cu alloys showed that the pearlite lamellae often nucleated on the broad faces of the proeutectoid α which is partially coherent. Figure 4 is the transmission electron micrograph illustrating this point Further, the tips of the growing Ti_2Cu lamellae are found to be characterised by misfit dislocation structures. These experimental facts are contradictory to the hitherto understood views of pearlite evolution which is based on the cooperative growth of the lamellae at the disordered boundaries which provide the necessary conditions for such growth. Our experimental observations are supporting the results of Lee and Aaronson[8] who first showed that pearlite can indeed evolve at the semicoherent interface. It has also been observed that the lamellar growth of the Ti_2Cu phase occurs by sympathetic mechanism. This is the first observation of this nature. The glass-forming ability of Ti–Ni alloy of near-eutectic composition has been studied in Ti–28·5% Ni–10% Si and it has been shown that rapid solidification of this alloy resulted in the formation of amorphous-phase partially. Crystallisation studies of the amorphous phase indicated that the amorphous phase decomposes initially by the formation of a b.c.c. phase before the intermetallic compound is formed.

4. Conclusions

Rapid solidificaion of titanium–eutectoid alloys has given rise to a variety of microstructures. Quasicrystalline, crystalline and amorphous phases have been synthesised.

References

1 WHANG, S H. *J. Mater Sci.*, 1986, **21**, 2224–2238.

2 BOMBERGER, H B. AND FROES, F. H *Titanium rapid solidification technology* (Froes, F H. and Eylon, D., eds) 1986, pp 21–44, Metal Society, AIME

3. SHECHTMAN, D , BLECH, I GRATIAS. D. AND CAHN, J W *Phys. Rev Lett*, 1984, **53**, 1951–1953

4 RAMACHANDRA RAO, P AND SASTRY, G. V. S. *Pramana*, 1985, **25**, L225–L230.

5. GIBBONS, P. C., KELTON, K. F., LEVINE, L E AND PHILIPS, R. B *Phil Mag B*, 1989, **59**, 593–618.

6 MUKHOPADHYAY, N K , RANGANATHAN, S AND CHATTOPADHYAY, K. *Phil. Mag Lett.*, 1987, **56**, 121–127.

7. LUBENSKY, T C , SOCOLAR, J E. S. STEINHARDT, P J., BANCEL, P. A AND HEINEY, P A. *Phys Rev Lett.*, 1986, **57**, 1440–1443

8. LEE, H. J AND AARONSON, H. I *J Mater Sci*, 1988, **23**, 150–160

Thesis Abstract (M.Sc. (Engng))

A graphical simulation environment for robotics applications by K. A. Jasmeer.
Research supervisors: Y. N. Srikant and M. R. Chidambara.
Department: Computer Science and Automation.

1. Introduction

Graphic simultors, to program robots offline, are receiving greater attention of late. Graphic simulators, in general, are more flexible in adapting to widely varying situations when compared to any other simulator, but the simulators developed so far are tied to particular robot environments[1–5]. The reasons behind this can be traced to two facts. First, not only robots but the applications they are subjected to also differ widely in nature and specifications. Secondly, the primary design aim is always to lessen the burden on the user. As a result, the tendency is to incorporate more and more details of the applications into the simulator, thereby reducing its flexibility drastically.

We have developed a general-purpose graphic environment to simulate robotic applications in the Robotics Laboratory at the Indian Institute of Science.

2. Design objectives and approach

The main design objective is that it should be possible to model different applications easily. So the techniques used for modelling and analysis should be general in nature. Specifically,

i) the modelling technique used should be general enough to model robots of any type with any number of degrees of freedom,

ii) the technique used for animation should be general enough to emulate any robot programming languages, and

iii) there should be general facilities to carry out analyses, both of physical (*e.g.,* work volume calculation) and geometric reasoning type (*e.g.,* collision avoidance path planning).

Our approach to this problem is unique. We organise the environment into two main modules, a graphic modelling system and a programming language interface to it. We keep the graphic modelling system as simple as possible; no solid modelling techniques are used. The second module compensates for this simplicity in modelling in a more flexible manner. It allows the user to develop world models and to carry out analyses according to the application. Apart from this, the language achieves animation more efficiently in a programmed manner. Thus, simulation of an application becomes executing an application program in this environment.

3. ANISOFT

We have named the environment developed by us as ANISOFT. As mentioned earlier the two main modules of ANISOFT are the graphic modelling system and the programming language interface to it. In addition to these two, it has three more modules, namely, the subsystems for viewing, teaching and cell editing. All these modules have been integrated into a menu-driven command hierarchy.

The modelling system creates and displays a cell which consists of the robots and their environment. A language has been designed for model specification. It can model not only robots but also other open kinematic structures such as gripper with fingers, etc.

The viewing system helps the user to see the images from different views. ANISOFT has been provided with facilities to have simultaneous multiple views on the screen. All changes in viewing are achieved using a mouse, thus making it very user-friendly.

Cell editing is a menu-driven process to change the position and orientation of the modelled entities. This module is very useful while modelling. During each trial, using the cell editor, different configurations of the entity can be tested.

In industrial robotics a teach-pendant is often used to teach the robot. ANISOFT duplicates this technique to teach the modelled robots. Teaching is a menu-driven process. The stored joint vectors can be read from the programs in ANISOFT's language.

Programming language interface is the most important part of ANISOFT. A language designed for such a purpose should meet the requirements such as easy and efficient animation, efficient constructs for robotics-specific computation and easy development of world models. In the completed implementation we could do full justice only to the first requirement. The language designed, which we call ANIL for ANImation Language, has constructs to achieve animation efficiently. Currently, it has simple data types and structures, simple constructs for numerical computation. At present no constructs have been provided for world model development. Future work can take care of this in addition to providing more sophisticated constructs.

References

1. GINI, G. C. AND GINI, M. L. — Dealing with world-model-based programs, *ACM Trans. Progm. Lang Syst.*, 1985, **7**, 334–347

2. LUMIA, R. — CAD-based off-line programming applied to a cleaning and deburring workstation, *CAD-based programming for sensory robots* (Bahram Ravani, ed), NATO ASI Series, Series F. Vol. 50, 1988, Springer-Verlag.

3 MIROLO, C. AND PAGELLO, E. — A solid modeling system for robot action planning, *IEEE Comput. Graphics Applic.*, 1989, **9**, 55–59.

4. THEVENEAU, R. AND PASQUIER, M. A geometric modeler for an automatic robot programming system, *CAD-based programming for sensory robots* (Bahram Ravani, ed), NATO ASI Series F, Vol 50, 1988, Springer-Verlag

5 TILOVE, R. B Extending solid modeling systems for mechanism design and kinematic simulation, *IEEE Comput Graphics Applic* , 1983, **3**, 9–19

IISc Theses Abstracts

Author Index

Nov.–Dec. 1992